

Copyright
by
Christopher Joseph Lombardo
2011

**The Dissertation Committee for Christopher Joseph Lombardo Certifies that this is
the approved version of the following dissertation:**

**Development of New Experimental Techniques for Studying Transport
and Recombination in Organic and Inorganic Thin Film Solar Cells**

Committee:

Ananth Dodabalapur, Supervisor

Sanjay Banerjee

Seth Bank

Brian Korgel

Emanuel Tutuc

Edward Yu

**Development of New Experimental Techniques for Studying Transport
and Recombination in Organic and Inorganic Thin Film Solar Cells**

by

Christopher Joseph Lombardo, B.S.; M.S.

Dissertation

Presented to the Faculty of the Graduate School of
The University of Texas at Austin
in Partial Fulfillment
of the Requirements
for the Degree of

Doctor of Philosophy

The University of Texas at Austin

May 2011

Dedication

To all of the people of our global community who need low-cost solar energy to gain access to a sufficient amount of clean water, to become agriculturally self-sufficient and eradicate hunger where it is endemic, and to provide light so that children can become literate, enrich their lives through education, and break the cycle of poverty.

Acknowledgements

I would to thank my advisor Professor Ananth Dodabalapur for his guidance and support over the past six years. In addition, I'd like to thank all of the present and former members of the Organic Electronics Research Group especially Davianne Duarte, Dr. Brian Cobb, Chen-Guan Lee, Eric Danielson, Tae-Jun Ha, Dr. Suvid Nadkarni, Dr. Yeon-Taek Jeong, Tanvi Joshi, Kiran Divakar, Sebastian Scheofer, Dr. Larry Dunn, Dharmendar Reddy, Dr. Debarshi Basu, Deepak Sharma, Dr. Byungwook Yoo, Dr. Taeho Jung, Dr. Dan Fine, and Dr. Llang "Frank" Wang for useful discussions, brainstorming, and help in the lab. Thanks goes out to the Microelectronics Research Center staff for all of their support, Professor Sanjay Banerjee for supplying us with an almost never ending supply of coffee, and Dr. Praveen Pasupathy for letting me bounce any idea off him no matter the topic. I would like to thank all of my previous teachers and professors who enabled me to become a contributing member of society through their dedication to education and mentorship. I'd like to thank my mom, dad, and my sister for their love and support throughout the years. Without their guidance preparing me for my life to come, I would not be where I am today. Lastly, I cannot express how grateful I am for the love and support of my perpetual editor, partner in crime, and wife to be, Heather Schulman. She is always there supporting me when things get tough and encouraging me to pursue worthwhile endeavors that leave a positive impact on society. Heather, I love you and thank you for everything. You have made this accomplishment significantly easier through your presence in my life.

Development of New Experimental Techniques for Studying Transport and Recombination in Organic and Inorganic Thin Film Solar Cells

Christopher Joseph Lombardo, Ph.D.

The University of Texas at Austin, 2011

Supervisor: Ananth Dodabalapur

For more than 20 years, scientists have studied solar cells made from organic semiconductors. Throughout this time, device structures have evolved from bilayer devices to bulk heterojunction (BHJ) devices and even though efficiencies are approaching 10%, scientists still know relatively little about the transport of charge carriers and recombination mechanisms in these materials. Novel structures, based on lateral BHJ solar cells, have proven to be versatile tools to study transport and recombination mechanisms. In addition, these structures can easily be employed by researchers and solar cell manufacturers to determine the quality and measure the improvement of their materials. For these studies, poly(3-hexylthiophene) (P3HT):[6,6]-phenyl C61-butyric acid methyl ester (PCBM) has been employed due to its wide use among researchers as well as potential for commercialization.

DC photocurrent measurements as a function of device length have yielded the mobility-lifetime product and the generation rate of free carriers within these BHJ devices. In addition to these parameters, the recombination rate as a function of light intensity provides information about the mechanisms of recombination. For example, by

measuring the recombination rate as a function of applied electric field and light intensity we have found that recombination is unimolecular in nature and shifts to bimolecular at increased electric field strengths. Additionally, the mobility-lifetime product, generation rate, and recombination mechanism have been studied as a function of applied electric field, illumination spectrum, illumination intensity, etc. This information has provided much insight on physics of the P3HT:PCBM material system which did not exist before these studies.

Table of Contents

List of Figures	x
Chapter 1: Bulk Heterojunction Solar Cells	1
1.1 Introduction	1
1.2 Principals of Operation	2
1.3 OPV Device Structures	10
1.4 Mechanisms of Recombination.....	12
1.5 Outlook	15
Chapter 2: Ambipolar Organic Thin Film Transistors.....	17
2.1 Introduction	17
2.2 Experimental	20
2.3 Results and Discussion	22
2.4 Summary	30
Chapter 3: Derivation and Measurement of the Mobility-Lifetime Product	31
3.1 Introduction	31
3.2 Theory	31
3.3 Experimental and Measurements	35
3.4 Results and Discussion	37
3.5 Summary	41
Chapter 4: Mechanisms of Recombination.....	43
4.1 Introduction	43
4.2 Experimental	45
4.3 Results.....	46
4.4 Mobility-Lifetime Product & Generation Rate.....	49
4.5 Recombination Mechanisms	54
4.6 Conclusion	63

Chapter 5: Majority Carrier Transport in Nanocrystals of Copper Indium Diselenide	64
5.1 Introduction	64
4.2 Experimental	66
5.3 Results and Discussion	69
5.4 Summary	77
References	78
Vita	88

List of Figures

- Figure 1.1: Electronic structure of a bilayer heterojunction device. The donor (D) contacts the higher and the acceptor (A) the lower work function metal, to achieve good hole and electron collection, respectively. Photogenerated excitons can only be dissociated in a thin layer at the heterojunction and thus the device is exciton diffusion limited [10]. Reprinted with permission of Cambridge University Press.....3
- Figure 1.2: Schematic diagram of: a) bilayer solar cell, b) ideally spaced BHJ solar cell, c) realistic BHJ solar cell [16].....3
- Figure 1.3: Electronic structure of a bulk heterojunction device. The donor (D) is blended with the acceptor (A) throughout the whole film. Thus, photogenerated excitons can be dissociated into charges at any place [10]. Reprinted with permission of Cambridge University Press.4
- Figure 1.4: The chemical structure of a) MDMO-PPV, b) P3HT, c) PCPDTBT, d) PCBM, and e) C₇₁-PCBM.5
- Figure 1.5: Morphology of a P3HT:PCBM bulk heterojunction absorber layer [18].6
- Figure 1.6: Mobility and carrier lifetime of MDMO-PPV:PCBM based on the blend concentration [21]. Reprinted from Organic Electronics, Vol. 7, Dennler, G., A.J. Mozer, G. Juska, A. Pivrikas, R. Osterbacka, A. Fuchsbaauer, and N.S. Sariciftci, *Charge carrier mobility and lifetime versus composition of conjugated polymer/fullerene bulk-heterojunction solar cells.*, P. 229, Copyright (2006), with permission from Elsevier.8

Figure 1.7: The chemical structures of PEDOT (left) and PSS (right).....	8
Figure 1.8: Current vs. voltage data for an ITO/PEDOT:PSS/MDMO-PPV:PCBM (~1:4 wt. %)/cathode BHJ photovoltaic devices under illumination, with different metal electrodes. The device was illuminated with a halogen lamp with a power intensity of 80 mW/cm ² [26]. Reprinted with permission from Mihailechi, V.D., P.W.M. Blom, J.C. Hummelen, and M.T. Rispens, <i>Cathode dependence of the open-circuit voltage of polymer:fullerene bulk heterojunction solar cells</i> . Journal of Applied Physics, 2003. 94 (10): p. 6849-6854. Copyright 2003, American Institute of Physics.....	10
Figure 1.9: Structure of a conventional bottom illuminated OPV cell.	11
Figure 1.10: Structure of an inverted bottom illuminated OPV cell.....	12
Figure 1.11: A 120 nm MDMO-PPV:PCBM (20:80 wt %) device at short circuit showing the carrier densities and the net generation rate [8]. From Blom, P.W.M., V.D. Mihailechi, L.J.A. Koster, and D.E. Markov, <i>Device Physics of Polymer:Fullerene Bulk Heterojunction Solar Cells</i> . Advanced Materials, 2007. 19 (12): p. 1551-1566. Copyright Wiley- VCH Verlag GmbH & Co. KGaA. Reproduced with permission. ...	15
Figure 2.1: Schematic a) I_D vs. V_{DS} plot and b) I_D vs. V_G for an example ambipolar OTFT [51]. Reproduced with permission from Zaumseil, J. and H. Sirringhaus, Electron and Ambipolar Transport in Organic Field-Effect Transistors. Chemical Reviews, 2007. 107(4): p. 1296-1323. Copyright 2007 American Chemical Society.	19
Figure 2.2: A schematic diagram of a bottom contact bottom gate ambipolar OTFT.	21

Figure 2.3: Output characteristics of an ambipolar OTFT with a channel length of 10 μm : (top) pFET and (bottom) nFET [56]. Reprinted with permission from Lombardo, C. and A. Dodabalapur, Nongeminate carrier recombination rates in organic solar cells. *Applied Physics Letters*, 2010. 97(23): p. 233302-3. Copyright 2010, American Institute of Physics.23

Figure 2.4: Transfer characteristics of an ambipolar OTFT with a channel length of 10 μm24

Figure 2.5: Output characteristics of an ambipolar OTFT under 81 mW/cm^2 AM1.5g illumination with a channel length of 10 μm : (top) pFET and (bottom) nFET [56]. Reprinted with permission from Lombardo, C. and A. Dodabalapur, Nongeminate carrier recombination rates in organic solar cells. *Applied Physics Letters*, 2010. 97(23): p. 233302-3. Copyright 2010, American Institute of Physics.25

Figure 2.6: Transfer characteristics of an ambipolar OTFT under 81 mW/cm^2 AM1.5g illumination with a channel length of 10 μm26

Figure 2.7: Resistor characteristics of an ambipolar OTFT under 81 mW/cm^2 AM1.5g illumination [56]. Reprinted with permission from Lombardo, C. and A. Dodabalapur, Nongeminate carrier recombination rates in organic solar cells. *Applied Physics Letters*, 2010. 97(23): p. 233302-3. Copyright 2010, American Institute of Physics.27

Figure 2.8: Recombination rate as a function of applied electric field [56]. Reprinted with permission from Lombardo, C. and A. Dodabalapur, Nongeminate carrier recombination rates in organic solar cells. *Applied Physics Letters*, 2010. 97(23): p. 233302-3. Copyright 2010, American Institute of Physics.....29

Figure 3.1: Schematic diagram of a lateral solar cell structure.....32

Figure 3.2: Theoretical plot of lateral current density vs. device length as derived in equation 3.4 for multiple electric fields.34

Figure 3.3: Theoretical plot of normalized current vs. device length as derived in equation 3.5 for multiple electric fields.34

Figure 3.4: Experimental data for the lateral current density vs. electric field for lateral solar cells, in the reverse bias region where carrier injection was suppressed. The set of two curves represents a forward and backward voltage sweep. The inset shows the full range of collected data, which at higher fields have an increasing slope indicative of carrier injection.36

Figure 3.5: Experimental data for the normalized current vs. electric field for lateral solar cells, in the reverse bias region where carrier injection was suppressed. The set of two curves represents a forward and backward voltage sweep. The inset shows the full range of collected data, which at higher fields have an increasing slope indicative of carrier injection.37

Figure 3.6: Lateral current density vs. device length various electric field values for P3HT:PCBM lateral solar cells. Both measured data (points) and numerical fits (lines) are shown.....39

Figure 3.7: Normalized current vs. device length various electric field values for P3HT:PCBM lateral solar cells. Both measured data (points) and numerical fits (lines) are shown.....	40
Figure 3.8: The mobility-lifetime product and the generation rate vs. applied electric field extracted from the lateral current density and the normalized current.	41
Figure 4.1: Current vs. applied electric field data for lateral solar cells with lengths ranging from 3 μm to 20 μm under AM1.5g illumination at 100 mW/cm^2	47
Figure 4.2: Current vs. applied electric field data for lateral solar cells with lengths ranging from 3 μm to 20 μm under 532 nm illumination at 100 mW/cm^2	47
Figure 4.3: Current vs. applied electric field data for a 5 μm lateral solar cell with AM1.5g illumination intensities ranging from 6 mW/cm^2 to 100 mW/cm^2	48
Figure 4.4: Current vs. applied electric field data for a 5 μm lateral solar cell with 532 nm illumination intensities ranging from 5 mW/cm^2 to 500 mW/cm^2	49
Figure 4.5: Mobility-lifetime product vs. light intensity for lateral solar cell devices under AM1.5g illumination with intensities ranging from 6 mW/cm^2 to 100 mW/cm^2	50
Figure 4.6: Mobility-lifetime product vs. light intensity for lateral solar cell devices under 532 nm illumination with intensities ranging from 5 mW/cm^2 to 100 mW/cm^2	51

Figure 4.7: Generation rate vs. light intensity for lateral solar cell devices under AM1.5g illumination for reverse bias electric field strengths on the range $0.75 - 1.5 \times 10^5 \text{ cm}^{-3} \text{ s}^{-1}$ 52

Figure 4.8: Generation rate vs. light intensity for lateral solar cell devices under 532 nm illumination for reverse bias electric field strengths on the range $0.75 - 1.5 \times 10^5 \text{ cm}^{-3} \text{ s}^{-1}$ 53

Figure 4.9: Comparison of the mobility-lifetime product vs. illumination intensity for lateral solar cell devices under AM1.5g and 532 nm illumination. These devices have a reverse bias electric field of $0.75 \times 10^5 \text{ V/cm}$53

Figure 4.10: Comparison of the generation rate vs. illumination intensity for lateral solar cell devices under AM1.5g and 532 nm illumination. These devices have a reverse bias electric field of $0.75 \times 10^5 \text{ V/cm}$54

Figure 4.11: Recombination rate vs. applied electric field for lateral solar cell devices with lengths ranging from $3 \mu\text{m}$ to $20 \mu\text{m}$ under AM1.5g illumination at 100 mW/cm^255

Figure 4.12: Recombination rate vs. applied electric field for lateral solar cell devices with lengths ranging from $3 \mu\text{m}$ to $20 \mu\text{m}$ under 532 nm illumination at 500 mW/cm^256

Figure 4.13: Normalized recombination rate vs. applied electric field for lateral solar cell devices with lengths ranging from $3 \mu\text{m}$ to $20 \mu\text{m}$ under AM1.5g illumination at 100 mW/cm^2 (solid lines) and 532 nm illumination at 500 mW/cm^2 (dotted lines).57

Figure 4.14: Recombination rate vs. light intensity for lateral solar cell devices with lengths ranging from $5 \mu\text{m}$ to $20 \mu\text{m}$ under AM1.5g illumination at a reverse bias electric field of $0.75 \times 10^5 \text{ V/cm}$58

Figure 4.15: Recombination rate vs. light intensity for lateral solar cell devices with lengths ranging from 5 μm to 20 μm under 532 nm illumination at a reverse bias electric field of 0.75×10^5 V/cm.	59
Figure 4.16: Recombination exponent vs. reverse bias electric field for lateral solar cell devices with lengths ranging from 5 μm to 20 μm under AM1.5g illumination with intensities ranging from 6 mW/cm ² to 100 mW/cm ²	60
Figure 4.17: Recombination exponent vs. reverse bias electric field for lateral solar cell devices with lengths ranging from 5 μm to 20 μm under 532 nm illumination with intensities ranging from 5 mW/cm ² to 500 mW/cm ²	61
Figure 5.1: Current vs. voltage characteristics of TBP-Se CIS samples for temperature ranging from 91 K to 333 K.....	69
Figure 5.2: Mott-Schottky plot for CIS nanocrystal schottky diodes measured at room temperature made from TBP-Se CIS and Se ⁰ CIS measured shortly after preparation.	70
Figure 5.3: Majority carrier concentration as a function of temperature from 91 K - 333 K for CIS nanocrystal schottky diodes made from TBP-Se CIS and Se ⁰ CIS measured shortly after preparation.	71
Figure 5.4: Plot of $LN(\sigma)$ vs. $T^{-1/2}$ for TBP-Se CIS nanoparticle samples measured shortly after preparation, TBP-Se CIS nanoparticle samples measured 12 days after preparation, and Se ⁰ CIS nanoparticle samples measured shortly after preparation.....	72
Figure 5.5: Plot of $LN(\sigma)$ vs. $1000/T$ for the aforementioned CIS nanoparticle samples for $T > 150$ K.	74

Figure 5.6: Plot of $LN(\sigma)$ vs. $T^{-1/2}$ for Se^0 CIS nanoparticle samples measured shortly after preparation in the dark and under an AM1.5g spectrum with an illumination intensity of 81 mW/cm^2 75

Figure 5.7: Plot of $LN(\sigma)$ vs. $1000/T$ for the aforementioned samples in the dark and under an AM1.5g illumination spectrum with an intensity of 81 mW/cm^2 for $T > 150 \text{ K}$76

Chapter 1: Bulk Heterojunction Solar Cells

1.1 INTRODUCTION

As fossil fuel prices continue to rise and proven reserves continue to fall, there is an ever-increasing need to develop non-polluting sources of renewable energy. Solar photovoltaic (PV), solar thermal, wind, geothermal, tidal, nuclear, and hydro-electric power generation will all need to be parts of a comprehensive portfolio that can be used in conjunction with new technologies in energy storage, power distribution, energy efficiency, and other areas which are necessary to move to a new clean renewable energy generation and distribution paradigm. Solar photovoltaic cells are unique in this group as they can easily scale from tiny microelectronic power sources to small off-grid installations to utility scale power generation. In addition, PV cells require minimal maintenance, and can easily generate power at approximately the rated value for more than 30 years.

Thin film PV cells are of particular interest to researchers, as they could lead to great cost reduction in the production of PV panels. Currently, the absorber material represents approximately 50% of the production cost of silicon (Si) PV panels [1]. Si cells typically utilize absorber layers that are 100-300 μm thick, whereas thin film cells can absorb the same amount of light with absorber layers that range from 0.1-10 μm . This represents a decrease in absorber layer thickness from 30x-3000x and directly translates to a large decrease in production cost. The absorber layers in thin film cells can be deposited through a variety of processes including vapor deposition, electrochemical processes, spray coating, spin coating, drop coating, screen-printing, inkjet printing, doctor blading, etc. [2-4].

1.2 PRINCIPALS OF OPERATION

Even though thin film PV cells have been studied for over 35 years, very little is known about transport mechanisms and recombination in some of the absorber materials. One class of materials that is of particular interest is organic/polymeric semiconductors due to the ease of solar cell fabrication and potential for highly reduced cost per watt of generated power. Initially, organic photovoltaic (OPV) cells were fabricated in a manner similar to many other thin film architectures with an absorber layer sandwiched between electrodes with differing workfunctions. The power conversion efficiency of such cells was quite low due to the photogeneration of excitons in organic semiconducting materials. These excitons possess binding energies much greater than kT [5-7] so neither the quasi-particles' thermal energy nor the electric field created by the asymmetric electrodes is sufficient to dissociate them [8]. To provide the energy necessary to dissociate excitons, researchers began to use a bilayer of electron donating and electron accepting materials [9]. The energy diagram of this system is much like that of a traditional inorganic Type 2 heterojunction and is shown in Figure 1.1.

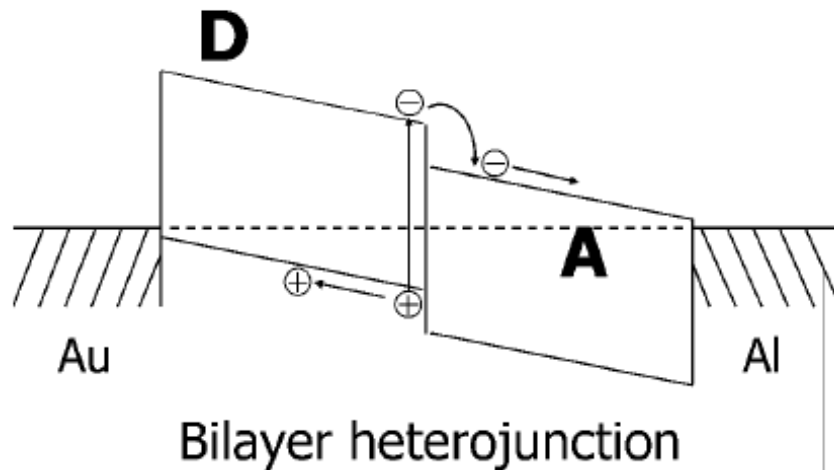


Figure 1.1: Electronic structure of a bilayer heterojunction device. The donor (D) contacts the higher and the acceptor (A) the lower work function metal, to achieve good hole and electron collection, respectively. Photogenerated excitons can only be dissociated in a thin layer at the heterojunction and thus the device is exciton diffusion limited [10]. Reprinted with permission of Cambridge University Press.

In this structure, photons absorbed within one exciton diffusion length of the donor/acceptor (D/A) interface would be dissociated by the energy difference present at the interface. Although bilayer structures greatly improved the efficiency of OPV devices, these structures could never provide an efficiency of much greater than 1% due to the relatively short exciton diffusion length of approximately 1-10 nm [11-15]. A schematic OPV bilayer structure is shown in Figure 1.2.

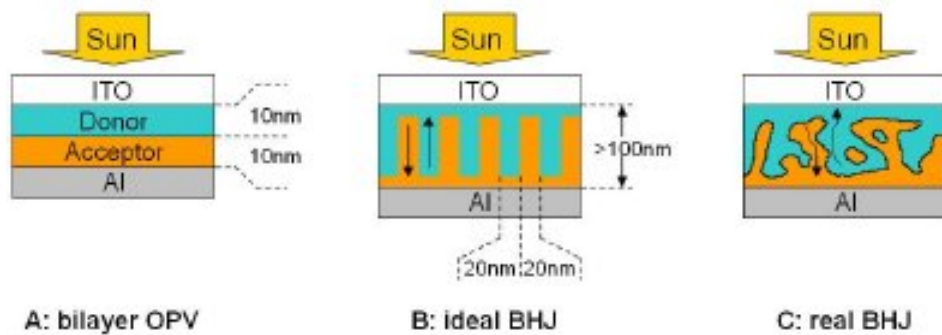


Figure 1.2: Schematic diagram of: a) bilayer solar cell, b) ideally spaced BHJ solar cell, c) realistic BHJ solar cell [16].

In order to increase the efficiency of OPV cells, the fraction of excitons that are transported to the D/A interface before relaxation would need to be increased. This could occur in two ways: increasing the exciton diffusion length or decreasing the distance that the excitons need to travel to the D/A interface without dramatically reducing the amount of photons being absorbed. This precluded making OPV devices with absorber

thicknesses on the range of 1-10 nm due to the reduced absorption thickness. An innovative solution was first reported by *Yu et al.* in 1995 and called a bulk heterojunction (BHJ) [17]. A BHJ is a blend of semiconducting materials that contains both electron donating and electron accepting materials within the same matrix. This provides a nano-structured D/A interface that is present throughout the entire absorber layer. As compared to a bilayer OPV structure, BHJs increase the surface area of the D/A interface by many orders of magnitude and as a result, many more excitons are dissociated within a diffusion length of the D/A interface without dramatically changing the energy diagram, as shown in Figure 1.3. Schematic diagrams of an ideal BHJ structure and a realistic BHJ structure are also shown in Figure 1.2.

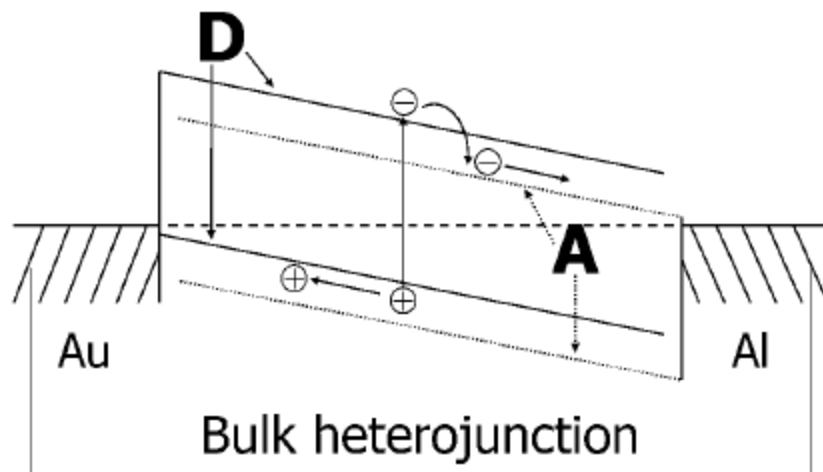


Figure 1.3: Electronic structure of a bulk heterojunction device. The donor (D) is blended with the acceptor (A) throughout the whole film. Thus, photogenerated excitons can be dissociated into charges at any place [10]. Reprinted with permission of Cambridge University Press.

In addition to a nano-structured D/A interface, an effective BHJ layer must include complete electron transporting and hole transporting networks that facilitate the

effective transport of charge carriers from the absorber material to the electrodes. Typically, unlike shown in Figure 1.2, these networks are interpenetrating and both the electron and hole transporting networks extend from the anode to the cathode. In most OPV systems, the electron donating material is a π -conjugated polymer and the accepting material is a chemically modified fullerene, although novel electron accepting materials have been reported on. Some common electron donating materials are poly(2-methoxy-5-(3',7'-dimethyloctyloxy)-*p*-phenylene vinylene) (MDMO-PPV), poly(3-hexylthiophene) (P3HT), and poly[2,6-(4,4-bis-(2-ethylhexyl)-4*H*-cyclopenta[2,1-b;3,4-b']dithiophene)-*alt*-4,7-(2,1,3-benzothiadiazole)] (PCPDTBT) and some common electron accepting materials are [6,6]-phenyl C₆₁-butyric acid methyl ester (PCBM) and [6,6]-phenyl C₇₁-butyric acid methyl ester (C₇₁-PCBM). The chemical structures of these common OPV materials are shown in Figure 1.4.

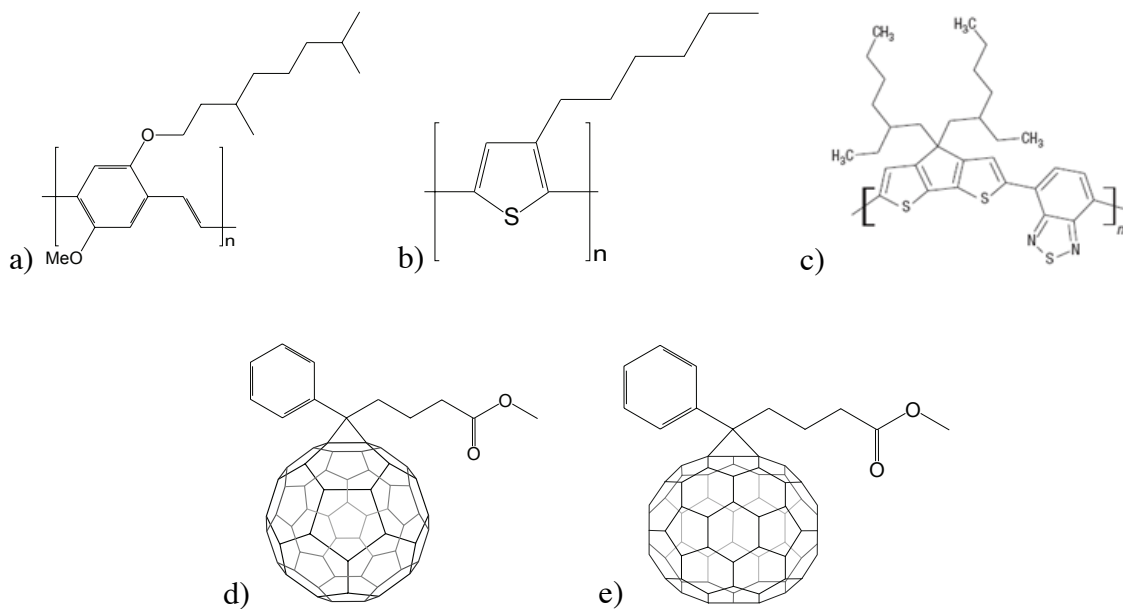


Figure 1.4: The chemical structure of a) MDMO-PPV, b) P3HT, c) PCPDTBT, d) PCBM, and e) C₇₁-PCBM.

To form the BHJ layer, the electron donating and electron accepting materials are mixed together in solution and deposited as one cohesive phase-segregated film. It is through these phase-segregated conduction networks that the free holes and free electrons are transported through the BHJ layer to the electrodes. The morphology of a P3HT:PCBM BHJ absorber layer illustrating the phase-segregated polymer and fullerene domains is shown in Figure 1.5.

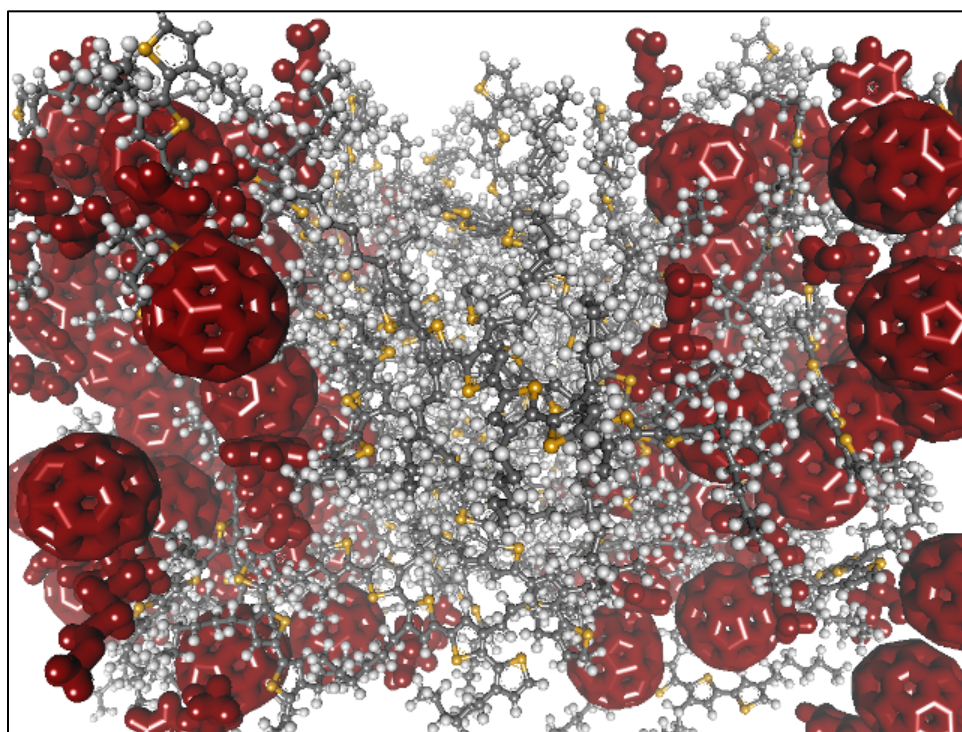


Figure 1.5: Morphology of a P3HT:PCBM bulk heterojunction absorber layer [18].

Since the electrons and holes are no longer excitonically bound after dissociation at the D/A interface, they travel to the electrodes via the electric field that is created between the dissimilar anode and cathode metals. Initially, researchers thought it was sufficient to study how holes traveled through the donor material and how electrons

traveled through the acceptor material. Measurements of the electron mobility in PCBM field effect transistors (FETs) were found to be ~ 4000 times greater than the hole mobility in MDMO-PPV FETs [19]. These measurements did not accurately characterize the BHJ system as the hole mobility of the MDMO-PPV:PCBM blend is higher than hole mobility of a film solely consisting of MDMO-PPV and the mobility in a FETs geometry is much greater than in a solar cell geometry [20]. In fact, the hole mobility in a blend of MDMO-PPV:PCBM varies over two orders of magnitude based on the ratio of MDMO-PPV to PCBM in the blend [21, 22]. This trend continues for the carrier lifetimes as well. A more recent transient measurement technique called photo-CELIV (photo charge extraction in a linearly increasing voltage) [23] is able to independently measure carrier mobilities and lifetimes in solar cell geometries. Hole mobility and lifetime is measured as a function of blend concentration using photo-CELIV is shown in Figure 1.6.

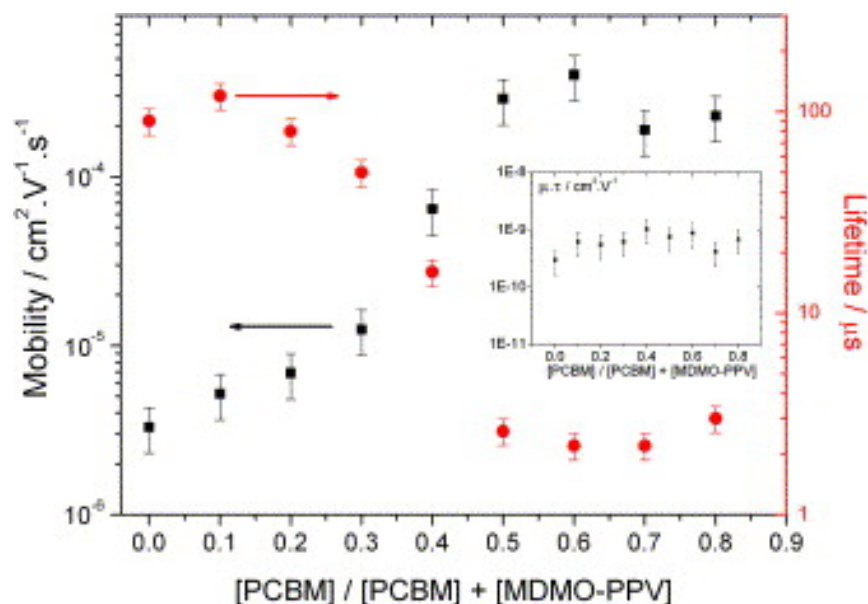


Figure 1.6: Mobility and carrier lifetime of MDMO-PPV:PCBM based on the blend concentration [21]. Reprinted from Organic Electronics, Vol. 7, Dennler, G., A.J. Mozer, G. Juska, A. Pivrikas, R. Osterbacka, A. Fuchsbauer, and N.S. Sariciftci, *Charge carrier mobility and lifetime versus composition of conjugated polymer/fullerene bulk-heterojunction solar cells.*, P. 229, Copyright (2006), with permission from Elsevier.

After the charges have traversed the BHJ layer, they are collected at the electrodes. Asymmetric electrode metals create an electric field that causes electrons (holes) to drift toward the cathode (anode). To help prevent recombination at the anode, a hole transport layer (HTL) is typically placed between the BHJ and the anode. A HTL facilitates hole transport while blocking the flow of electrons. The most commonly used HTL is poly(3,4-ethylenedioxythiophene) doped with poly(styrenesulfonate) (PEDOT:PSS) which is a highly conductive polymer. In addition to serving as the HTL, PEDOT:PSS energetically acts as the hole extracting anode in conjunction with another high workfunction metal used to collect holes and transport them away from the OPV cell. The chemical structures of PEDOT and PSS are shown in Figure 1.7.

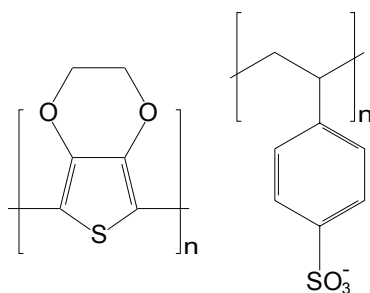


Figure 1.7: The chemical structures of PEDOT (left) and PSS (right).

An electron transport layer (ETL) can also be used to reduce carrier recombination at the cathode. Even though most conventional OPV structures do not

utilize an ETL, *Hau et al.* have reported on the successful use of nanoparticles of zinc oxide (ZnO) as an ETL in an inverted OPV structure [24, 25].

In addition to the HTL and ETL, the choice of cathode material makes an impact on OPV device characteristics. Typically in metal-insulator-metal structures, the workfunction difference between the two different metals would approximate the open circuit potential (V_{oc}). However when the metal workfunction aligns with either the lowest unoccupied molecular orbital (LUMO) of the acceptor material or with the highest occupied molecular orbital of the donor material, charge transfer of electrons or holes results in the pinning of the Fermi level at the LUMO or HOMO levels respectively. (For polymeric materials, the HOMO is analogous to the π band and the LUMO is analogous to the π^* band.) In this circumstance, V_{oc} is governed by the energy difference between the donor and acceptor materials with the maximum possible V_{oc} being the difference between the LUMO of the acceptor material and the HOMO of the donor material, $V_{oc} \leq LUMO_A - HOMO_D$. Figure 1.8 shows current versus voltage data for MDMO-PPV:PCBM solar cells under 80 mW/cm² illumination with cathode metals of palladium, gold, silver, and aluminum with a ~ 1 nm interfacial layer of lithium fluoride (LiF). As the workfunction of the metal decreases, V_{oc} increases as well as the short circuit current (J_{sc}).

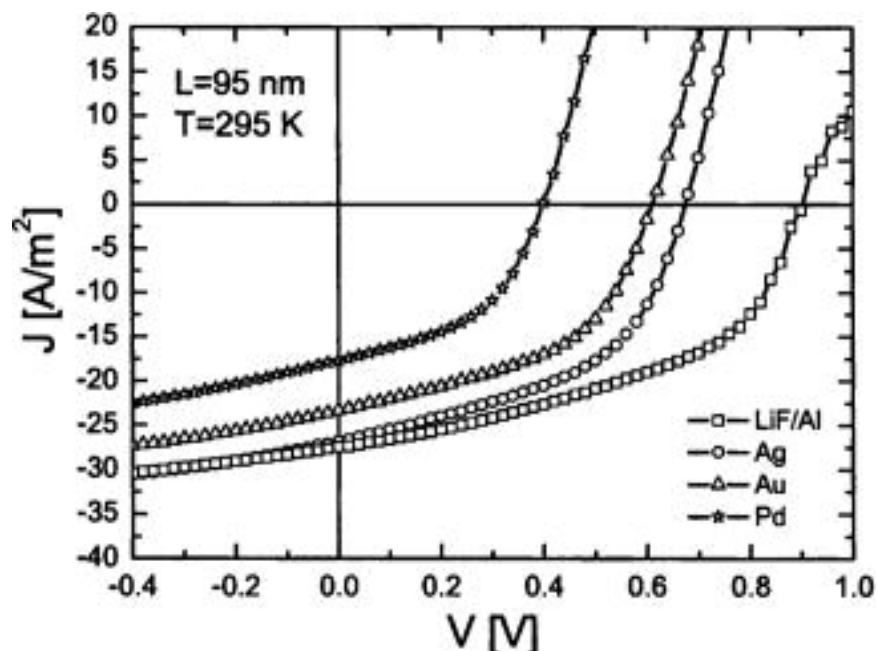


Figure 1.8: Current vs. voltage data for an ITO/PEDOT:PSS/MDMO-PPV:PCBM (~1:4 wt. %)/cathode BHJ photovoltaic devices under illumination, with different metal electrodes. The device was illuminated with a halogen lamp with a power intensity of 80 mW/cm² [26]. Reprinted with permission from Mihailetchi, V.D., P.W.M. Blom, J.C. Hummelen, and M.T. Rispens, *Cathode dependence of the open-circuit voltage of polymer:fullerene bulk heterojunction solar cells*. Journal of Applied Physics, 2003. **94**(10): p. 6849-6854. Copyright 2003, American Institute of Physics.

1.3 OPV DEVICE STRUCTURES

A conventional OPV cell is bottom illuminated which means that it is illuminated through a transparent substrate, usually made of glass or thin plastic such as polyethylene naphthalate (PEN). The substrate is usually coated with a transparent high workfunction anode such as indium tin oxide (ITO). To prevent recombination at the anode, a HTL of PEDOT:PSS is deposited via a solution coating technique to a thickness of 10-100 nm. PEDOT:PSS is optically transparent to the wavelengths of light that are most commonly absorbed by the BHJ absorber layer. The BHJ absorber layer is made of a mixture of electron donating and electron accepting materials and is also deposited by solution to a

thickness of 50-200 nm. Lastly a low workfunction metal such aluminum or calcium is deposited to effectively collect electrons. Figure 1.9 shows a conventional bottom illuminated OPV cell structure.

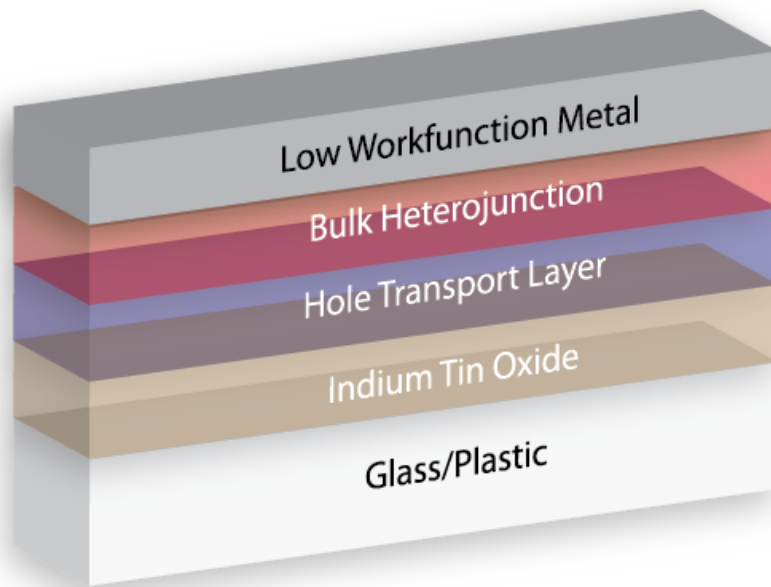


Figure 1.9: Structure of a conventional bottom illuminated OPV cell.

An inverted bottom illuminated structure effectively utilized by *Hau et al.* also starts with a glass or plastic substrate. In this particular case, a layer of ZnO nanoparticles has been used as an ETL [24, 25] but there are potentially other materials that could serve as an ETL. The BHJ is deposited on top of the ETL followed by a HTL made of PEDOT:PSS. Finally, a high workfunction anode such as gold or silver is deposited. Figure 1.10 shows an inverted bottom illuminated OPV structure. Alternative top illumination OPV structures have been proposed but face difficulties due to the necessity of a low resistance transparent electrode for effective charge collection.

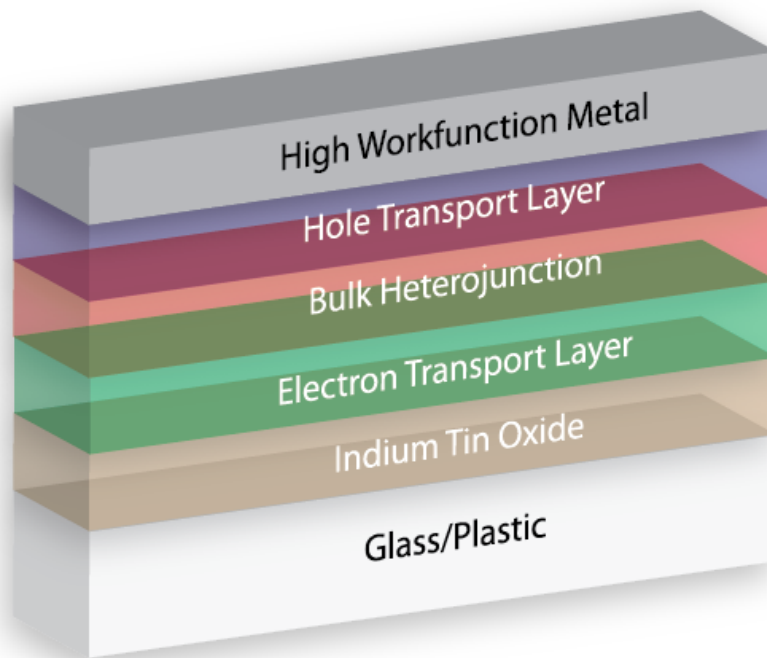


Figure 1.10: Structure of an inverted bottom illuminated OPV cell.

1.4 MECHANISMS OF RECOMBINATION

In OPV cells, the most common recombination mechanism is non-radiative recombination. In doped crystalline semiconductors, the recombination rate U , is a function of the minority carrier concentration and has the form $U = \frac{n}{\tau}$, where n is the minority carrier concentration (for p-type semiconductors) and τ is the lifetime of charge carriers. (In the case of an n-type semiconductor, holes would be the minority carrier.) This is a result of there being a concentration of majority carriers that is many orders of magnitude greater than that of the minority carriers. In the perspective of the minority carrier there are “infinitely” many majority carriers to recombine with. As a result, finding a majority carrier to recombine with at the end of the minority carrier’s lifetime is

a “guaranteed” as there are limitless numbers of majority carriers. This type of recombination is also referred to as unimolecular.

Bimolecular recombination occurs when each carrier type has approximately the same concentration, which is unlike what is typically seen in traditional doped semiconductors. When there are comparable populations of each carrier type (hole and electrons), either carrier can recombine to diminish the population of mobile charge carriers. Bimolecular recombination has the form $U = Bnp$, where B is the coefficient of bimolecular recombination and n and p are the concentrations of electrons and holes respectively. There exists a special case of bimolecular recombination proposed by *Langevin* where the recombination rate is dependent on the mobilities of the charge carriers [27]. Here the recombination coefficient is Langevin-type with $B_L = \frac{e(\mu_p + \mu_n)}{\epsilon_r \epsilon_0}$, where μ is the carrier’s mobility and ϵ is the dielectric constant of the semiconducting material [28]. The concept within Langevin-type recombination is that for low mobility (highly disordered) systems, it is uncertain whether two carriers of opposite polarity will be in the vicinity of one another. Regardless of a carrier’s lifetime, if it is unable to find a carrier of opposite polarity to recombine with, it will remain in an excited mobile state. A result of this is that as the carrier’s mobility increases, so does the recombination rate. This contrast between Langevin and non-Langevin recombination has been seen experimentally by comparing OPV cells made from MDMO-PPV:PCBM and P3HT:PCBM [29]. By using various transient photocurrent measurement techniques, *Pivrikas et al.* have shown that $B/B_L \approx 1$ for OPV cells made from MDMO-PPV:PCBM which indicated Langevin-type recombination and $B/B_L \approx 10^{-4}$ for OPV cells made from P3HT:PCBM, which indicates the Langevin-type recombination is strongly suppressed. The reason for this different recombination type is the result of differences in the nano-morphology between MDMO-PPV:PCBM and P3HT:PCBM which leads to

better ordering in P3HT:PCBM. One important property of P3HT is its ability to maintain the microcrystalline structure present in pristine films even when mixed with fullerenes in a BHJ absorber layer [30] which facilitates better charge carrier transport as compared to MDMO-PPV.

Recombination in an OPV cell need not take place via only one mechanism throughout the entire device structure and should be dependent on the relative electron and hole concentrations. The electron and hole carrier concentrations and the net carrier generation rate (U in this instance only), defined as the generation rate – the recombination rate, are shown in Figure 1.11 [8]. These quantities are calculated from numerical simulations as a function of position for a 120 nm thick MDMO-PPV:PCBM (1:4 wt %) OPV cell at short circuit conditions. These simulations assume Langevin-type bimolecular recombination, a mobility difference of one order of magnitude with the electrons being the faster carrier, and the cathode located at $x = 0$.

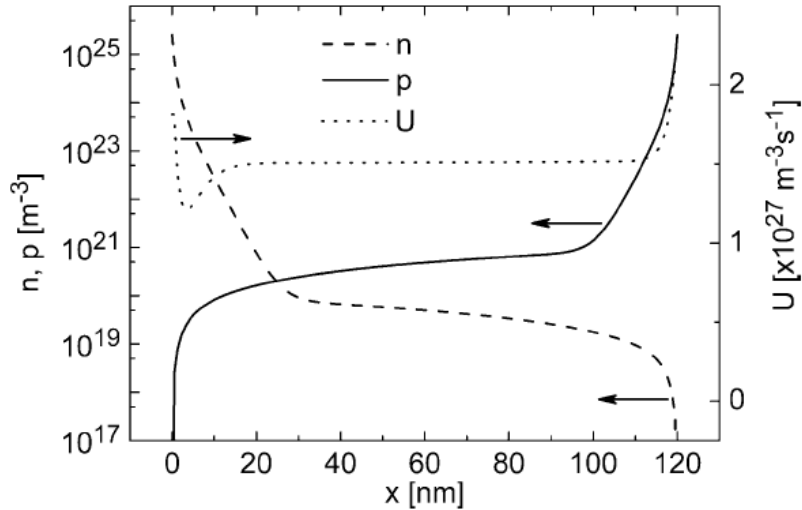


Figure 1.11: A 120 nm MDMO-PPV:PCBM (20:80 wt %) device at short circuit showing the carrier densities and the net generation rate [8]. From Blom, P.W.M., V.D. Mihailetschi, L.J.A. Koster, and D.E. Markov, *Device Physics of Polymer:Fullerene Bulk Heterojunction Solar Cells*. Advanced Materials, 2007. **19**(12): p. 1551-1566. Copyright Wiley-VCH Verlag GmbH & Co. KGaA. Reproduced with permission.

In the bulk of the device, the carrier concentrations are appropriately one order of magnitude different with residual hole accumulation which agrees well with the mobility difference used as an input parameter. The residual carrier accumulation creates a “quasi majority carrier-like case” for holes and a “quasi minority carrier-like case” for electrons. The terms “quasi majority carrier” and “quasi minority carrier” are terms that we have introduced to describe a slower carrier that creates an accumulation layer within a device and a faster carrier that quickly exists a device respectively. The creation of a hole accumulation layer and quasi majority and quasi minority carriers raises doubt about the use of bimolecular recombination in the numerical simulation. The use of unimolecular recombination or a combination of unimolecular and bimolecular recombination may be a more appropriate choice. The mechanisms of recombination and the regimes in which each mechanism is applicable will be further discussed in Chapter 4. P3HT:PCBM also exhibits asymmetry in the carrier mobility [31] and as a result, similar questions exist about its mechanisms of recombination.

1.5 OUTLOOK

It is clear that significant work has been done to study charge transport and recombination in OPV materials. Old and new experimental techniques such as time of flight (TOF) [32, 33], CELIV [23, 34-36] and photo-CELIV [37, 38], double injection (DI) [39-44], and plasma extraction [45] have been developed or redefined to specifically

to study recombination, carrier mobilities, etc. as a function of electric field, light intensity, and temperature. Although researchers have learned about many characteristics of charge transport from these measurements, there are still many questions that need to be addressed and assumptions that may not be accurate and need to be revisited. Many researchers assume bimolecular recombination is the only recombination mechanism but there is evidence that unimolecular recombination plays a role in these devices. In addition, many researchers assume that the electron and hole concentrations are equal in the OPV device but *Blom et al.* [8] and other researchers have simulated and experimental evidence that steady-state carrier concentrations are unequal creating quasi majority and quasi minority carriers within OPV devices. In order to study these questions further, we have developed new experimental techniques using novel lateral solar cell structures to probe the transport of charge carriers as well as recombination mechanisms in ways that have not been previously reported.

Chapter 2: Ambipolar Organic Thin Film Transistors

2.1 INTRODUCTION

Ambipolar transistors can be made with bulk heterojunction systems that are the principal subject of this dissertation. An investigation of the operational characteristics of such transistors yields insight into charge transport phenomena such as the electron and hole mobilities and also the nature of electrical contacts. We can also combine ambipolar field-effect transistor (FET) measurements with optoelectronic characterization under solar illumination to evaluate non-geminate carrier recombination rates. To study such non-geminate recombination rates, we employ ambipolar organic thin film transistors (OTFTs) together with planar photoresistor structures. Ambipolar OTFTs have been studied by multiple researchers in dark conditions [8, 29, 46-48]. We can build upon such studies to learn more about charge transport by performing experiments under illumination. Although a few studies of these ambipolar devices under illumination have been reported [49], a detailed analysis of transport or recombination based upon such measurements had not been done. We have performed such studies on ambipolar OTFTs with donor-acceptor active semiconductor layers as well as lateral photoresistor structures that are not gated. The active layers are a blend of poly(3-hexylthiophene) (P3HT) and [6,6]-phenyl C₆₁-butyric acid methyl ester (PCBM) deposited just as in typical organic solar cells [50]. We note that the morphology of the active semiconductor film in a field effect transistor (FET) geometry is different from that of a typical solar cell geometry, and this could place limits on the interpretation of these results with reference to charge transport in solar cells. Nevertheless, a wealth of information is available from FET-based and lateral measurements, despite the material

organization and transport direction being potentially different in FET devices and solar cells.

Ambipolar OTFTs are different from typical FETs as they can operate in both p-channel mode and n-channel modes. This is a result of the ability of the semiconducting material to effectively transport both electrons and holes. Ambipolar OTFTs operate in a manner similar to traditional unipolar OTFTs with a few exceptions. By looking at schematic I_D vs. V_{DS} measurements, it is shown that for small gate bias the current is diode-like as a result of minority carrier injection from the drain. At moderate gate bias, the applied gate voltage begins to drive minority carriers out of the channel and accumulate majority carriers. The I_D vs. V_{DS} curves look like commonly seen FET curves with “linear” and “saturation” regions except that at high source-drain bias, the device comes out of “saturation” as the source-drain electric field overcomes the effect of the electric field produced by the gate bias. Minority carriers begin to flow through the channel again and the I_D vs. V_{DS} characteristics become diode-like again. As the gate bias continues to increase, the FET curves again show the familiar “linear” and “saturation” characteristics. Schematic transfer characteristics show ambipolar currents at low gate bias which decrease with increasing gate bias as minority carriers are pushed out of the channel. After a transition point in the gate voltage sweep, the minority carriers have been sufficiently depleted and majority carriers begin to accumulate, thus increasing either the electron or hole currents (depending on the mode of operation). Schematic ambipolar OTFT output and transfer characteristics are shown in Figure 2.1.

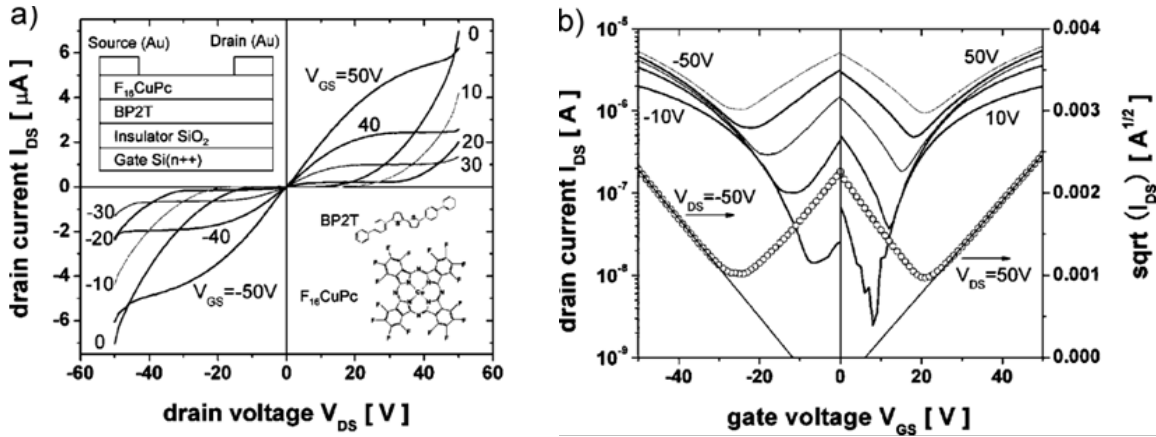


Figure 2.1: Schematic a) I_D vs. V_{DS} plot and b) I_D vs. V_G for an example ambipolar OTFT [51]. Reproduced with permission from Zaumseil, J. and H. Sirringhaus, Electron and Ambipolar Transport in Organic Field-Effect Transistors. Chemical Reviews, 2007. 107(4): p. 1296-1323. Copyright 2007 American Chemical Society.

To determine recombination rates and characterize other parameters of interest in this system, three basic measurements are made: the output characteristic and the transfer characteristic (for both pFET and nFET modes), and a resistor characteristic (a two-terminal ungated I-V sweep). These parameters must be measured both in the dark and under illumination, preferably AM1.5. From the transfer characteristics, the dark electron and hole mobilities can be found using the known equation for drain current,

$$I_D = \mu C_{ox} \frac{W}{L} \left((V_{GS} - V_{th}) V_{DS} - \frac{V_{DS}^2}{2} \right) \quad (2.1)$$

in the linear region of the FET. Using the slope of the resistor characteristic curve and the device geometry, the conductivity can also be obtained. The electron and hole mobilities under illumination can be extracted from transfer curves and the conductivity under illumination can be extracted from the resistor characteristic. Combining these parameters, we extract the excess carrier concentration as the expression for the photocurrent becomes:

$$\vec{j} = \sigma \vec{E} \quad (2.2)$$

where

$$\sigma_{ph} = q(\Delta n(\mu_{e,ph} + \mu_{h,ph}) + n_e \mu_{e,ph} + n_h \mu_{h,ph}) \quad (2.3)$$

Under illumination we assumed that the number of photogenerated electrons and the number of photogenerated holes must be equal so $\Delta n_e = \Delta n_h = \Delta n$. As a result of photocurrent measurements in lateral solar cells, we now know that this assumption is invalid at electric fields below $1 - 3 \times 10^5$ V/cm. Since the electron mobility and the hole mobility are unequal, the photocurrent will be dominated by the carrier with higher mobility. This will be discussed in more detail in Chapter 4. One additional assumption is that the carrier mobilities obtained from the FET measurements are the same as those under illumination.

2.2 EXPERIMENTAL

Ambipolar OTFTs were prepared using a standard bottom-gate, bottom-contact geometry with a p-Si substrate and 2000 Å of thermally grown silicon dioxide. Source and drain electrodes were defined through photolithography with device channel lengths ranging from 3 µm to 100 µm. The W/L was 1000 for all devices with channel lengths of 50 µm and smaller, while the 100 µm channel length devices had a W/L of 500. Aluminum was chosen for its ability to effectively inject both electrons and holes in the BHJ [52], and was thermally evaporated to a final thickness of 500 Å. To form the BHJ absorber layer, *Plextronics Plexcore PV 1000*, which is a commercially available P3HT:PCBM solution, was spun-cast at 1000 rpm for 60 seconds and annealed on a hot

plate at 140° C for 20 minutes in a nitrogen atmosphere. A schematic diagram of a bottom contact bottom gate ambipolar OTFT is shown in Figure 2.2.

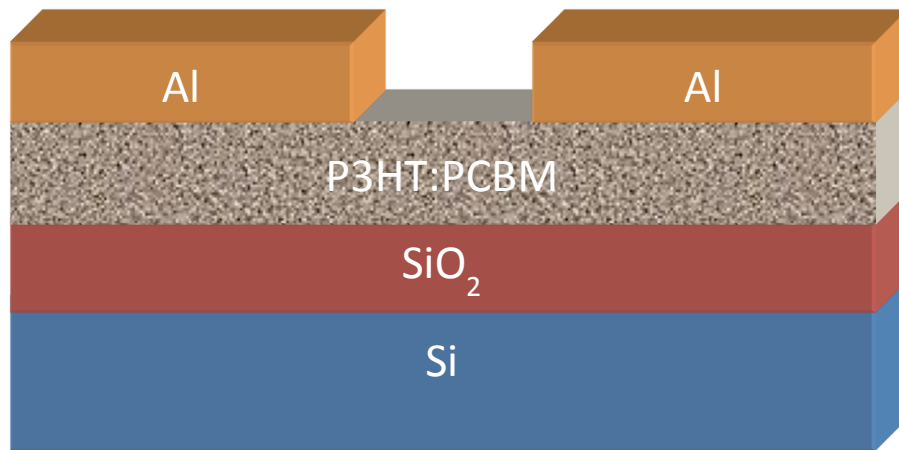
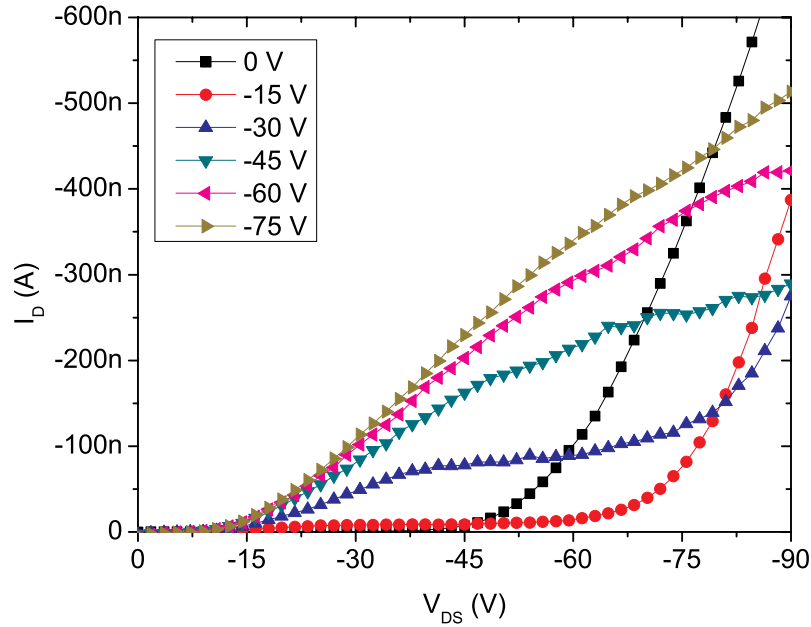


Figure 2.2: A schematic diagram of a bottom contact bottom gate ambipolar OTFT.

Measurements were performed in a *Desert Cryogenics* cryogenic probe station under vacuum better than 10^{-3} Torr. All electrical measurements were performed using an *Agilent 4155C* semiconductor parameter analyzer. When necessary, sample illumination was provided by an *Oriel Model 66907 and 66912* arc lamp using a 150 W ozone-free xenon lamp. The output spectrum was modified using an AM1.5g spectrum filter and the illumination intensity was 81 mW/cm². Typical output characteristics and transfer characteristics were measured in the dark and under 81 mW/cm² AM1.5g illumination for the ambipolar OTFTs in both pFET and nFET modes. In addition, current vs. voltage characteristics were measured with the gate disconnected both with and without illumination.

2.3 RESULTS AND DISCUSSION

Output characteristics and transfer characteristics are shown in Figure 2.3 and Figure 2.4 respectively, from an ambipolar OTFT with a channel length of $10\ \mu\text{m}$ and $W/L = 1000$. Typical ambipolar OTFT characteristics are seen with a diode-like current existing for low gate bias. As gate bias increases, the familiar linear and saturation characteristics are observed [51-55]. At increased source-drain bias, there is the onset of the diode-like current resulting from the opposite carrier type being injected as a result of the high electric field at the contacts. Dark linear mobilities are calculated for $|V_{DS}| = 30$, resulting in a hole mobility of $3.9 \times 10^{-6}\ \text{cm}^2/\text{V} \cdot \text{s}$ and an electron mobility of $7.8 \times 10^{-6}\ \text{cm}^2/\text{V} \cdot \text{s}$.



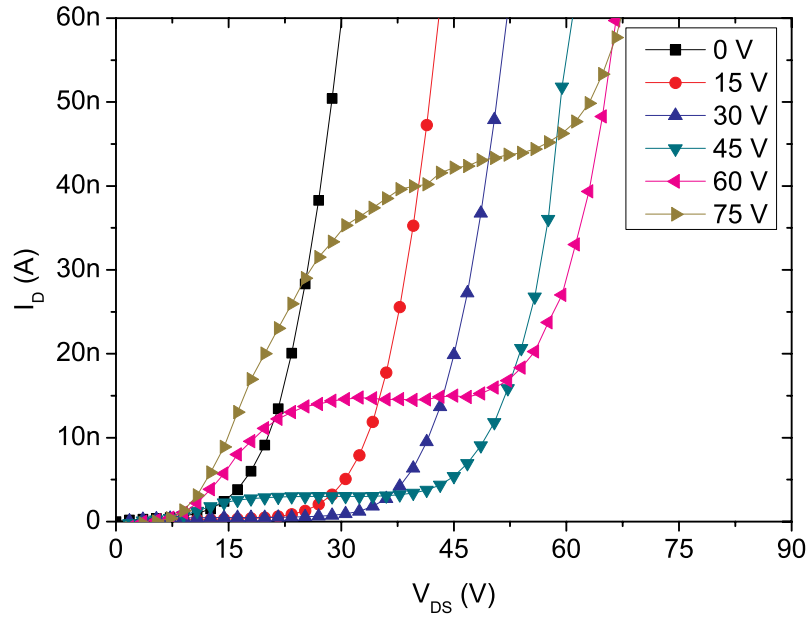


Figure 2.3: Output characteristics of an ambipolar OTFT with a channel length of 10 μm : (top) pFET and (bottom) nFET [56]. Reprinted with permission from Lombardo, C. and A. Dodabalapur, Nongeminate carrier recombination rates in organic solar cells. *Applied Physics Letters*, 2010. 97(23): p. 233302-3. Copyright 2010, American Institute of Physics.

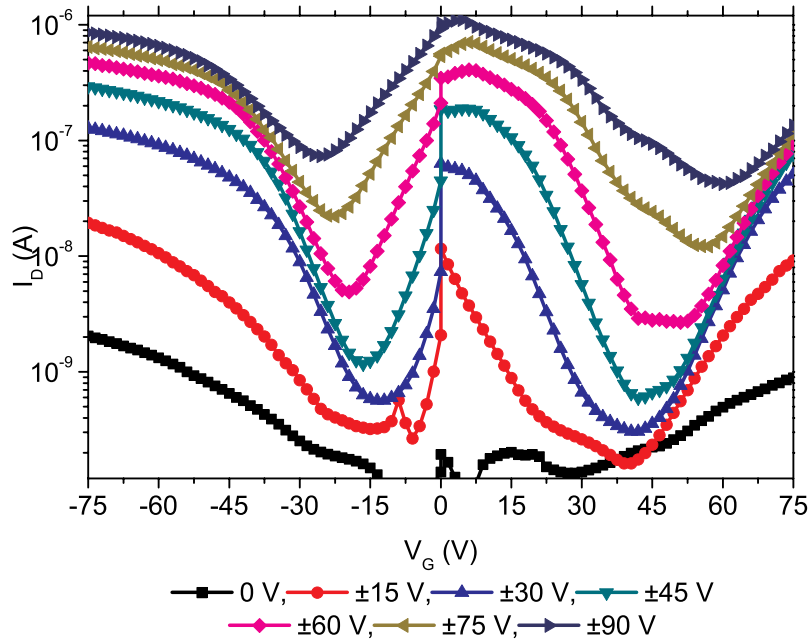
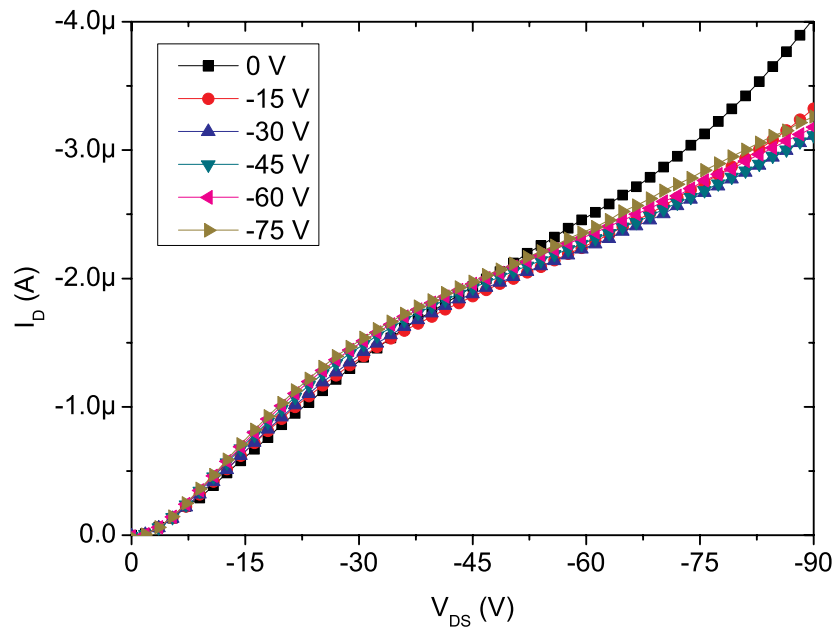


Figure 2.4: Transfer characteristics of an ambipolar OTFT with a channel length of 10 μm .

Output characteristics and transfer characteristics are shown in Figure 2.5 and Figure 2.6 respectively, from the previous ambipolar OTFT under 81 mW/cm^2 AM1.5g illumination. Under illumination, there are parallel conduction pathways: the interfacial channel due to the field induced charge, and the photogenerated charges throughout the thickness of the film. The data shows gate modulation due to an applied voltage bias, which permits us to extract the carrier mobility under illumination. Linear mobilities are calculated for $|V_{DS}| = 30$ resulting in a hole mobility of $3.8 \times 10^{-6} \text{ cm}^2/\text{V} \cdot \text{s}$ and an electron mobility of $3.2 \times 10^{-5} \text{ cm}^2/\text{V} \cdot \text{s}$.



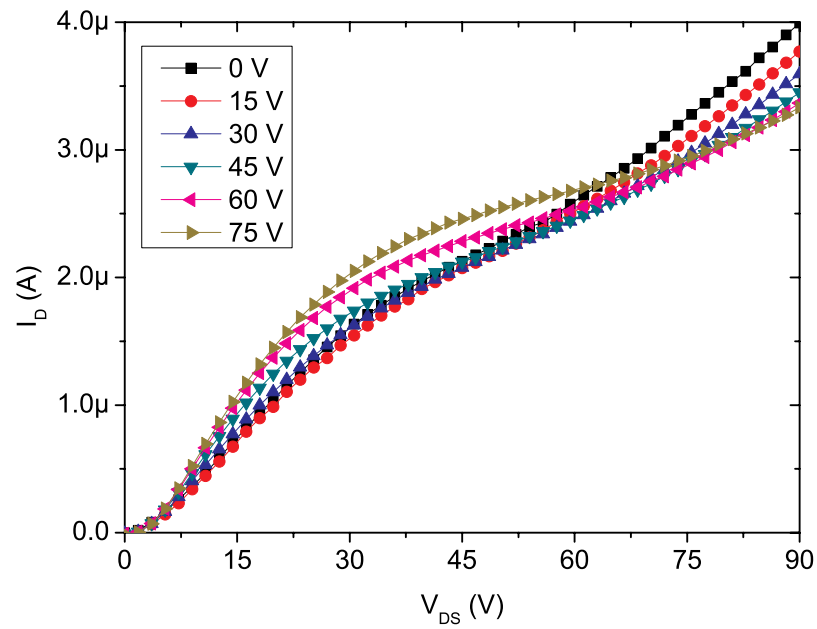


Figure 2.5: Output characteristics of an ambipolar OTFT under 81 mW/cm² AM1.5g illumination with a channel length of 10 μ m: (top) pFET and (bottom) nFET [56]. Reprinted with permission from Lombardo, C. and A. Dodabalapur, Nongeminate carrier recombination rates in organic solar cells. Applied Physics Letters, 2010. 97(23): p. 233302-3. Copyright 2010, American Institute of Physics.

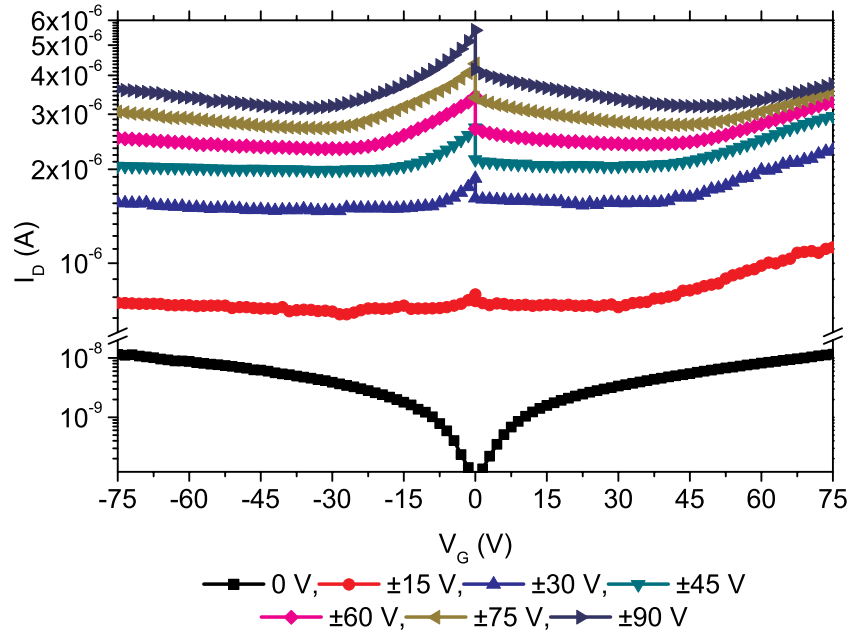


Figure 2.6: Transfer characteristics of an ambipolar OTFT under 81 mW/cm^2 AM1.5g illumination with a channel length of $10 \text{ }\mu\text{m}$.

Resistor characteristics for channel lengths ranging from $3 \text{ }\mu\text{m}$ to $20 \text{ }\mu\text{m}$ are shown in Figure 2.7. The conductivity under illumination for the $10 \text{ }\mu\text{m}$ channel length device at $V_{DS} = 30$ is $3.6 \times 10^{-6} \text{ S/cm}$. Using the electron mobility, hole mobility, and the conductivity under illumination and assuming that the carrier concentration under illumination is much greater than the carrier concentration in the dark and the number of photogenerated electrons and holes is equal, we can assume that the excess carrier concentration is approximately equal to the total number of electrons or holes. For the device parameters specified, we have calculated an excess carrier concentration of $5.8 \times 10^{17} \text{ cm}^{-3}$. Despite this, the photoinduced sheet carrier concentration is greater than the field-induced sheet carrier concentration.

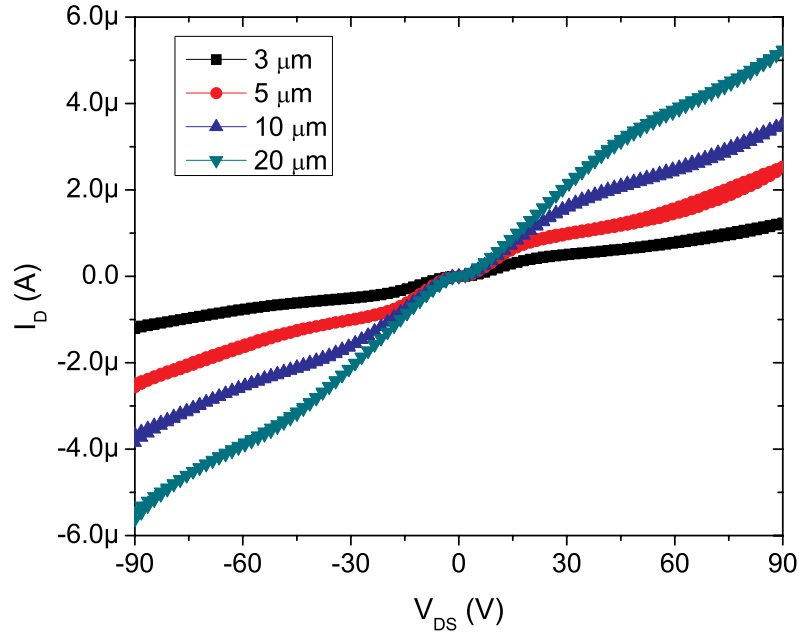


Figure 2.7: Resistor characteristics of an ambipolar OTFT under 81 mW/cm² AM1.5g illumination [56]. Reprinted with permission from Lombardo, C. and A. Dodabalapur, Nongeminate carrier recombination rates in organic solar cells. *Applied Physics Letters*, 2010. 97(23): p. 233302-3. Copyright 2010, American Institute of Physics.

To evaluate the recombination rates in these BHJ films, the photoresistor data for multiple channel lengths shown in Figure 2.7 needs to be suitably scaled. As most of the channel lengths have a constant W/L and, as a result, a different area for photon absorption, the photocurrent data was normalized to the absorption area. This can also be seen as a result of the continuity equation in steady state. By appropriately modifying this equation for electrons or holes we find that

$$\frac{I_D}{LW} = \pm qT(G - U) \quad (2.4)$$

where I_D is the resistor photocurrent, L , W , and T are the channel length, width, and thickness, and G and U are the generation and recombination rates. This result shows that the photocurrent in steady state conditions is proportional to the number of

photogenerated carriers minus the number of carriers that recombine. The generation rate is constant per unit area whereas as the recombination rate is critically dependent on the electrode spacing and electric field. It is this length dependence that allows for the extraction of recombination information from the normalized photocurrent at a given electric field. The photocurrent is linearly dependent on the applied field ($\vec{J} = \sigma\vec{E}$) since it is flowing laterally through the photoresistor. Figure 2.8 shows the recombination rate as a function of applied electric field for channel lengths ranging from 3 μm to 100 μm calculated using the above expression. The data shows that as the applied field increases, the non-geminate recombination rate decreases since the carrier velocity is higher. At lower fields, the carrier velocity is much lower which leads to carriers spending more time in the channel thus increasing the recombination rate. As the applied field approaches zero, there are very few carriers that transport out of the device before recombining. In this regime, contact effects are also present.

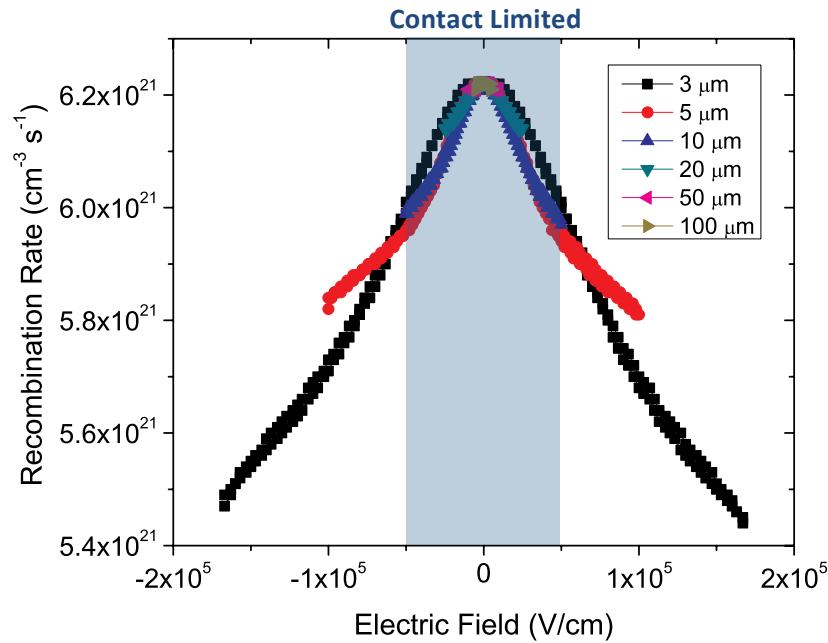


Figure 2.8: Recombination rate as a function of applied electric field [56]. Reprinted with permission from Lombardo, C. and A. Dodabalapur, Nongeminate carrier recombination rates in organic solar cells. *Applied Physics Letters*, 2010. 97(23): p. 233302-3. Copyright 2010, American Institute of Physics.

A typical OPV device has a built in electric field of approximately 10^5 V/cm and recombination rates of $5.7 \times 10^{21} \text{ cm}^{-3} \text{ s}^{-1}$ and $5.9 \times 10^{21} \text{ cm}^{-3} \text{ s}^{-1}$ at 10^5 V/cm have been calculated for the 3 μm and 5 μm devices respectively. Unimolecular recombination is a process that occurs when a system is dominated by one carrier type (majority carriers) and recombination is a function of the minority carrier concentration and the minority carrier lifetime. Bimolecular recombination occurs when there are approximately equal majority and minority carrier concentrations. Here recombination processes are based on the concentrations of both carrier types and recombination rates are typically significantly higher than in systems where unimolecular recombination prevails. Chapter 4 will present the conditions in which unimolecular and bimolecular recombination are valid for P3HT:PCBM lateral solar cell devices.

To find the bimolecular recombination coefficient, we use the expression for the recombination rate:

$$U = Bnp = B\Delta n^2 \quad (2.5)$$

Combining the recombination rate and the continuity equation yields an expression for the bimolecular recombination coefficient,

$$B = \frac{1}{\Delta n^2} \left(G - \frac{I_D}{qLWT} \right) \quad (2.6)$$

as a function of measured parameters, device geometry, and the generation rate. Using this expression and the recombination information located in Figure 2.8, the bimolecular recombination coefficient is estimated to be approximately $1.7 \times 10^{14} \text{ cm}^3/\text{s}$ for a

device length of 3 μm . If the system were to exhibit unimolecular recombination, using $U = \frac{\Delta n_{min}}{\tau_{min}}$, where Δn_{min} is the minority carrier concentration, the minority carrier lifetime τ_{min} would be approximately 100 μs .

2.4 SUMMARY

Lateral ambipolar OTFT structures have been used to study recombination in OPV materials. By measuring the output characteristic, transfer characteristic, and resistor characteristic of these devices under dark and illumination conditions, we have determined some of the material parameters for the P3HT:PCBM material system that are useful in analyzing solar cells. Using these material parameters, an excess carrier concentration of $5.8 \times 10^{17} \text{ cm}^{-3}$ has been calculated. Through studying the electric field dependence of the recombination rate, we have determined that recombination decreases as the electric field increases and the bimolecular recombination coefficient is approximately $1.7 \times 10^{14} \text{ cm}^3/\text{s}$.

Chapter 3: Derivation and Measurement of the Mobility-Lifetime Product

3.1 INTRODUCTION

Researchers have employed a multitude of methods to study transport and recombination in bulk heterojunction (BHJ) solar cells including: photo-generated charge extraction in a linearly increasing voltage (photo-CELIV) [57], ambipolar thin film transistors [56], and transient photocurrents [58], to name a few. Measurement of the mobility-lifetime product in BHJ solar cells is an important parameter for such photovoltaic materials, but has not been adequately studied so far. In this letter, we report on such measurements and employ lateral structures, which are suitable for measuring drift lengths of several microns with uniform illumination.

Researchers who study photodetectors of various types have used methods developed by Karl Hecht to determine the efficiency of these detectors [59]. Hecht's original derivation for charge collection was for a vertical photodetector where individual photons pass through a semi-transparent electrode and photogenerate electrons and holes, which then travel through the photodetector and are collected at the electrodes. This derivation has been used to characterize many types of vertical photodetectors including: amorphous silicon [60], cadmium zinc telluride [61-63], single crystals of β -metal-free phthalocyanine [64], and 2-(4'-octylphenyl)-6-dodecyoxynaphthalene [65]. Hecht's derivation has to be modified for the lateral solar cell structures under steady state illumination that we employ.

3.2 THEORY

Consider the charges collected per unit time (*i.e.* current), as a result of photogeneration, at position x over a thickness dx in a lateral semiconducting device,

shown schematically in Figure 3.1. In the absence of recombination losses, the current dI collected from this small volume equals $q G T W dx$, where q is the elementary charge, G is the generation rate, T is the thickness of the semiconductor, and W is the device width.

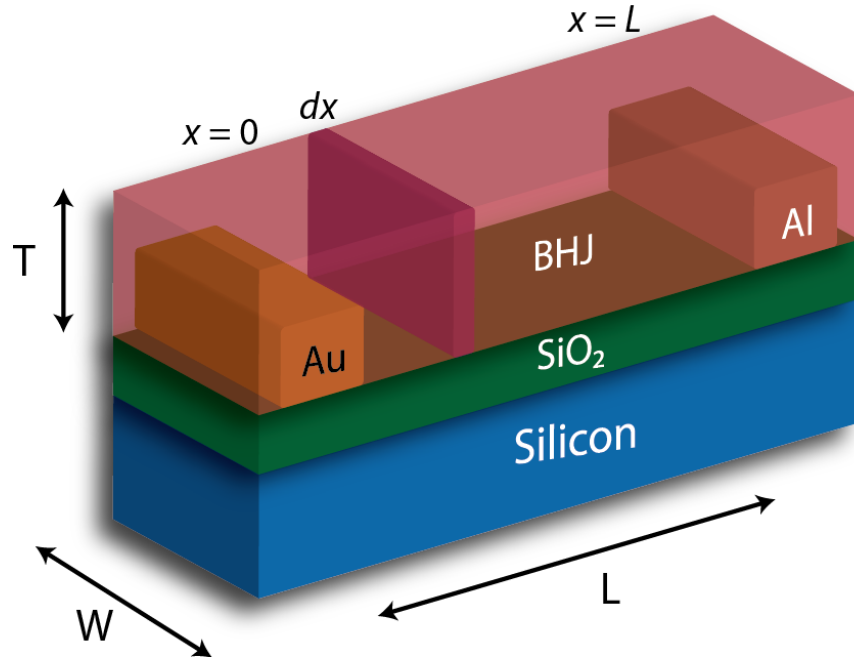


Figure 3.1: Schematic diagram of a lateral solar cell structure.

However, due to a recombination process (assumed here to be unimolecular), the charge density decays as the charges travel, so that the current eventually collected from this small volume becomes

$$dI = q G T W e^{-\frac{t}{\tau}} dx \quad (3.1)$$

where t is the time since the charge has been photogenerated, and τ is the lifetime of the charge carrier. The distance x traveled by the carriers is related to t through $dx = \mu E dt$, where μ is the mobility of the charge carrier and E is the electric field strength (the product μE gives the carrier velocity). Substitution then gives:

$$dI = q G T W \mu E e^{-\frac{t}{\tau}} dt \quad (3.2)$$

To find the total measured current, the contributions of the photogenerated charge throughout the entire length L of the device must be accounted for. As a result the total measured current will be:

$$I = \int_0^{\frac{L}{\mu E}} q G T W \mu E e^{-\frac{t}{\tau}} dt = q G T W \lambda \left(1 - e^{-\frac{L}{\lambda}}\right) \quad (3.3)$$

where the characteristic drift length λ is defined as $\lambda \equiv \mu E \tau$. Expressions for the current density, $J_{lat} = I/W T$, and the measured current normalized to absorption area, $I_{nor} = I/W L$, are shown in equations 3.4 and 3.5 respectively.

$$J_{lat} = q G \lambda \left(1 - e^{-\frac{L}{\lambda}}\right) \quad (3.4)$$

$$I_{nor} = \frac{q G T \lambda}{L} \left(1 - e^{-\frac{L}{\lambda}}\right) \quad (3.5)$$

In a system with bipolar transport, electrons and holes, in general, will possess different mobilities and mobility-lifetime products. The measured mobility-lifetime product will approximately be that of the faster carrier.

Figure 3.2 shows the current density collected at the electrodes as a function of device length for multiple electric fields. As the device length increases, the current density increases as a result of additional absorption area. Near $L = 3\lambda$, the current begins to saturate as a result of the device length increasing well beyond the characteristic drift length. As this happens, even though more mobile charge is being created, only the charge carriers created within about 3λ of the electrodes are collected. Carriers generated outside this zone will be lost to recombination processes. Figure 3.3 shows the current collected at the electrodes normalized to absorption area as a function of device length for multiple electric fields. In this case, the additional carriers generated due to the greater

absorption area in the larger devices have been factored out. As a result, the normalized current drops as a function of length because the charges have to travel well beyond their characteristic drift length and will be increasingly lost to recombination processes.

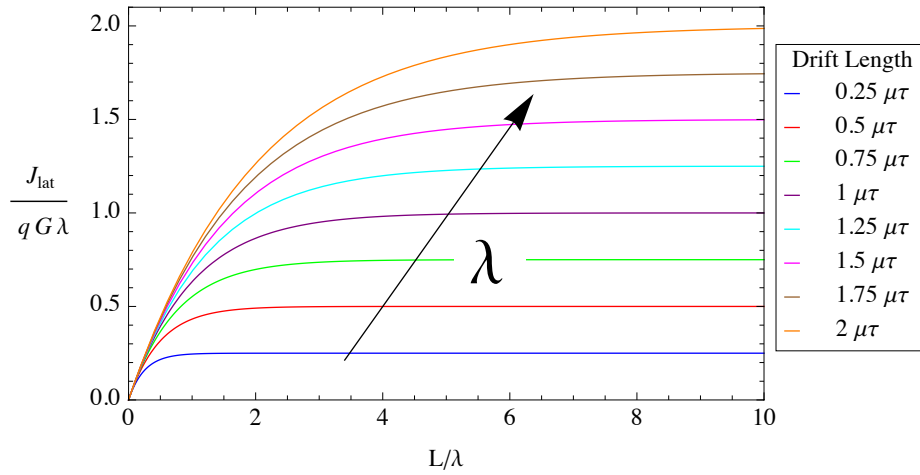


Figure 3.2: Theoretical plot of lateral current density vs. device length as derived in equation 3.4 for multiple electric fields.

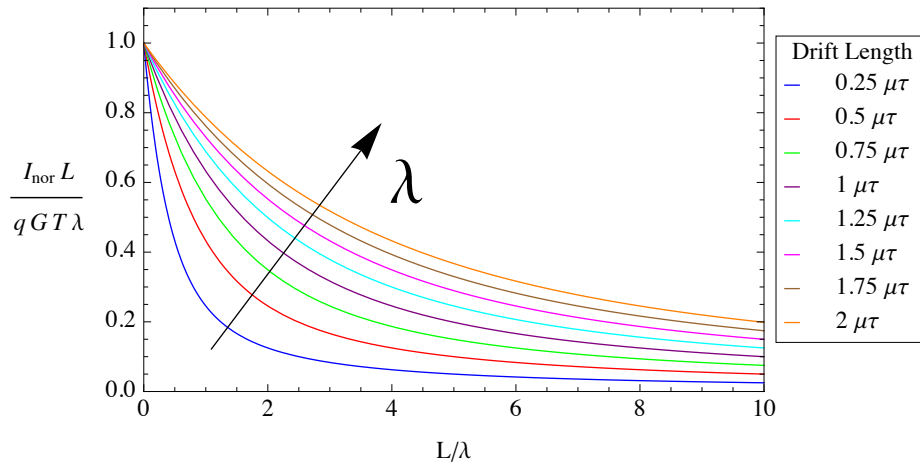


Figure 3.3: Theoretical plot of normalized current vs. device length as derived in equation 3.5 for multiple electric fields.

3.3 EXPERIMENTAL AND MEASUREMENTS

Lateral solar cell devices were fabricated starting on a p-type silicon substrate with 2000 Å of thermally grown silicon dioxide. The asymmetric electrodes were defined through two sets of photolithography: one for the aluminum (Al) cathodes and one for the gold (Au) anodes. These metals were chosen to efficiently suppress reverse bias injection within the lateral solar cell [66]. Each of these metals was thermally evaporated with a thickness of 500 Å. The device lengths ranged from 3 μm to 20 μm with a constant $W/L = 1000$. Before deposition of the BHJ layer, the substrate was dipped in a phosphoric acid solution to dissolve any aluminum oxide present on the surface of the Al electrodes. This was followed by a solvent clean to degrease the substrate, which consisted of acetone, methanol, and isopropyl alcohol. The BHJ absorber layer was deposited from a 20 mg/mL solution of P3HT:PCBM (1:1 by weight) dissolved in chloroform that was heated to 50° C for more than 12 hours. The BHJ was spun-cast on the prepared substrates at 1200 rpm for 60 seconds and this was followed by annealing at 145° C for 15 min. in a nitrogen atmosphere.

Measurements were performed in a *Desert Cryogenics* cryogenic probe station under vacuum better than 10^{-3} Torr at 333 K. Electrical measurements were performed using an *Agilent 4155C Semiconductor Parameter Analyzer*. Sample illumination was achieved using an *Oriel model 66912 and 66907* 150 W ozone-free xenon lamp. The optical spectrum was modified using an AM1.5g spectral filter and the light intensity was 100 mW/cm². Current vs. voltage measurements were performed on devices with lengths ranging from 3 μm to 20 μm under AM1.5g illumination. Experimental data for lateral current density vs. applied electric field and current normalized to absorption area vs. applied electric field are shown in Figure 3.4 and 3.5 respectively. For reverse bias electric field strengths less than 0.5×10^5 V/cm contact effects are present and for

reverse bias electric field strengths greater than 1.5×10^5 V/cm injection currents begin to influence the device characteristics.

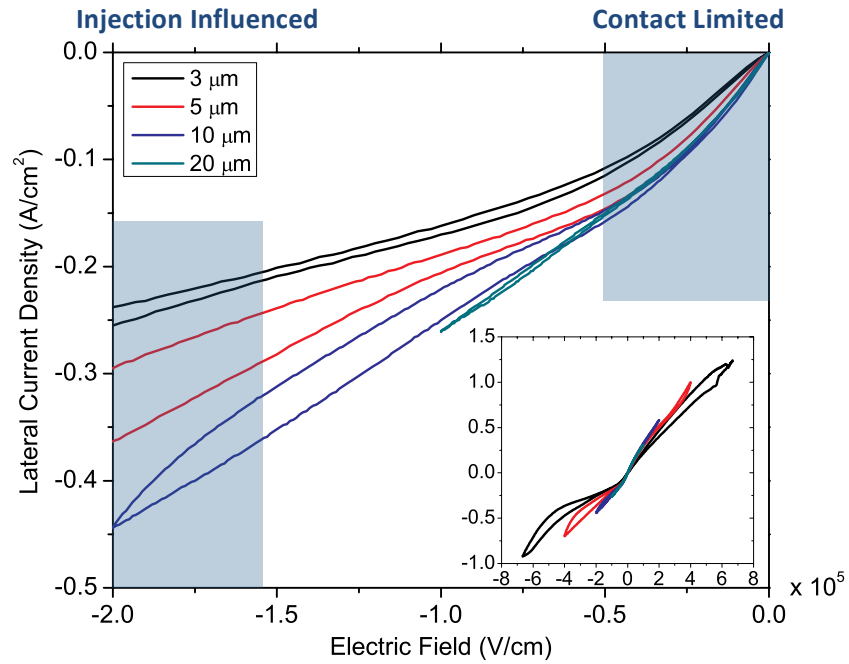


Figure 3.4: Experimental data for the lateral current density vs. electric field for lateral solar cells, in the reverse bias region where carrier injection was suppressed. The set of two curves represents a forward and backward voltage sweep. The inset shows the full range of collected data, which at higher fields have an increasing slope indicative of carrier injection.

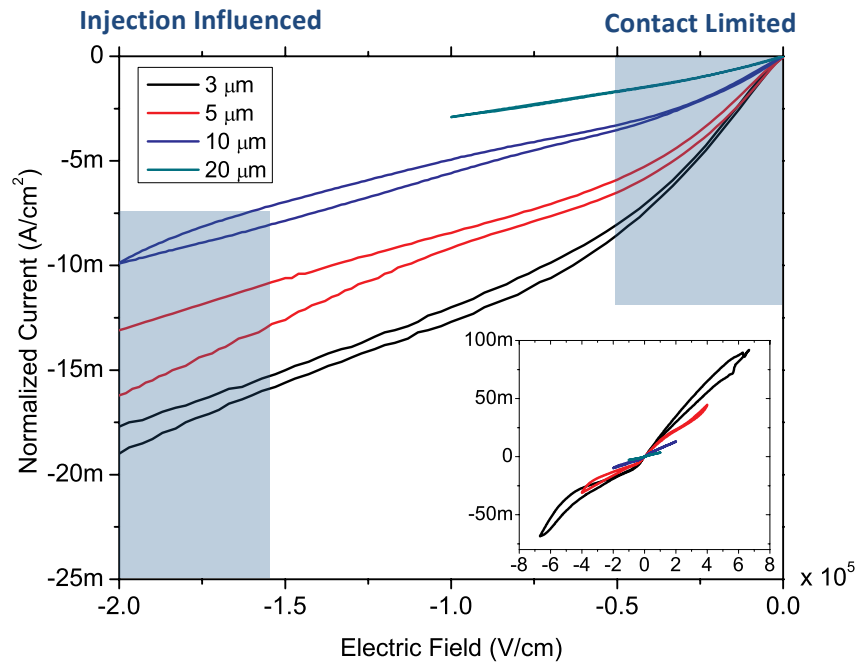


Figure 3.5: Experimental data for the normalized current vs. electric field for lateral solar cells, in the reverse bias region where carrier injection was suppressed. The set of two curves represents a forward and backward voltage sweep. The inset shows the full range of collected data, which at higher fields have an increasing slope indicative of carrier injection.

3.4 RESULTS AND DISCUSSION

To extract the mobility-lifetime product in lateral solar cells using equations 3.4 or 3.5, current vs. channel length data for a given applied electric field was used. To ensure that the currents being fitted were extraction currents as opposed to injection currents, data was extracted for values of the reverse bias electric field ranging from $0.25 \times 10^5 \text{ V/cm}$ to $2.0 \times 10^5 \text{ V/cm}$. In this region, the current response of the devices was relatively linear due to lack of carrier injection. At electric fields greater than $2.0 \times 10^5 \text{ V/cm}$ there was significant charge injection, as seen in the increasing slope of the current-voltage curve. This increased slope is also present in the device data under forward bias where carrier injection dominates.

Numerical fits to equations 3.4 and 3.5 were performed for lateral solar cells with device lengths ranging from 3 μm to 20 μm and at applied electric fields ranging from $0.25 \times 10^5 \text{ V/cm}$ to $2.0 \times 10^5 \text{ V/cm}$, which are shown in Figure 3.6 and Figure 3.7 respectively. These numerical fits result in carrier drift lengths of 2-5 μm regardless of whether equation 3.4 or equation 3.5 was used for fitting. The mobility-lifetime product, calculated from the drift length, was experimentally found to be $2 - 5 \times 10^{-9} \text{ cm}^2/\text{V}$ and is consistent with previous reports of mobility and/or carrier lifetime in measurements or simulations of BHJ solar cells based on P3HT:PCBM [56, 67, 68] or other organic BHJ systems [21, 69, 70]. The value of the mobility-lifetime product decreases slightly for increasing electric field. We believe that this is a result of the carrier lifetime decreasing. As more carriers are injected at larger electric fields, the recombination rate also increases, which in turn decreases the carrier's lifetime [56]. This is a result of the charge carrier populations becoming more balanced due to charge injection and the apparent dominant mechanism of recombination shifting from unimolecular to bimolecular. The mobility-lifetime product as a function of applied electric field extracted from equations 3.4 and 3.5 is shown in Figure 3.8.

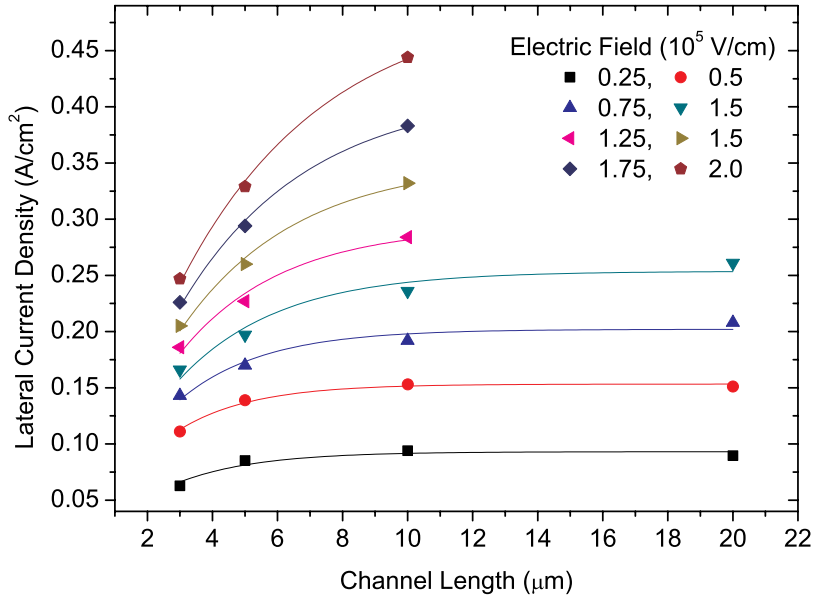


Figure 3.6: Lateral current density vs. device length various electric field values for P3HT:PCBM lateral solar cells. Both measured data (points) and numerical fits (lines) are shown.

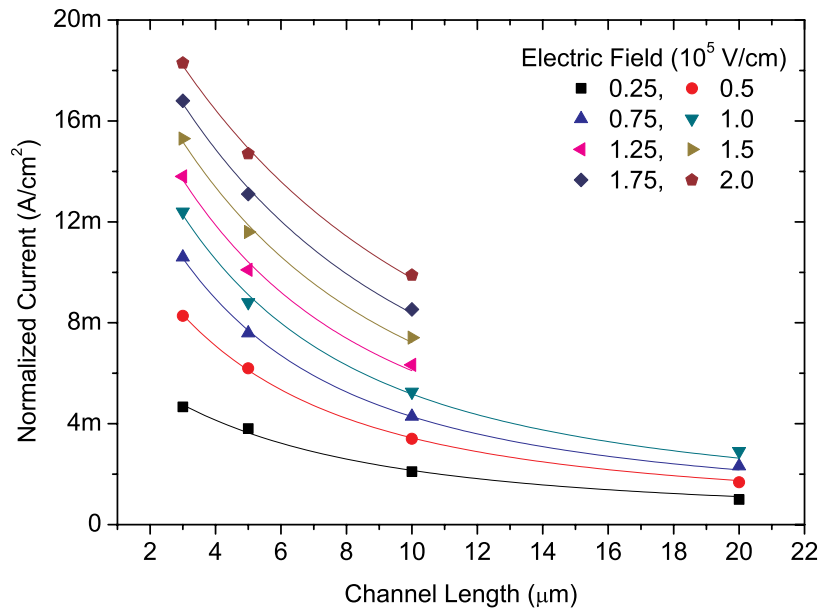


Figure 3.7: Normalized current vs. device length various electric field values for P3HT:PCBM lateral solar cells. Both measured data (points) and numerical fits (lines) are shown.

In addition to the mobility-lifetime product, fitting to equations 3.4 and 3.5 provided an independent estimate of the charge carrier generation rate, G . This number is the volume concentration of charge carriers generated per unit time as a result of photogenerated excitons disassociating. The generation rates calculated from equations 3.4 and 3.5 are in the range $4 - 7 \times 10^{21} \text{cm}^{-3} \text{s}^{-1}$ which is consistent with previous reports [71]. As the applied electric field increases, the generation rate also increases which could be a result of the increased electric field assisting the ionization of charge transfer excitons [72-74]. Present within the measurement of the generation rate will be any injection currents. These currents arise since to the asymmetric electrodes do not perfectly block the injection of charge carriers at with increases in applied electric field. In addition, the recombination mechanism shifts from unimolecular to bimolecular with increased applied electric field which should affect the generation rate. The shifts in generation mechanism will be discussed in Chapter 4. The generation rate as a function of applied electric field extracted from equations 3.4 and 3.5 is also shown in Figure 3.8. We note that the approach we have discussed above is one of the few methods to calculate the carrier generation rate, which is a parameter of importance in characterizing new materials technologies.

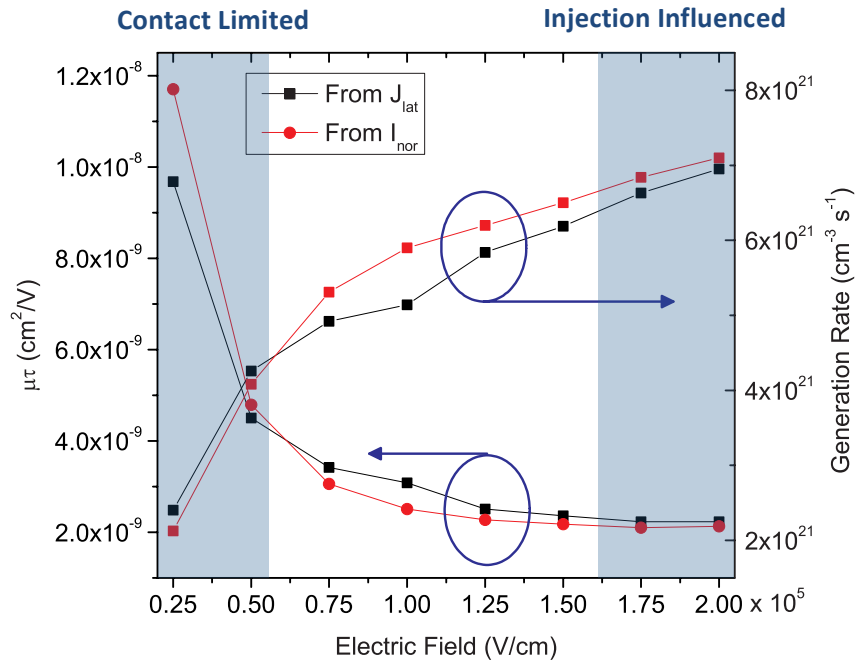


Figure 3.8: The mobility-lifetime product and the generation rate vs. applied electric field extracted from the lateral current density and the normalized current.

The mobility-lifetime product that we calculate will apply to the faster of the two carrier types. This faster carrier is present at comparably lower steady-state carrier concentrations and functions as the “minority carrier”. This also justifies our assumption of unimolecular recombination at low electric fields.

3.5 SUMMARY

We have reported on Hecht’s equation, which was rederived for lateral device structures both in terms of current density and normalized current as a function of device length. From this derivation, experimental data from lateral BHJ solar cells was fitted to these equations and has resulted in mobility-lifetime products of $2 - 5 \times 10^{-9} \text{ cm}^2/\text{V}$ and charge carrier generation rates of $4 - 7 \times 10^{21} \text{ cm}^{-3} \text{ s}^{-1}$. Drift lengths for applied electric fields on the order of 10^5 V/cm were found to be a few microns which are

comparable to the device lengths. Such drift lengths are markedly longer than the typical thickness of organic BHJ solar cells (active layer ~ 100 nm), and suggest that carrier recombination may not be a performance-limiting factor in P3HT:PCBM cells. The mobility-lifetime product decreases with increasing electric field, which is probably a result of charge carrier injection and a shift in recombination mechanisms from unimolecular to bimolecular. In addition, the charge carrier generation rate increased with increasing electric field, most likely due to the electric field assisted ionization of charge transfer excitons at the donor/acceptor interface as well as a shift in recombination mechanism.

Chapter 4: Mechanisms of Recombination

4.1 INTRODUCTION

Fundamental to understanding the operation of OPV cells is a thorough study of the recombination mechanisms present in these devices. By studying these processes researchers can better understand how to make high quality materials and device structures. In order to calculate the recombination rate, we begin with the continuity equation for holes and electrons shown in equations 4.1 and 4.2 respectively, where q is the amount of charge, p and n are the hole and electron concentrations respectively, J is the current density, G is the generation rate, and U is the recombination rate.

$$\frac{\partial p}{\partial t} = -\frac{1}{q} \frac{\partial J_p}{\partial x} + G_p - U_p \quad (4.1)$$

$$\frac{\partial n}{\partial t} = \frac{1}{q} \frac{\partial J_n}{\partial x} + G_n - U_n \quad (4.2)$$

Since under steady state illumination $\frac{\partial p}{\partial t} = 0$ and $\frac{\partial n}{\partial t} = 0$, the recombination rate is simply the generation rate minus the number of charge carriers that exit the device (after accounting for the sign of the charge carriers).

$$U_p = G_p - \frac{1}{q} \frac{\partial J_p}{\partial x} \quad (4.3)$$

$$U_n = G_n + \frac{1}{q} \frac{\partial J_n}{\partial x} \quad (4.4)$$

The generation and recombination rates of electrons and holes should be the equal, $G = G_p = G_n$ and $U = U_p = U_n$, and by using Ramo's Theorem for electrical current induced by electron motion [75], equations 4.3 and 4.4 reduce to a single expression for the recombination rate in terms of measured parameters and the geometry of the device,

$$U = G \pm \frac{1}{q} \frac{I}{WLT} \quad (4.5)$$

where I is the measured photocurrent, W is the device width, L is the device length, and T is the thickness of the BHJ layer. This equation is the same as equation 2.4 initially presented in Chapter 2.

In order to determine the mechanism of recombination, the carrier concentration dependence of the recombination rate must be determined. *Mihailetschi et al.* have stated that the generation rate is proportional to the light intensity [71], $G \propto P_{light}$. In addition, the excess carrier concentrations of both holes and electrons will also be proportional to the light intensity. Therefore, for a purely unimolecular recombination process where electrons are the minority carrier, $U \propto \Delta n \propto P_{light}$, or for a purely bimolecular recombination process, $U \propto \Delta p \Delta n \propto P_{light}^2$, where Δp and Δn are the excess hole and electron concentrations respectively. A more general form for how the recombination rate is affected by changes in light intensity is shown in equation 4.6.

$$U \propto P_{light}^{\nu} \quad (4.6)$$

For a purely unimolecular recombination process, $\nu = 1$, and for a purely bimolecular recombination process, $\nu = 2$. Values of ν that are between 1 and 2 indicate that the recombination process is not strictly unimolecular or bimolecular in nature. Unimolecular recombination processes should determine when there is a steady-state charge accumulation layer present due to an asymmetry in the electron and hole mobilities. Bimolecular recombination processes should prevail when the electron and hole carrier concentrations are roughly balanced which means the electron and hole mobilities are approximately equal. Although most researchers publish either strictly unimolecular [60] or bimolecular recombination rates (bimolecular for OPV systems) [8,

21, 27-29, 33, 44, 45, 57, 70, 76], it is likely that an intermediate mechanism or a transition between recombination mechanisms is actually what occurs [77].

4.2 EXPERIMENTAL

Lateral solar cell devices were fabricated starting on a p-type silicon substrate with 2000 Å of thermally grown silicon dioxide. The asymmetric electrodes were defined through two sets of photolithography: one for the aluminum (Al) cathodes and one for the gold (Au) anodes. These metals were chosen to reduce the extent of reverse bias injection within the lateral solar cell [66]. Each of these metals was thermally evaporated with a thickness of 500 Å. The device lengths ranged from 3 µm to 20 µm with a constant $W/L = 1000$. Before deposition of the BHJ layer, the substrate was dipped in a phosphoric acid solution to dissolve any aluminum oxide present on the surface of the Al electrodes. This was followed by a solvent clean to degrease the substrate, which consisted of acetone, methanol, and isopropyl alcohol. The BHJ absorber layer was deposited from a 20 mg/mL solution of P3HT:PCBM (1:1 by weight) dissolved in chloroform that was heated to 50° C for more than 12 hours. The BHJ was spun-cast on the prepared substrates at 1200 rpm for 60 seconds and this was followed by annealing at 145° C for 15 min. in a nitrogen atmosphere. This device structure is the same structure used in Chapter 3.

Measurements were performed in a *Desert Cryogenics* cryogenic probe station under vacuum better than 10^{-3} Torr. Electrical measurements were performed using an *Agilent 4155C Semiconductor Parameter Analyzer*. Solar illumination was provided using an *Oriel model 66912 and 66907* 150 W ozone-free xenon lamp. The optical spectrum was modified using an AM1.5g spectral filter. The light intensity was

modulated using a set of neutral density filters to achieve the desired illumination intensity. Monochromatic illumination was provided using an *Optotronics VA-I-300-532* 532 nm diode pumped solid-state laser system. The light intensity was modulated both at the power supply and through the use of neutral density filters to achieve the desired intensity. Current vs. voltage measurements were performed on devices with lengths ranging from 3 μm to 20 μm under AM1.5g and 532 nm illumination at multiple illumination intensities.

4.3 RESULTS

Current vs. applied electric field data is shown in Figure 4.1 for lateral solar cells with lengths ranging from 3 μm to 20 μm under AM1.5g illumination at 100 mW/cm^2 . As expected, the current at a given electric field increases as the device length increases since $W/L = 1000$ and the absorption area increases with device length for all of the measured devices. Similar results are shown under 532 nm illumination at 100 mW/cm^2 in Figure 4.2.

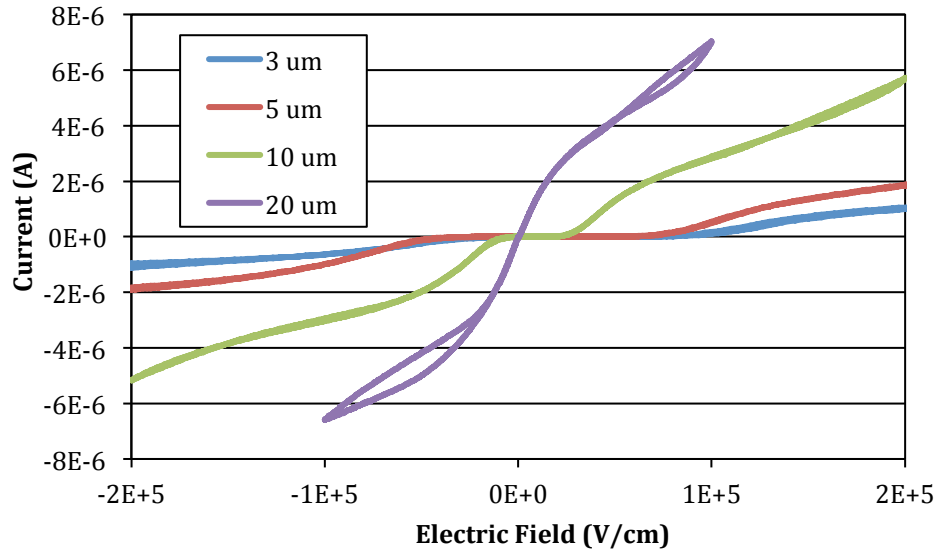


Figure 4.1: Current vs. applied electric field data for lateral solar cells with lengths ranging from 3 μm to 20 μm under AM1.5g illumination at 100 mW/cm^2 .

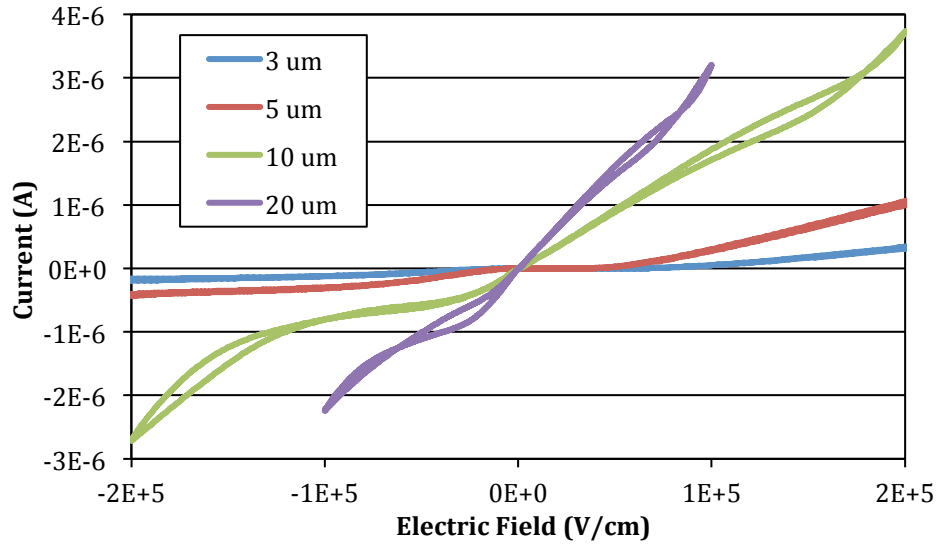


Figure 4.2: Current vs. applied electric field data for lateral solar cells with lengths ranging from 3 μm to 20 μm under 532 nm illumination at 100 mW/cm^2 .

In addition, current vs. applied electric field data for a 5 μm lateral solar cell under AM1.5g illumination with illumination intensities ranging from 6 mW/cm^2 to 100

mW/cm² is shown in Figure 4.3. The same device is also shown under 532 nm illumination with illumination intensities ranging from 5 mW/cm² to 500 mW/cm² and is shown in Figure 4.4. As expected, the current increases for increasing illumination intensity under both illumination spectra. The 3 μm, 10 μm, and 20 μm length devices exhibit similar characteristics to the 5 μm device. The current exiting the lateral solar cells is greater under AM1.5g illumination as compared to 532 nm illumination at the same intensity which is a result of P3HT:PCBM being able to efficiently absorb additional wavelengths of light present in the AM1.5g spectrum. P3HT can generate carriers from green and red light while at the same time PCBM can generate carriers from UV light [71] which increases the current produced per unit absorption area. In addition, contact effects are present at electric field strengths less than 0.5×10^5 V/cm under forward and reverse bias.

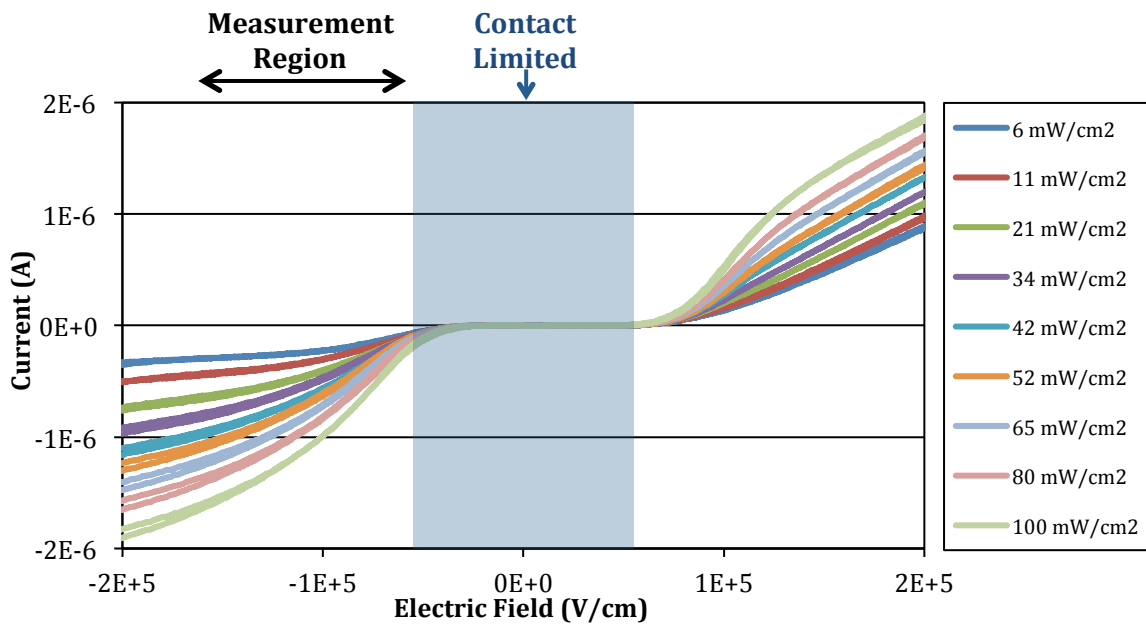


Figure 4.3: Current vs. applied electric field data for a 5 μm lateral solar cell with AM1.5g illumination intensities ranging from 6 mW/cm² to 100 mW/cm².

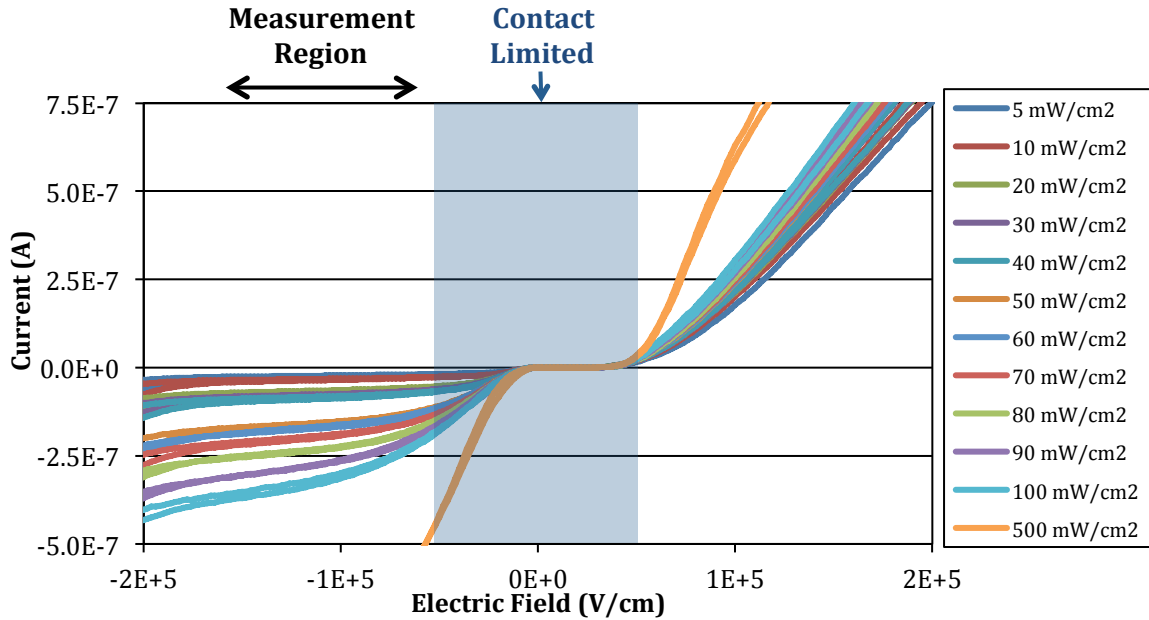


Figure 4.4: Current vs. applied electric field data for a 5 μm lateral solar cell with 532 nm illumination intensities ranging from 5 mW/cm^2 to 500 mW/cm^2 .

4.4 MOBILITY-LIFETIME PRODUCT & GENERATION RATE

The mobility-lifetime product and generation rate in lateral solar cell devices was calculated by rederiving Hecht's equation for charge collection. This derivation was discussed in detail in Chapter 3. This analysis, resulting in equations 3.4 and 3.5, has been applied to lateral solar cell devices while varying the light intensity. Figure 4.5 shows the mobility-lifetime product as a function of AM1.5g light intensity for reverse bias applied electric field values of $0.75 - 1.5 \times 10^5 \text{ V}/\text{cm}$. The mobility-lifetime product calculated for these devices is roughly between 10^{-9} and $10^{-8} \text{ cm}^2/\text{V}$. As the light intensity increases, the mobility-lifetime product decreases which is likely the result of the carrier lifetime decreasing. This occurs because for higher illumination intensities, there are greater carrier populations. This results in more opportunities for carrier recombination and as a result, reduces the lifetime of charge carriers. This is consistent

with mobility-lifetime product data as a function of applied electric field discussed in Chapter 3 and presented in Figure 3.8. In addition, data for light intensities that are less than about 30 mW/cm^2 are influenced by dark current.

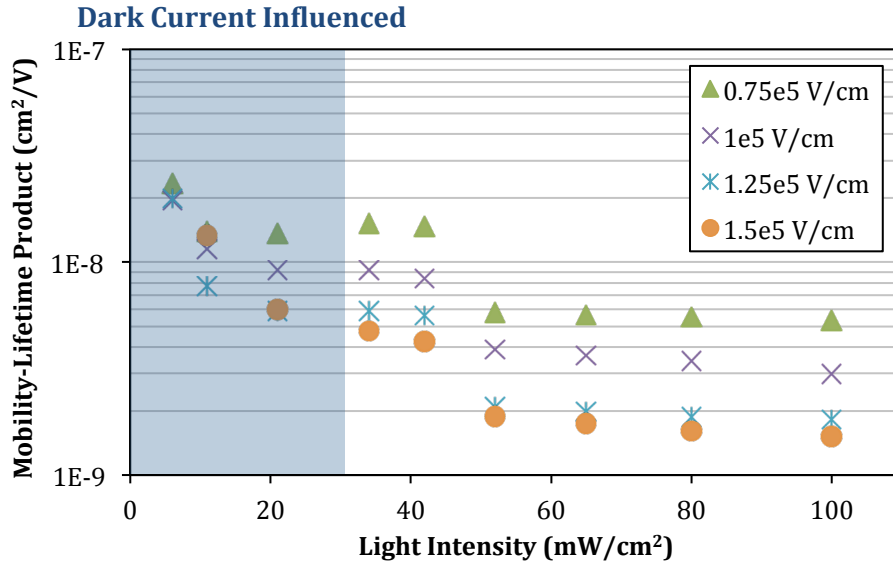


Figure 4.5: Mobility-lifetime product vs. light intensity for lateral solar cell devices under AM1.5g illumination with intensities ranging from 6 mW/cm^2 to 100 mW/cm^2 .

Similar results are for shown for the mobility-lifetime product vs. 532 nm illumination intensity in Figure 4.6. Like under AM1.5g illumination, the mobility-lifetime product also decreases as both the light intensity and the reverse bias electric field increases.

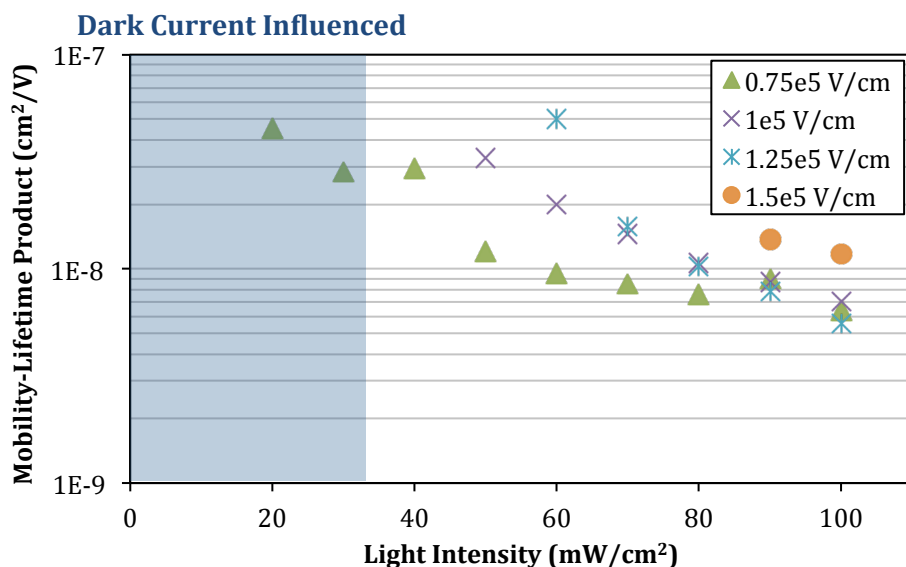


Figure 4.6: Mobility-lifetime product vs. light intensity for lateral solar cell devices under 532 nm illumination with intensities ranging from 5 mW/cm² to 100 mW/cm².

In addition to the mobility-lifetime product, the generation rate as a function of light intensity has also been calculated for these lateral solar cell devices. Figure 4.7 shows the generation rate as a function of AM1.5g light intensity for reverse bias electric field values of 0.75 – 1.5 x 10⁵ V/cm. The generation rate calculated for these devices is roughly between 10²⁰ and 10²² cm⁻³ s⁻¹. The generation rate increases by about an order of magnitude with increasing light intensity. This behavior is expected as the saturation of light induced charge carrier generation is not likely to occur at light intensities on the order of 1 sun. Following the discussion in Chapter 3, the generation rate also increases as the applied electric field increases.

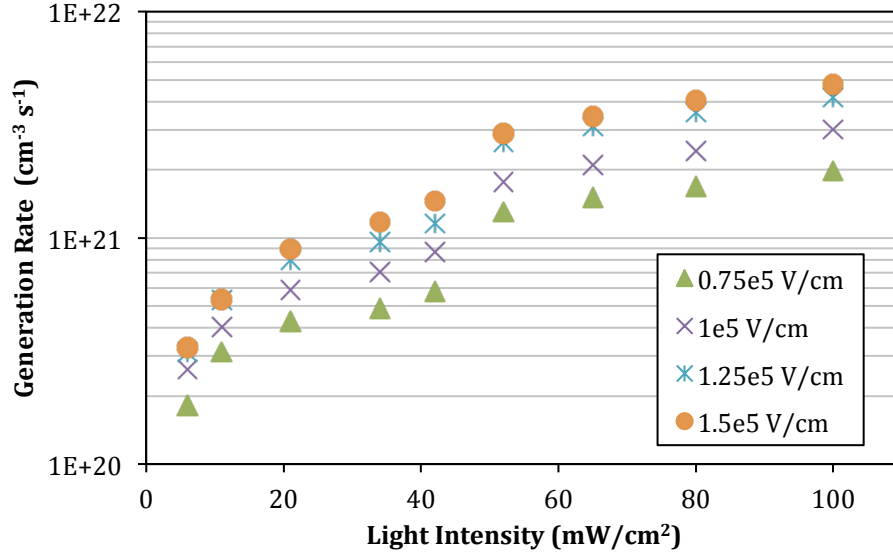


Figure 4.7: Generation rate vs. light intensity for lateral solar cell devices under AM1.5g illumination for reverse bias electric field strengths on the range 0.75 - 1.5 x 10⁵ cm⁻³ s⁻¹.

Similar results are for shown for the generation rate vs. 532 nm light intensity in Figure 4.8. Like under AM1.5g illumination, the generation rate increases as both the light intensity and the applied electric field increase.

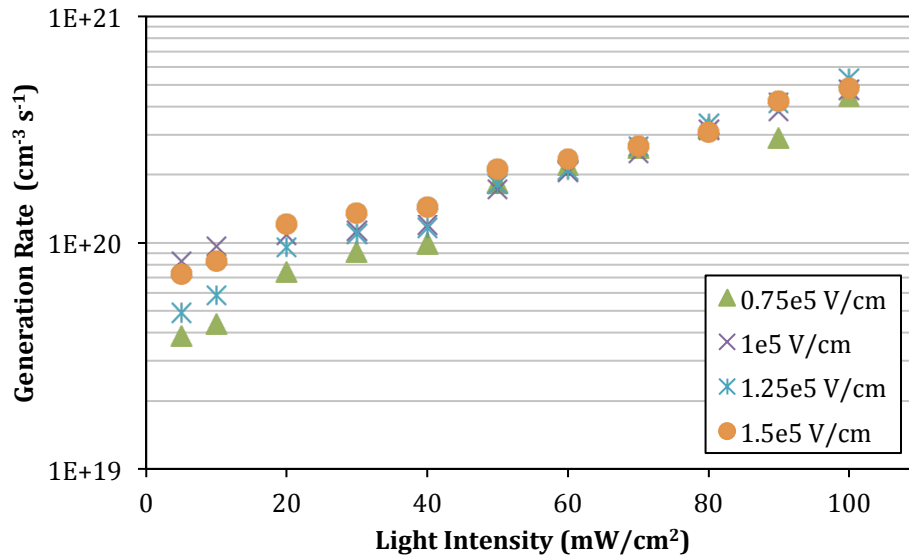


Figure 4.8: Generation rate vs. light intensity for lateral solar cell devices under 532 nm illumination for reverse bias electric field strengths on the range $0.75 - 1.5 \times 10^5 \text{ cm}^{-3} \text{ s}^{-1}$.

Figure 4.9 shows the mobility-lifetime product under AM1.5g and 532 nm illumination with a reverse bias electric field of $0.75 \times 10^5 \text{ V/cm}$. Figure 4.10 shows the generation rate under AM1.5g and 532 nm illumination at with a reverse bias electric field of $0.75 \times 10^5 \text{ V/cm}$.

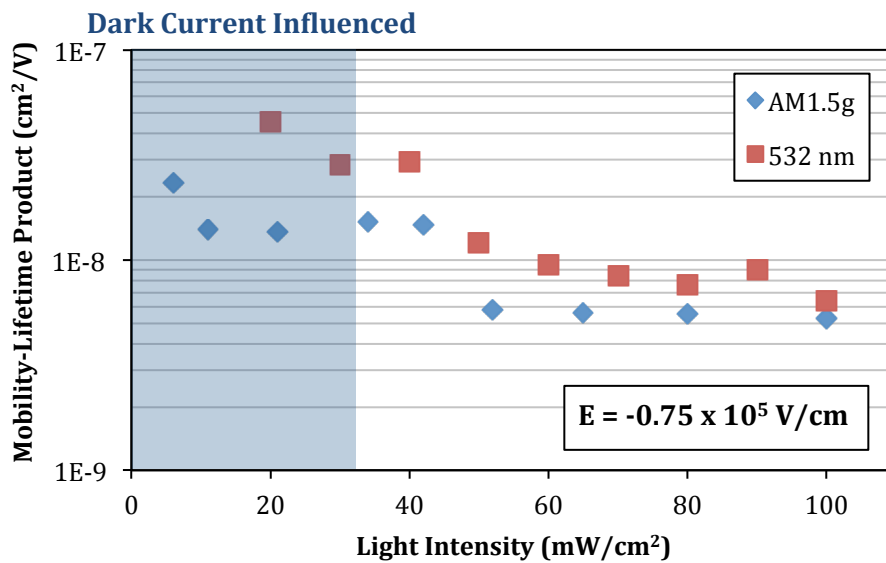


Figure 4.9: Comparison of the mobility-lifetime product vs. illumination intensity for lateral solar cell devices under AM1.5g and 532 nm illumination. These devices have a reverse bias electric field of $0.75 \times 10^5 \text{ V/cm}$.

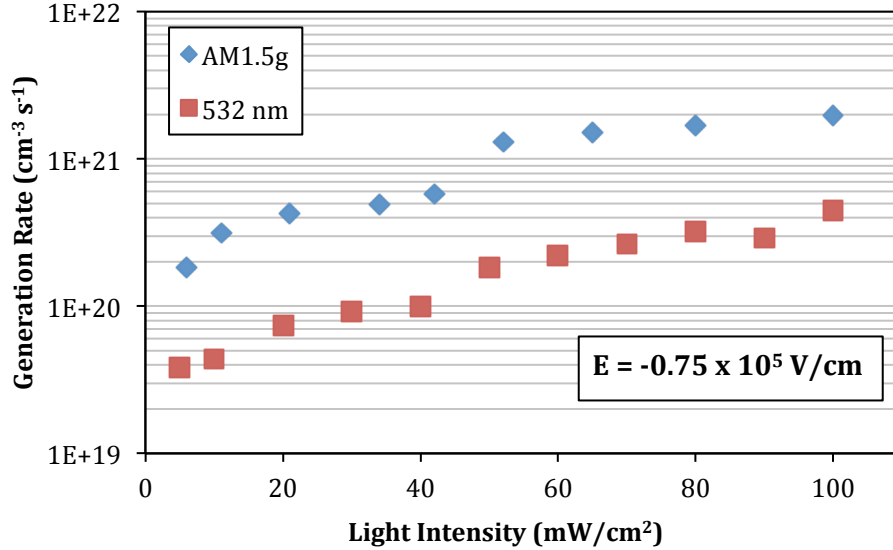


Figure 4.10: Comparison of the generation rate vs. illumination intensity for lateral solar cell devices under AM1.5g and 532 nm illumination. These devices have a reverse bias electric field of 0.75×10^5 V/cm.

The mobility-lifetime product under AM1.5g illumination is reduced as compared to 532 nm illumination. This is correlated to the increased generation rate present under AM1.5g illumination as compared to 532 nm illumination. Just as an increased light intensity creates more photogenerated charge carriers, differences in absorption spectrum result in changes in the carrier population. The reduction in carrier lifetime as a result of higher carrier populations occurs whether the differences in carrier concentration arise as a result of changes in illumination intensity or changes in illumination spectrum.

4.5 RECOMBINATION MECHANISMS

In addition to the mobility-lifetime product, DC photocurrent measurements can be used to measure the recombination rate in lateral solar cell devices. Using equation 4.5 the recombination rate can be plotted as a function of electric field where the

generation rate used is extracted from the mobility-lifetime product/generation rate calculation described in Chapter 3 and Chapter 4.4. This is shown for lateral solar cell devices with lengths ranging from 3 μm to 20 μm under AM1.5g illumination at 100 mW/cm^2 in Figure 4.11. As the electric field increases, the recombination rate decreases because the applied electric field sweeps more photogenerated carriers out of the device. As expected, the recombination rate increases with increasing device length as an increasing number of carriers cannot exit the device before recombining. The asymmetry in the recombination data is due to the asymmetric electrodes used in the device structure. In reverse bias, the electrodes block (to some extent) the injection of the opposite carrier type and should only extract carriers (until a sufficient electric field strength is reached). In forward bias, carriers will be injected even at small electric fields so it is important to the study these devices under reverse bias while studying recombination mechanisms.

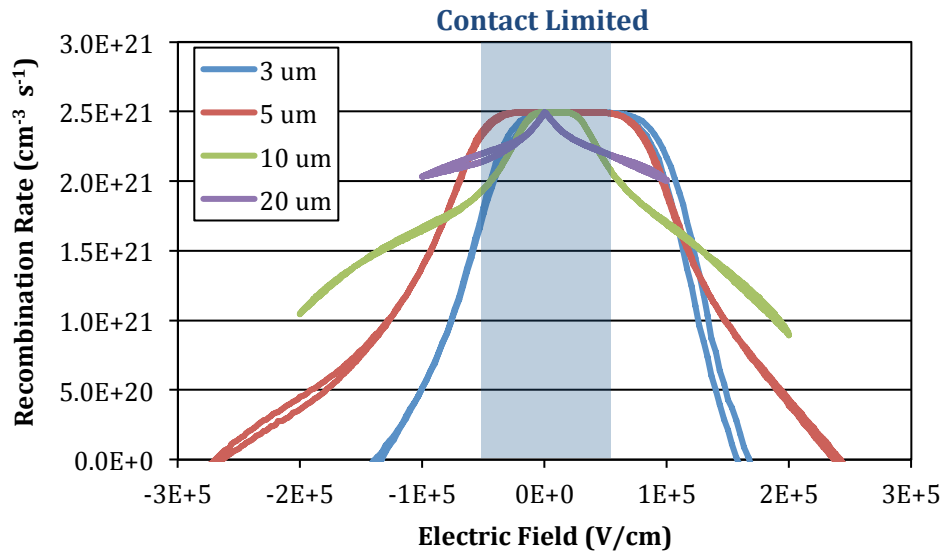


Figure 4.11: Recombination rate vs. applied electric field for lateral solar cell devices with lengths ranging from 3 μm to 20 μm under AM1.5g illumination at 100 mW/cm^2 .

Similar data is shown for lateral solar cell devices under 532 nm illumination at 500 mW/cm² in Figure 4.12. Recombination data is shown under 532 nm illumination at 500 mW/cm² because the generation rate was calculated to be $1.6 \times 10^{21} \text{ cm}^{-3} \text{ s}^{-1}$. The generation rate under AM1.5g illumination at 100 mW/cm² was calculated to be $2.5 \times 10^{21} \text{ cm}^{-3} \text{ s}^{-1}$. These two data sets are the most comparable in terms of generation rate in the vicinity of 1 sun illumination.

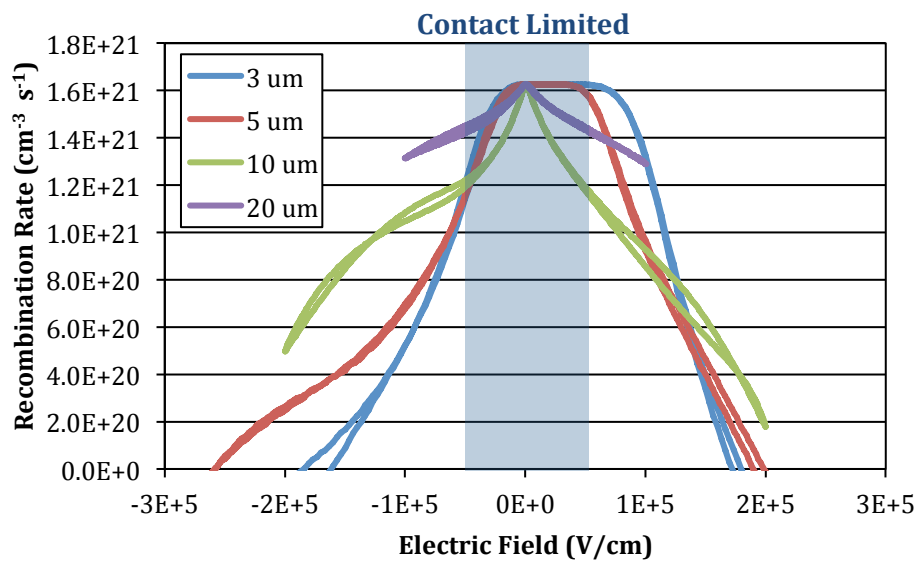


Figure 4.12: Recombination rate vs. applied electric field for lateral solar cell devices with lengths ranging from 3 μm to 20 μm under 532 nm illumination at 500 mW/cm².

To analyze the differences between AM1.5g illumination and 532 nm illumination on the electric field dependence of the recombination rate, both sets of recombination data were normalized to their generation rate and plotted together. In most cases, 532 nm illumination shows lower normalized recombination than AM1.5g illumination. In addition, there is less of an asymmetry in the recombination rate as a function of electric field under 532 nm illumination as compared to AM1.5g illumination.

The recombination rate normalized to the generation rate as a function of applied electric field is shown in Figure 4.13.

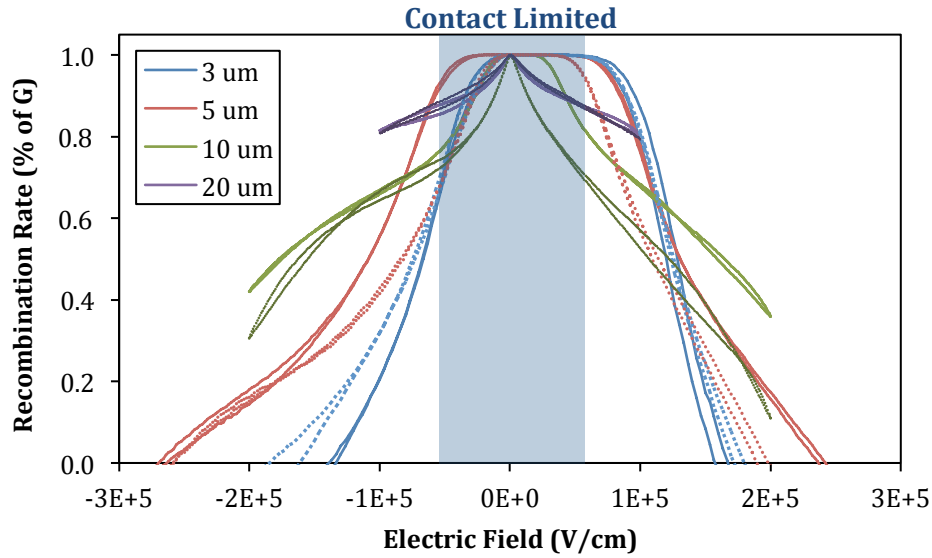


Figure 4.13: Normalized recombination rate vs. applied electric field for lateral solar cell devices with lengths ranging from 3 μm to 20 μm under AM1.5g illumination at 100 mW/cm^2 (solid lines) and 532 nm illumination at 500 mW/cm^2 (dotted lines).

In order to determine the mechanism of recombination, the recombination rate needs to be analyzed in terms of the illumination intensity, which is proportional to the carrier concentration (equation 4.6). Figure 4.14 shows the recombination rate vs. light intensity for lateral solar cell devices ranging from 3 μm to 20 μm under AM1.5g illumination at a reverse bias electric field of $0.75 \times 10^5 \text{ V}/\text{cm}$. As expected, the recombination rate increases with increasing illumination intensity. The recombination exponent is in the range 1.0 to 1.2, which indicates the recombination mechanism is unimolecular in nature. This implies the recombination is dependent on a single carrier type, the “quasi minority carrier”. This carrier is the faster carrier in these lateral solar

cell devices. The slower, “quasi majority carrier”, accumulates within the BHJ and becomes an “infinite sea” of carriers, much like majority carriers in traditional doped semiconductors. For the case of purely unimolecular recombination, the recombination rate is based on the excess carrier concentration of minority carriers and their lifetime, $U = \frac{\Delta n}{\tau_e}$ in the case where electrons are the faster carrier (quasi minority carrier) or $U = \frac{\Delta p}{\tau_h}$ in the case where holes are the faster carrier.

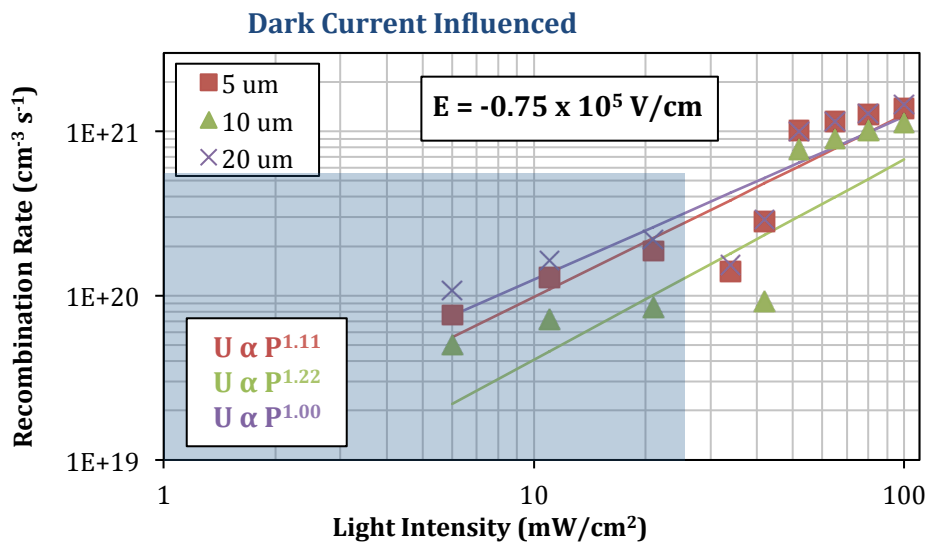


Figure 4.14: Recombination rate vs. light intensity for lateral solar cell devices with lengths ranging from 5 μm to 20 μm under AM1.5g illumination at a reverse bias electric field of $0.75 \times 10^5 \text{ V/cm}$.

Figure 4.15 shows similar recombination rate vs. light intensity data under 532 nm illumination. Like recombination data shown for AM1.5g illumination, the recombination mechanism under 532 nm illumination is also primarily unimolecular indicating there is an accumulation layer of the slower carrier (quasi majority carrier). The exponent value is in the range of 1.1 to 1.3 which is slightly higher than for AM1.5g illumination.

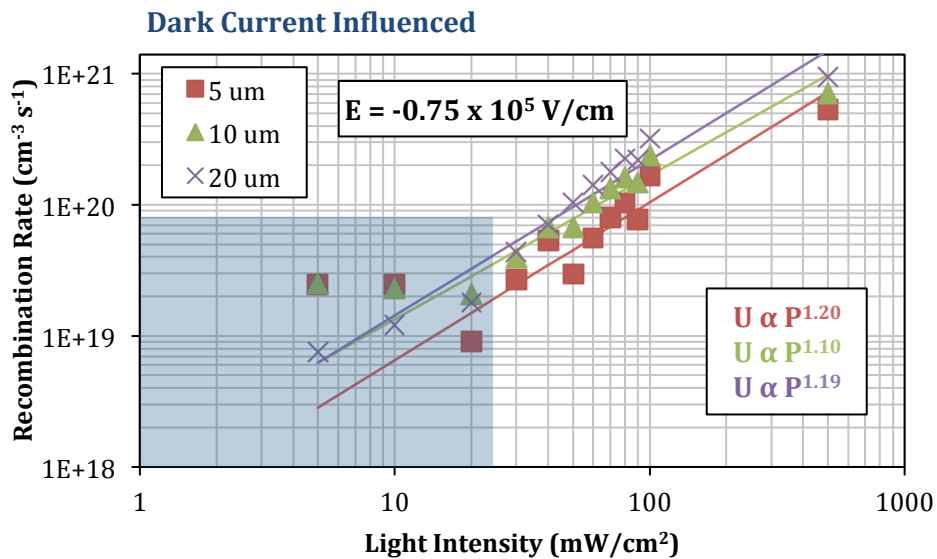


Figure 4.15: Recombination rate vs. light intensity for lateral solar cell devices with lengths ranging from 5 μm to 20 μm under 532 nm illumination at a reverse bias electric field of $0.75 \times 10^5 \text{ V/cm}$.

In order to examine the effects of device length and electric field on the recombination mechanisms, the recombination exponent needs to be examined as a function of reverse bias electric field for both AM1.5g illumination and 532 nm illumination. For AM1.5g illumination, the recombination exponent increases with reverse bias electric field until a specific point, about $1.5 \times 10^5 \text{ V/cm}$ depending on the specific device. The increase in recombination exponent is the result of increased carrier injection. This can be seen as the generation rate increases as a function of applied electric field as shown in Figure 3.8. This carrier injection favors the faster carrier (quasi minority carrier) which has a much lower concentration than the slower carrier (quasi majority carrier). As a result, the imbalance in carrier populations will tend to become equalized due to the injection of quasi minority carriers. As the carrier concentrations become more balanced, the recombination exponent should increase, approaching 2.0,

indicating a bimolecular recombination process. Unlike unimolecular recombination, the bimolecular recombination rate is dependent on both carrier types and has the form $U = B \Delta n \Delta p$. The recombination exponent vs. reverse bias electric field is shown in Figure 4.16 for lateral solar cell devices ranging in length from 5 μm to 20 μm under AM1.5g illumination with intensities ranging from 6 mW/cm^2 to 100 mW/cm^2 .

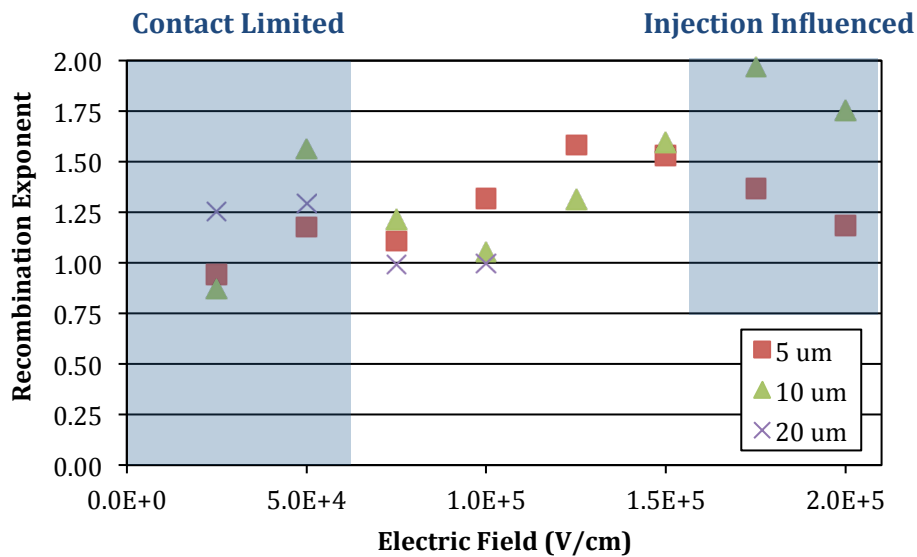


Figure 4.16: Recombination exponent vs. reverse bias electric field for lateral solar cell devices with lengths ranging from 5 μm to 20 μm under AM1.5g illumination with intensities ranging from 6 mW/cm^2 to 100 mW/cm^2 .

Under 532 nm illumination, similar characteristics are present in the recombination mechanisms as compared to AM1.5g illumination. At low electric field strengths, the recombination mechanism is unimolecular indicating the presence of a charge accumulation layer. As the electric field increases, there is a much clearer transition to bimolecular recombination as compared to AM1.5g illumination. Figure 4.17 shows the recombination exponent vs. reverse bias electric field for lateral solar

cells ranging from 5 μm to 20 μm under 532 nm illumination with intensities ranging from 5 mW/cm^2 to 500 mW/cm^2 .

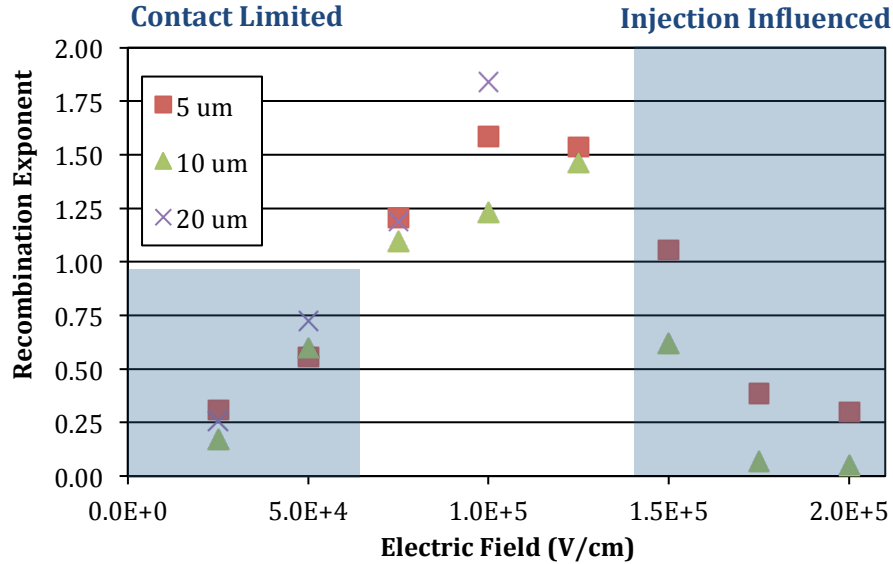


Figure 4.17: Recombination exponent vs. reverse bias electric field for lateral solar cell devices with lengths ranging from 5 μm to 20 μm under 532 nm illumination with intensities ranging from 5 mW/cm^2 to 500 mW/cm^2 .

At low and high electric field strengths, the recombination exponent is less than 1.0. Initially, this may seem unphysical but the explanation can be traced back to assumptions made in Chapter 4.1. Previously it was stated that the recombination rate is proportional to the excess carrier concentration which is proportional to the incident light intensity ($U \propto \Delta n \propto P_{light}$ or $U \propto \Delta p \Delta n \propto P_{light}^2$), but our measurements are of recombination rate vs. light intensity, not recombination rate vs. excess carrier concentration. By fitting this data to equation 4.6, the recombination exponent ν is found. Since the recombination exponent is found as a function of light intensity, not excess carrier concentration, it tells us how the light intensity affects the recombination rate. For $\nu = 1$, the recombination rate is dependent on one carrier type and only that

carrier type is modulated by changes in the light intensity. For $\nu = 2$, the recombination rate is dependent on both carrier types and both are modulated by changes in the light intensity. By extension, for $\nu = 0$, the recombination rate is not modulated by changes in light intensity.

At low electric field strengths the recombination exponent is less than 1.0 because there is not sufficient carrier velocity to transport the carriers out of the device, so the vast majority of the charge carriers recombine. Since the drift length of these carriers, which is a function of electric field, is much smaller than the device length, modulating the carrier concentration by changing the illumination intensity has little effect on the recombination rate since virtually all carriers recombine before exiting that device. At high electric field strengths the recombination exponent also begins to drop. At these electric field strengths, the majority of the current flowing in these devices is not due to photogenerated charge carriers. The measured current is the result of injected charge carriers. Since a lower value for the recombination exponent means that light intensity plays a diminished role in recombination, and measured current due to the injection of charge carriers should not be modulated by changes in the light intensity, it follows logically that the injected current dominates the current flow in the device at high electric fields. If this were not the case and the majority of the current flowing in the device was a result of photogenerated charge carriers, changes in light intensity would produce a much larger change in the carrier concentration and thus the recombination rate. This shows that in the case of high electric fields where charge injection plays a significant role in the device characteristics, the assumption that the excess carrier concentration is proportional to the light intensity becomes invalid.

4.6 CONCLUSION

Measurements of the DC current flowing in BHJ lateral solar cell devices have demonstrated the ability to measure recombination rates and mechanisms of recombination in these devices. By measuring the current vs. applied electric field for devices with lengths ranging from 3 μm to 20 μm , under AM1.5g and 532 nm illumination at multiple intensities, we have calculated the mobility-lifetime product, the charge generation rate, and the recombination rate as a function of electric field. In addition, we have determined the recombination mechanisms and their electric field dependence for lateral solar cells of P3HT:PCBM. For low reverse bias electric field strengths, unimolecular recombination prevails due to a charge imbalance which creates an accumulation layer of the slower moving quasi majority carriers. As the reverse bias electric field increases, more charge carriers are injected leading to greater balance in the charge carrier populations. This shifts the recombination mechanism to favor a bimolecular process since quasi majority carrier population is no longer dominant over the quasi minority carrier population. Although there are still many questions about the transport of charge carriers and recombination mechanisms within BHJ solar cells, the results presented in this dissertation and the associated manuscripts clearly show the usefulness of lateral device structures for studying the material and device physics associated with OPV cells.

Chapter 5: Majority Carrier Transport in Nanocrystals of Copper Indium Diselenide

5.1 INTRODUCTION

Colloidal nanocrystals are being studied for use in a variety of applications, including photovoltaic (PV) cells [78, 79], light-emitting diodes [80, 81], batteries [82, 83], field-effect transistors [84], memory devices [85], and other electronic devices [86]. In some cases, the goal is to make use of unique quantum effects of the materials, such as multi-exciton generation [87] and hot carrier collection [88]. Another motivation for their use is to provide low-cost solvent-based deposition methods for polycrystalline inorganic coatings that do not need high temperature or vacuum processes, similar to organic/polymeric semiconductors [89, 90].

Many proposed applications of nanocrystal films require charge transport through the layers. This is particularly true in the case of PV cells, where photogenerated electrons and holes must migrate out of the nanocrystal layer to electrode interfaces for extraction and power generation. The nanocrystals are typically surrounded by organic capping ligands, making the films inhomogeneous in composition with a high concentration of interfaces. Nanocrystals in the films can also exhibit strong Coulomb blockade at room temperature which results carrier transport that is typically slow with low carrier mobilities [91]. Recent work has focused on characterizing electronic conduction through semiconductor nanocrystal arrays, with the majority of the work focused on cadmium and lead-based materials [79, 88, 91-99]. Often, chemical or thermal treatments of the nanocrystal films have been employed to remove the capping ligands and reduce the interparticle spacing, thus helping to improve transport between nanocrystalline grains [95] and modifying the effective dopant concentration and polarity, with some nanocrystal materials exhibiting either n-type or p-type doping based

on the surface treatment conditions [84]. These treatments, however, have also been found to increase the concentration of surface states in some cases, resulting in conduction dominated by surface state hopping [92, 97].

Here we report the electrical transport characteristics of films of oleylamine-coated copper indium diselenide (CIS) nanocrystals. Temperature-dependent conductivity and capacitance-voltage measurements were carried out to determine the carrier concentration, mobility, and transport mechanism. CIS is a subset of copper indium gallium diselenide ($\text{Cu}(\text{In}_{1-x}\text{Ga}_x)\text{Se}_2$ or CIGS) semiconductors, which have been identified as one of the leading candidates to compete with crystalline silicon (Si) for solar cell fabrication [100, 101]. Single junction PV cells with vapor-deposited polycrystalline CIGS films have demonstrated solar power conversion efficiencies near 20% [102]. The synthesis of CIS nanocrystals and their use in PVs has been reported, with power conversion efficiency of up to 3.1% under AM1.5 illumination with only ambient processing and no post-treatment of the CIS absorber layer [103]. Hillhouse, Agrawal and coworkers have demonstrated much higher efficiencies (>10% PCE) by high temperature sintering (> 450°C) of $\text{CuIn}(\text{S},\text{Se})_2$ nanocrystal films under selenium vapor [104]. Sintering improves electron and hole transport in the films, but the need for high temperature processing increases the manufacturing cost significantly. In order to improve device efficiencies in nanocrystal-based PV cells that are not processed under extreme conditions, charge transport through the nanocrystal films must be understood.

In the case of vapor-deposited, sintered polycrystalline CIS films, charge transport through is well understood. Charge carrier mobilities above 30 $\text{cm}^2/\text{V}\cdot\text{s}$ have been reported, enabled by good crystalline order and large grain size [105]. CIS nanocrystal films on the other hand are a collection of 10–15 nm diameter nanocrystal grains embedded in insulating organic oleylamine capping ligands that separate the nanocrystals

by about 1-2 nm [3]. The oleylamine is important for formulating the nanocrystal ink as it facilitates dispersibility in solvents for solution-processibility and also appears to passivate electronic traps on the nanocrystal surfaces [98]. Nonetheless, the insulating organic material in the nanocrystal films inhibits charge transport. In this publication, majority charge transport (holes) in CIS nanocrystal films is characterized.

4.2 EXPERIMENTAL

CIS nanoparticle films were synthesized as reported by *Panthani et al.* [3] and spray deposited from 20 mg/mL dispersion in toluene to achieve a final thickness of 100 nm as measured by profilometry. Synthesis of nanocrystals was performed using standard air-free chemistry. Two types of CIS nanocrystals were studied. Elemental selenium (Se^0) particles were prepared by loading CuCl, InCl_3 , powdered Se, and degassed oleylamine in a three neck flask in a nitrogen filled drybox as a one-pot reaction. The reaction mixture was degassed under vacuum for 30 minutes, and then purged with dry nitrogen for 30 minutes. Reaction temperature was raised to 240°C and incubated for 60 minutes. Black slurry was the resulting product. Tributylphosphine selenium (TBP-Se) particles were prepared through a hot injection reaction. In this case, CuCl, InCl_3 , and degassed oleylamine were loaded in the three neck flask in a nitrogen filled glovebox, without any Se precursor. The product was similarly degassed and purged with dry nitrogen for 30 minutes in each step. The reactant temperature was raised to 180°C and a stoichiometric ratio of previously prepared tributylphosphine and selenium complex was injected into the vessel. The reaction temperature was raised to 240°C and incubated for 10 minutes. Similar looking black slurry was the reaction product. Undesirable by-products and remaining reactants were cleaned out of the

nanocrystal solution by a two-step solvent/anti-solvent cleaning. Cleaned product was dissolved in clean toluene at 20 mg/mL for spray deposition.

Cadmium sulfate (CdSO_4 , 99.999%) was purchased from *Aldrich Chemical Co.* Ammonium hydroxide (18M NH_3 , ACS certified) was purchased from Fisher Scientific. Thiourea (99.999%) was purchased from *Fluka*. A CdS buffer layer was deposited by chemical bath deposition following procedures described by *McCandless and Shafarman* [96]. The device is preheated to 90°C by placing it directly on a heated hotplate; 0.7 mL of an aqueous solution containing 3 mM CdSO_4 , 0.53 M thiourea, and 8.1 M NH_3 is dropcast on the surface of the device and the reaction chamber is quickly sealed by placing an inverted glass petri dish directly above the substrate. The reaction is allowed to proceed for 2 minutes. At that stage, the substrate is removed and washed by running DI water over the surface. The film is dried by blowing clean air over the surface.

Electrical tests were performed on CIS nanocrystal films incorporated into two different device structures. Capacitance-voltage measurements were performed using diode structures of CIS nanocrystal films deposited on indium tin oxide (ITO)-coated glass substrates. These substrates were initially cleaned with acetone, methanol, isopropyl alcohol, and deionized water followed by a 3 min UV/ozone exposure. CIS nanoparticle films were synthesized as described above and spray deposited using an Iwata airbrush (*Eclipse HP-CS*) to achieve a final thickness of 100 nm as measured by profilometry. The nanocrystal film was coated with a CdS buffer layer and completed with a 100 nm layer of aluminum to create a schottky diode. Devices for electrical conductivity measurements used glass substrates with the same spray deposited CIS layer as described above. Electrical contacts with a bottom layer of gold for good electrical contact and a top layer of silver for mechanical robustness were thermally evaporated through a shadow mask on top of the CIS layer to a final thickness of 100 nm. For the

measurements reported in this letter, the contacts had a separation of 50 μm and width of 1 mm.

Electrical testing was performed in a *Lakeshore Cryogenics* cryogenic probe station at a pressure of $< 10^{-3}$ Torr. C-V measurements were performed using a *HP 4284 LCR Meter* and I-V measurements were performed using an *Agilent 4155C Semiconductor Parameter Analyzer*. The I-V characteristics were linear over the entire temperature range indicating that contact resistance effects are minimal in these measurements. Measurements were also performed using devices with varying a channel length, ranging from 3 μm to 20 μm (in the dark at room temperature). The two point conductivity saturates when the channel length exceeds 10 μm , and shows little electric field dependence. The conductivity does fall at shorter channel lengths indicating that the contact resistance is more significant at these dimensions.

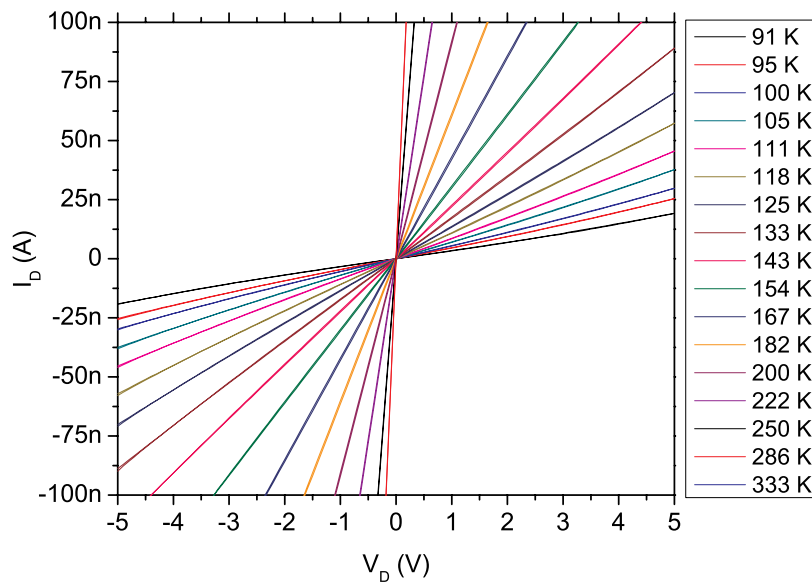


Figure 5.1: Current vs. voltage characteristics of TBP-Se CIS samples for temperature ranging from 91 K to 333 K.

5.3 RESULTS AND DISCUSSION

Carrier concentrations in the nanocrystal films were estimated from C-V measurements using the Mott-Schottky relation,

$$\frac{1}{C^2} = \frac{2}{q\epsilon N_A} \left(V_{fb} - V - \frac{kT}{q} \right) \quad (5.1)$$

where N_A is the dopant concentration, V_{fb} is the flat band potential, and V is the applied potential, q is the elementary charge, and ϵ is the dielectric constant. Figure 5.2 shows room temperature C-V data for two different films consisting of CIS nanocrystals prepared using slightly different reaction chemistries (TBP-Se CIS and Se^0 CIS) as described in the experimental section. The nanocrystal films are p-type with carrier concentrations in the low to mid 10^{17} cm^{-3} , which is consistent with previous measurements for nanocrystal CIS [103]. These values are about an order of magnitude higher than those of vapor deposited CIS [106]. C-V measurements were also performed at various temperatures ranging from 91 K to 333 K. As shown in Figure 5.3, the carrier concentration increased slightly with decreasing temperature, by about a factor of 2. The apparent change in carrier concentration could be a result of changing trap occupancy at interfaces between nanocrystals or at the CdS/nanocrystal layer interface [107].

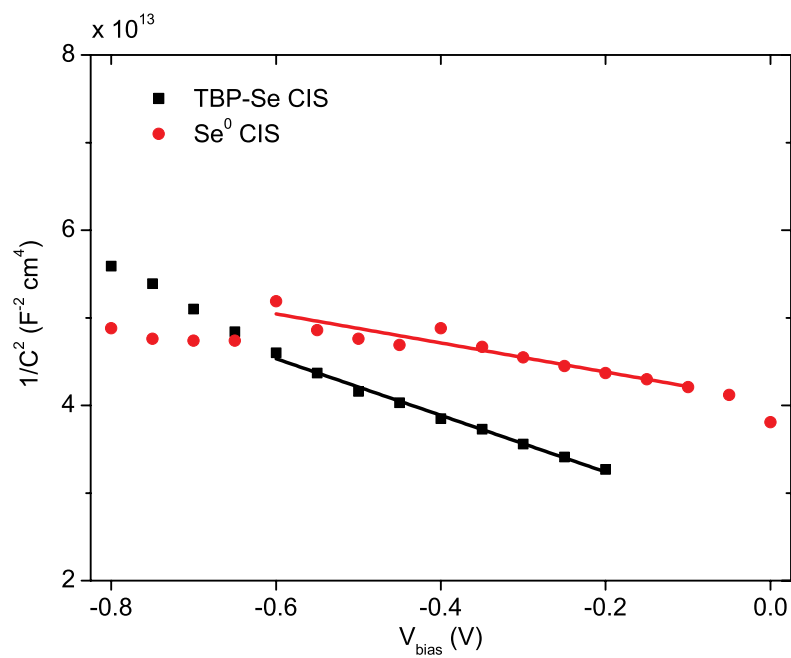


Figure 5.2: Mott-Schottky plot for CIS nanocrystal schottky diodes measured at room temperature made from TBP-Se CIS and Se^0 CIS measured shortly after preparation.

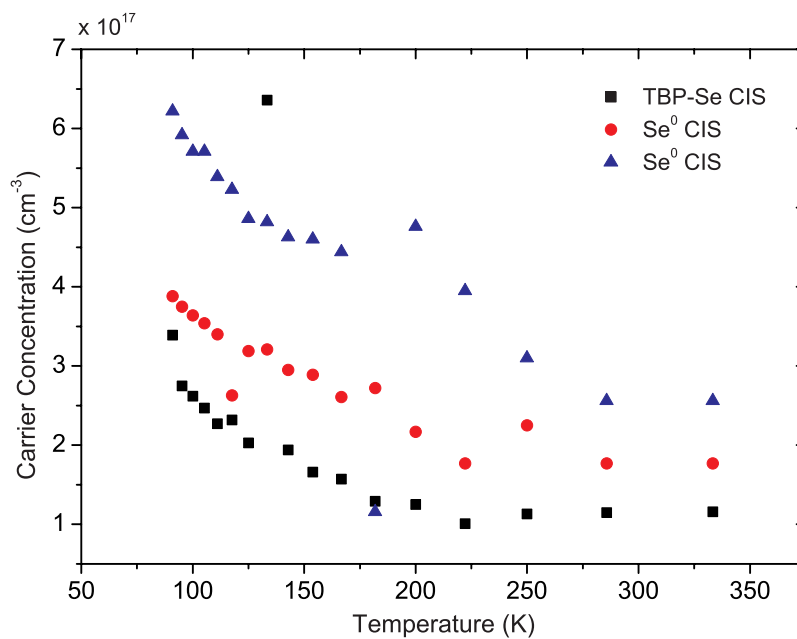


Figure 5.3: Majority carrier concentration as a function of temperature from 91 K - 333 K for CIS nanocrystal schottky diodes made from TBP-Se CIS and Se⁰ CIS measured shortly after preparation.

Temperature-dependent current-voltage (I-V) measurements were performed at temperatures ranging from 91-333 K. The electrical conductivity σ , was determined from the measured electrical resistance, the nanocrystal layer thickness, and the electrode geometry and was found to increase with increasing temperature. However, the increase in σ with increasing temperature is not due to an increase in carrier concentration, but rather an increase in carrier mobility. Figure 5.4 shows a plot of $LN(\sigma)$ vs. $T^{-\frac{1}{2}}$ for the six devices that were tested. The data labeled as TBP-Se and Se⁰ were CIS nanocrystals synthesized using slightly different approaches measured shortly after preparation and the data labeled TBP-Se Aged were measured 12 days after preparing the film. According to the Efros and Shklovskii model for variable range hopping (ES-VRH) [108]:

$$\sigma = \sigma'_0 e^{-\left(\frac{T'_0}{T}\right)^{\frac{1}{2}}} \quad (5.2)$$

where

$$T'_0 = \frac{2.8e^2}{4\pi\epsilon_r\epsilon_0ak_b} \quad (5.3)$$

and a is the localization length. The scaling of the conductivity with temperature is consistent with ES-VRH in the low temperature range, up to 181 K. Numerical fits of the conductivity data also fit Mott's VRH [109] but the ES-VRH model is more appropriate since the average hopping energy at a given temperature is less than Coulomb gap [110, 111]. *Shafarman et al.* describe a method for comparing the values T'_0 of for ES-VRH (equation 5.2) and T'_0 for Mott's VRH ($\sigma = \sigma_0 e^{-\left(\frac{T_0}{T}\right)^{\frac{1}{4}}}$), to determine whether or not the mean hopping energy is greater than the coulomb gap [111]. When $T > T_0/1170$, the coulomb gap can be neglected as the mean hopping energy is greater than the coulomb

gap and Mott's VRH is appropriate. For $T < T_0/2000$ the mean hopping energy is less than the coulomb gap and ES-VRH should be used. For the CIS samples measured, fits to Mott's VRH yield $T_0 \approx 2-7 \times 10^7$ K. As $T_0/2000 \approx 10^4$ K and all measurements are performed at temperatures much less than 10^4 K, the coulomb gap cannot be neglected and ES-VRH should accurately describe transport in the system. In addition, the coulomb gap width has been estimated to be greater than 60 meV using the relation $T'_0/T_{Cg} \approx 10$, where kT_{Cg} is the coulomb gap energy [111]. The values for T'_0 are extracted below from the temperature dependent conductivity data.

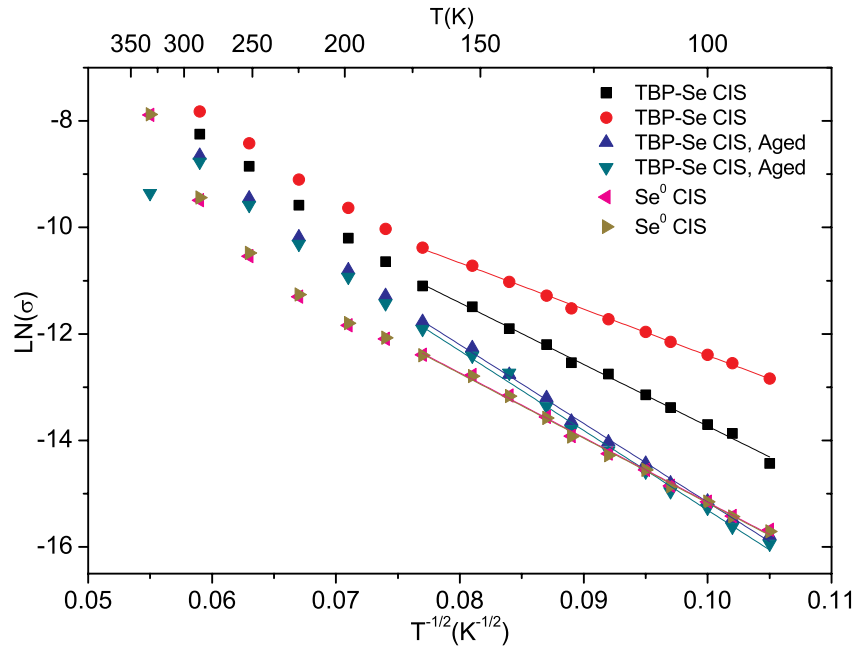


Figure 5.4: Plot of $LN(\sigma)$ vs. $T^{-1/2}$ for TBP-Se CIS nanoparticle samples measured shortly after preparation, TBP-Se CIS nanoparticle samples measured 12 days after preparation, and Se^0 CIS nanoparticle samples measured shortly after preparation.

Assuming ES-VRH, $T'_0 = 7.44 \times 10^3$ K, 2.18×10^4 K, and 1.46×10^4 K from the dark conductivity data for the TBP-Se CIS samples measured shortly after preparation,

TBP-Se CIS samples measured 12 days after preparation, and Se⁰ CIS samples measured shortly after preparation respectively. These results are in agreement with equation 3 where we estimate $T_0' \approx 1.2 \times 10^4$ K using $\epsilon_r \approx 4$, and $a \approx 1$ nm. Our results are also consistent with similar findings by Yu *et al.* for CdSe nanocrystal films [99]. The increase in T_0' for the 12 day old TBP-Se CIS samples and the Se⁰ CIS samples compared to freshly prepared TBP-Se CIS nanocrystal films could be a result of two different effects: the density of states may have decreased and/or the localization length has been altered [99, 109, 110]. It is possible that the increase in T_0' is related to a change in the density of thermally accessible states for the charge carriers as a result of a different precursor chemistry for the Se⁰ CIS samples and degradation over time for the TBP-Se CIS samples that were measured 12 days after preparation.

For temperatures above 181 K, the transport mechanism appears to change to nearest neighbor hopping (NNH), as has been reported for CdSe nanocrystals [94]. As the temperature increases, additional transport pathways become accessible and hopping to spatially closer sites becomes energetically possible at higher temperatures [112]. This transition occurs at T_A , where $T_A = \left(\frac{a}{4d}\right)^2 T_0'$ and d is the hopping distance between the surface states. Based on the data in Figure 5.4, the transition to NNH appears to occur around 181 K. Using this relation as well as values of T_0' and a specified above, we find the nearest neighbor hopping distance to be ~ 2 nm.

Values for the activation energy have been calculated for temperatures above 181 K using the well-known equation for thermally activated transport, $\sigma = \sigma_A e^{-\frac{E_A}{kT}}$. Figure 5.5 shows the logarithm of the conductivity vs. $1000/T$ with fits for the activation energy. The activation energy was determined to be 105 meV, 124 meV, and 135 meV from the dark conductivity data for the TBP-Se CIS samples measured shortly after preparation,

TBP-Se CIS samples measured 12 days after preparation, and Se^0 CIS samples measured shortly after preparation respectively. The increase in activation energy is consistent with increases found for T_0' at temperatures less than 181 K and indicates, for the 12 day old TBP-Se CIS samples and for the Se^0 CIS samples, there is an increased energy barrier between adjacent nanocrystals as compared to the freshly prepared TBP-Se CIS samples. The transition from VRH to nearest neighbor hopping has also been reported for nanocrystal films of PbSe, CdSe, CdTe, ZnO, and Au [91, 99, 113-115].

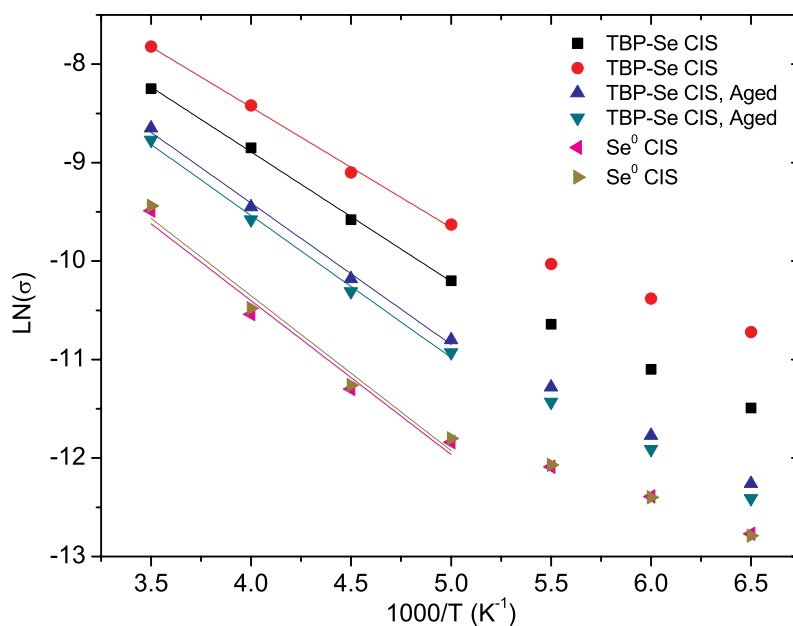


Figure 5.5: Plot of $\text{LN}(\sigma)$ vs. $1000/T$ for the aforementioned CIS nanoparticle samples for $T > 150$ K.

Figure 5.6 shows the temperature-dependent conductivity of Se^0 CIS films under an AM1.5 spectrum with an illumination intensity of 81 mW/cm^2 . The conductivity increases along the entire temperature range with illumination. This is partially a result of the carrier concentration increasing by about 75% ($7 \times 10^{17} \text{ cm}^{-3}$) due to the addition of

photogenerated carriers as well as changes in trap occupancy. The additional carriers fill trap states which reduces their effect on the remaining charge carriers present in the system. The constant T_0' for the Se^0 CIS samples under illumination is 6×10^3 K. The decrease in T_0' is a result of the additional photogenerated charge shifting the Fermi level toward the band edge, which allows charge carriers to more easily hop from one nanoparticle to another. This can also be seen in Figure 5.7, where at temperatures > 181 K, a transition to NNH again occurs. The activation energy under illumination is 71 meV which is about a 50% decrease from the Se^0 CIS samples in the dark indicating that the energy barrier between adjacent nanocrystals has been reduced by about 50%.

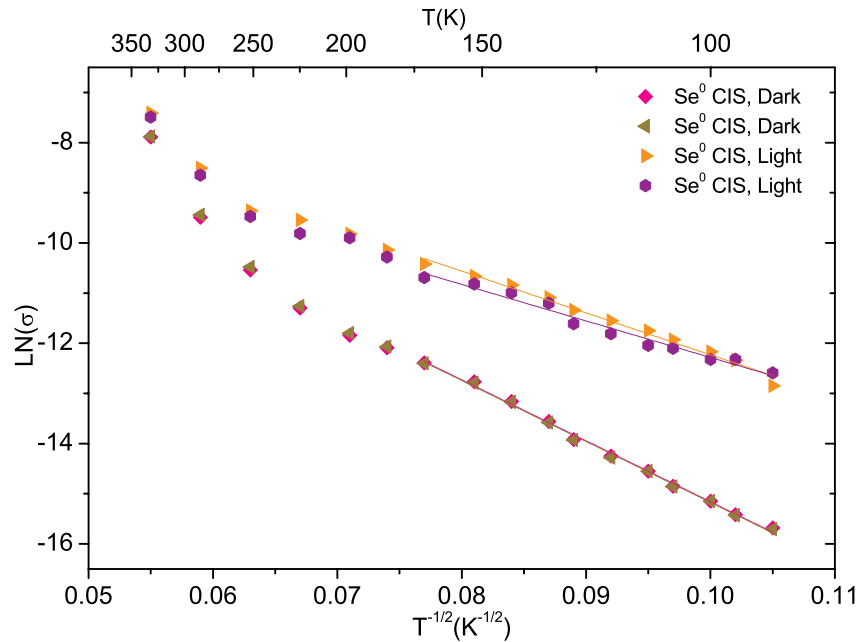


Figure 5.6: Plot of $\text{LN}(\sigma)$ vs. $T^{-1/2}$ for Se^0 CIS nanoparticle samples measured shortly after preparation in the dark and under an AM1.5g spectrum with an illumination intensity of 81 mW/cm^2 .

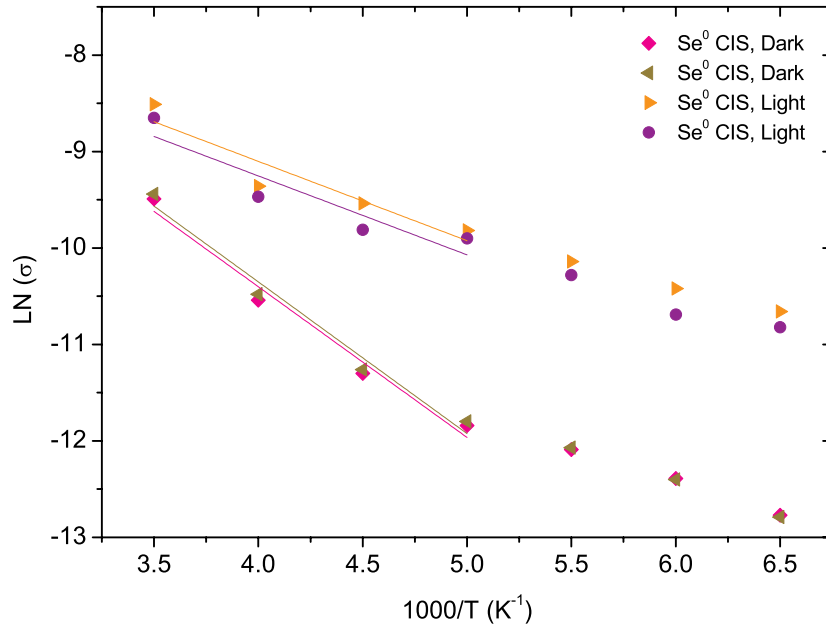


Figure 5.7: Plot of $LN(\sigma)$ vs. $1000/T$ for the aforementioned samples in the dark and under anAM1.5g illumination spectrum with an intensity of 81 mW/cm^2 for $T > 150 \text{ K}$.

The nanocrystals in the measured films range from 10 to 15 nm in diameter and their doping level at room temperature is $1\text{-}3 \times 10^{17} \text{ cm}^{-3}$. This corresponds to an average of about 1 charge carrier per nanocrystal. It is expected that charge movement in the film is limited by the numerous domain boundaries that the charges encounter and not transport through the delocalized energy levels within the nanocrystal. Since the probability of a hopping event is related to the distance between adjacent nanocrystals, it is expected that the carrier mobility (and as a result the carrier conductivity) should improve by reducing the spacing between nanocrystals [84, 95, 98]. This should greatly enhance the charge carrier mobilities and result in improved collection of photogenerated charges provided that electronic defects and traps on the nanocrystal surface remain passivated.

5.4 SUMMARY

In summary, we have reported on the majority carrier transport in spray-deposited films of CIS nanocrystals. The presence of organic ligands between the nanocrystals affects transport significantly. Our measurements indicate that charge moves by variable range hopping. We interpret this to be a result of hopping between filled states in one crystallite to an unfilled state in an adjacent nanocrystal. Reduction or elimination of these hopping distances should improve carrier mobility and improve the performance of solar cells made from these materials.

References

1. Rohatgi, A., D.S. Kim, K. Nakayashiki, V. Yelundur, and B. Rounsaville, *High-efficiency solar cells on edge-defined film-fed grown (18.2%) and string ribbon (17.8%) silicon by rapid thermal processing*. Applied Physics Letters, 2004. **84**(1): p. 145-147.
2. Hoppe, H. and N.S. Sariciftci, *Organic solar cells: An overview*. Journal of Materials Research, 2004. **19**(7): p. 1924-1945.
3. Panthani, M.G., V. Akhavan, B. Goodfellow, J.P. Schmidtke, L. Dunn, A. Dodabalapur, P.F. Barbara, and B.A. Korgel, *Synthesis of CuInS₂, CuInSe₂, and Cu(In_xGa_{1-x})Se₂ (CIGS) Nanocrystal "Inks" for Printable Photovoltaics*. Journal of the American Chemical Society, 2008. **130**(49): p. 16770-16777.
4. Steinhagen, C., M.G. Panthani, V. Akhavan, B. Goodfellow, B. Koo, and B.A. Korgel, *Synthesis of Cu₂ZnSnS₄ Nanocrystals for Use in Low-Cost Photovoltaics*. Journal of the American Chemical Society, 2009. **131**(35): p. 12554-12555.
5. Barth, S. and H. Bassler, *Intrinsic Photoconduction in PPV-Type Conjugated Polymers*. Physical Review Letters, 1997. **79**(22): p. 4445.
6. Gomes da Costa, P. and E.M. Conwell, *Excitons and the band gap in poly(phenylene vinylene)*. Physical Review B, 1993. **48**(3): p. 1993.
7. Marks, R.N. and et al., *The photovoltaic response in poly(p-phenylene vinylene) thin-film devices*. Journal of Physics: Condensed Matter, 1994. **6**(7): p. 1379.
8. Blom, P.W.M., V.D. Mihailetschi, L.J.A. Koster, and D.E. Markov, *Device Physics of Polymer:Fullerene Bulk Heterojunction Solar Cells*. Advanced Materials, 2007. **19**(12): p. 1551-1566.
9. Tang, C.W., *Two-layer organic photovoltaic cell*. Applied Physics Letters, 1986. **48**(2): p. 183-185.
10. Hoppe, H. and N.S. Sariciftci, *Organic solar cells: An overview*. Journal of Materials Research, 2004. **19**(07): p. 1924-1945.
11. Choong, V., Y. Park, Y. Gao, T. Wehrmeister, K. Mullen, B.R. Hsieh, and C.W. Tang, *Dramatic photoluminescence quenching of phenylene vinylene oligomer thin films upon submonolayer Ca deposition*. Applied Physics Letters, 1996. **69**(10): p. 1492-1494.
12. Halls, J.J.M., K. Pichler, R.H. Friend, S.C. Moratti, and A.B. Holmes, *Exciton diffusion and dissociation in a poly(p-phenylenevinylene)/C[_{sub 60}] heterojunction photovoltaic cell*. Applied Physics Letters, 1996. **68**(22): p. 3120-3122.

13. Halls, J.J.M. and R.H. Friend, *The photovoltaic effect in a poly(p-phenylenevinylene)/perylene heterojunction*. Synthetic Metals, 1997. **85**(1-3): p. 1307-1308.
14. Markov, D.E., E. Amsterdam, P.W.M. Blom, A.B. Sieval, and J.C. Hummelen, *Accurate Measurement of the Exciton Diffusion Length in a Conjugated Polymer Using a Heterostructure with a Side-Chain Cross-Linked Fullerene Layer*. The Journal of Physical Chemistry A, 2005. **109**(24): p. 5266-5274.
15. Markov, D.E., C. Tanase, P.W.M. Blom, and J. Wildeman, *Simultaneous enhancement of charge transport and exciton diffusion in poly(p -phenylene vinylene) derivatives*. Physical Review B, 2005. **72**(4): p. 045217.
16. Haeussler, D.M. *Fabrication of Organic Photovoltaic Devices*. 2009 [cited 2010 2/27/2011]; Available from: <http://viewnxt.blogspot.com/2009/10/fabrication-of-organic-photovoltaic.html>.
17. Yu, G., J. Gao, J.C. Hummelen, F. Wudl, and A.J. Heeger, *Polymer Photovoltaic Cells: Enhanced Efficiencies via a Network of Internal Donor-Acceptor Heterojunctions*. Science, 1995. **270**(5243): p. 1789-1791.
18. Yingling, Y.G. *Computational Soft and Bio Nanomaterials*. 2011 [cited 2011 March 6]; Available from: <http://www.mse.ncsu.edu/yingling/>.
19. Blom, P.W.M., M.J.M. de Jong, and M.G. van Munster, *Electric-field and temperature dependence of the hole mobility in poly(p-phenylene vinylene)*. Physical Review B, 1997. **55**(2): p. R656.
20. Tanase, C., E.J. Meijer, P.W.M. Blom, and D.M. de Leeuw, *Unification of the Hole Transport in Polymeric Field-Effect Transistors and Light-Emitting Diodes*. Physical Review Letters, 2003. **91**(21): p. 216601.
21. Dennler, G., A.J. Mozer, G. Juska, A. Pivrikas, R. Osterbacka, A. Fuchsbauer, and N.S. Sariciftci, *Charge carrier mobility and lifetime versus composition of conjugated polymer/fullerene bulk-heterojunction solar cells*. Organic Electronics, 2006. **7**(4): p. 229-234.
22. Mihailitchi, V.D., L.J.A. Koster, P.W.M. Blom, C. Melzer, B. de Boer, J.K.J. van Duren, and R.A.J. Janssen, *Compositional Dependence of the Performance of Poly(p-phenylene vinylene):Methanofullerene Bulk-Heterojunction Solar Cells*. Advanced Functional Materials, 2005. **15**(5): p. 795-801.
23. Juska, G., K. Arlauskas, R. Osterbacka, and H. Stubb, *Time-of-flight measurements in thin films of regioregular poly(3-hexyl thiophene)*. Synthetic Metals, 2000. **109**(1-3): p. 173-176.
24. Hau, S.K., H.-L. Yip, N.S. Baek, J. Zou, K. O'Malley, and A.K.Y. Jen, *Air-stable inverted flexible polymer solar cells using zinc oxide nanoparticles as an electron selective layer*. Applied Physics Letters, 2008. **92**(25): p. 253301-3.

25. Hau, S.K., H.-L. Yip, H. Ma, and A.K.Y. Jen, *High performance ambient processed inverted polymer solar cells through interfacial modification with a fullerene self-assembled monolayer*. Applied Physics Letters, 2008. **93**(23): p. 233304-3.
26. Mihailetschi, V.D., P.W.M. Blom, J.C. Hummelen, and M.T. Rispens, *Cathode dependence of the open-circuit voltage of polymer:fullerene bulk heterojunction solar cells*. Journal of Applied Physics, 2003. **94**(10): p. 6849-6854.
27. Langevin, P., *Recombinaison et mobilités des ions dans les gaz*. Annales Chimie et de Physique, 1903. **28**: p. 433.
28. Pivrikas, A., G. Juscaronka, Ouml, R. sterbacka, M. Westerling, M. Viliumacrnas, K. Arlauskas, and H. Stubb, *Langevin recombination and space-charge-perturbed current transients in regiorandom poly(3-hexylthiophene)*. Physical Review B, 2005. **71**(12): p. 125205.
29. Pivrikas, A., N.S. Sariciftci, G. Juscaronka, and R. Österbacka, *A review of charge transport and recombination in polymer/fullerene organic solar cells*. Progress in Photovoltaics: Research and Applications, 2007. **15**(8): p. 677-696.
30. Kim, Y., S. Cook, S.M. Tuladhar, S.A. Choulis, J. Nelson, J.R. Durrant, D.D.C. Bradley, M. Giles, I. McCulloch, C.-S. Ha, and M. Ree, *A strong regioregularity effect in self-organizing conjugated polymer films and high-efficiency polythiophene:fullerene solar cells*. Nat Mater, 2006. **5**(3): p. 197-203.
31. Koster, L.J.A., V.D. Mihailetschi, H. Xie, and P.W.M. Blom, *Origin of the light intensity dependence of the short-circuit current of polymer/fullerene solar cells*. Applied Physics Letters, 2005. **87**(20): p. 203502-3.
32. Osterbacka, R., G. Juska, K. Arlauskas, A.J. Pal, K.M. Kallman, and H. Stubb, *Electric field redistribution and electroluminescence response time in polymeric light-emitting diodes*. Journal of Applied Physics, 1998. **84**(6): p. 3359-3363.
33. Pivrikas, A., G. Juscaronka, A.J. Mozer, M. Scharber, K. Arlauskas, N.S. Sariciftci, H. Stubb, Ouml, and R. sterbacka, *Bimolecular Recombination Coefficient as a Sensitive Testing Parameter for Low-Mobility Solar-Cell Materials*. Physical Review Letters, 2005. **94**(17): p. 176806.
34. Juška, G., K. Arlauskas, M. Viliūnas, and J. Kočka, *Extraction Current Transients: New Method of Study of Charge Transport in Microcrystalline Silicon*. Physical Review Letters, 2000. **84**(21): p. 4946.
35. Juska, G., K. Genevicius, M. Viliunas, K. Arlauskas, H. Stuchllkov, A. Fejfar, and J. Kocka, *New method of drift mobility evaluation in [mu]c-Si:H, basic idea and comparison with time-of-flight*. Journal of Non-Crystalline Solids, 2000. **266-269**(Part 1): p. 331-335.

36. Juska, G., M. Viliunas, K. Arlauskas, N. Nekrasas, N. Wyrsh, and L. Feitknecht, *Hole drift mobility in μ c-Si:H*. Journal of Applied Physics, 2001. **89**(9): p. 4971-4974.
37. Juska, G., K. Arlauskas, M. Viliunas, K. Genevicius, R. Osterbacka, and H. Stubb, *Charge transport in π -conjugated polymers from extraction current transients*. Physical Review B, 2000. **62**(24): p. R16235.
38. Genevicius, K., R. Osterbacka, G. Juska, K. Arlauskas, and H. Stubb, *Charge transport in [π]-conjugated polymers from extraction current transients*. Thin Solid Films, 2002. **403-404**: p. 415-418.
39. Carius, R., F. Becker, R. Bruggemann, and H. Wagner, *Electroluminescence and forward bias currents in amorphous silicon p-i-n diodes: the effect of steady state bias and large i-layer thickness*. Journal of Non-Crystalline Solids, 1996. **198-200**(Part 1): p. 246-250.
40. Dean, R.H., *Transient Double Injection in Germanium*. Applied Physics Letters, 1968. **13**(5): p. 164-166.
41. Dean, R.H., *Transient Double Injection in Semiconductors with Traps*. Journal of Applied Physics, 1969. **40**(2): p. 596-602.
42. Dean, R.H., *Transient Double Injection in Trap-Free Semiconductors*. Journal of Applied Physics, 1969. **40**(2): p. 585-595.
43. Hack, M. and R.A. Street, *Analysis of double injection transients in amorphous silicon p-i-n diodes*. Journal of Applied Physics, 1992. **72**(6): p. 2331-2339.
44. Vanderhaghen, R. and D. Han, *Interface effects on double injection current and photocurrent in a-Si:H n-i-p and p-i-n diodes*. Journal of Non-Crystalline Solids, 1995. **190**(1-2): p. 95-106.
45. Juska, G., G. Sliuzys, K. Genevicius, A. Pivrikas, M. Scharber, G. Dennler, N.S. Sariciftci, and R. Osterbacka, *Charge-carrier transport and recombination in thin insulating films studied via extraction of injected plasma*. Physical Review B, 2006. **74**(11): p. 115314.
46. Cho, S., J. Yuen, J.Y. Kim, K. Lee, and A.J. Heeger, *Ambipolar organic field-effect transistors fabricated using a composite of semiconducting polymer and soluble fullerene*. Applied Physics Letters, 2006. **89**(15): p. 153505-3.
47. Anthopoulos, T.D., C. Tanase, S. Setayesh, E.J. Meijer, J.C. Hummelen, P.W.M. Blom, and D.M. de Leeuw, *Ambipolar Organic Field-Effect Transistors Based on a Solution-Processed Methanofullerene*. Advanced Materials, 2004. **16**(23-24): p. 2174-2179.
48. Rost, C., D.J. Gundlach, S. Karg, and W. Riess, *Ambipolar organic field-effect transistor based on an organic heterostructure*. Journal of Applied Physics, 2004. **95**(10): p. 5782-5787.

49. Marjanovic, N., T.B. Singh, G. Dennler, S. Günes, H. Neugebauer, N.S. Sariciftci, R. Schwödauer, and S. Bauer, *Photoresponse of organic field-effect transistors based on conjugated polymer/fullerene blends*. Organic Electronics, 2006. **7**(4): p. 188-194.
50. Padinger, F., R.S. Rittberger, and N.S. Sariciftci, *Effects of Postproduction Treatment on Plastic Solar Cells*. Advanced Functional Materials, 2003. **13**(1): p. 85-88.
51. Zaumseil, J. and H. Sirringhaus, *Electron and Ambipolar Transport in Organic Field-Effect Transistors*. Chemical Reviews, 2007. **107**(4): p. 1296-1323.
52. Dodabalapur, A., H.E. Katz, L. Torsi, and R.C. Haddon, *Organic Heterostructure Field-Effect Transistors*. Science, 1995. **269**(5230): p. 1560-1562.
53. Dodabalapur, A., H.E. Katz, L. Torsi, and R.C. Haddon, *Organic field-effect bipolar transistors*. Applied Physics Letters, 1996. **68**(8): p. 1108-1110.
54. Rost, C., S. Karg, W. Riess, M. Loi, M. Murgia, and M. Muccini, *Ambipolar light-emitting organic field-effect transistor*. Applied Physics Letters, 2004. **85**(9): p. 1613-1615.
55. Dinelli, F., R. Capelli, M.A. Loi, M. Murgia, M. Muccini, A. Facchetti, and T.J. Marks, *High-Mobility Ambipolar Transport in Organic Light-Emitting Transistors*. Advanced Materials, 2006. **18**(11): p. 1416-1420.
56. Lombardo, C. and A. Dodabalapur, *Nongeminate carrier recombination rates in organic solar cells*. Applied Physics Letters, 2010. **97**(23): p. 233302-3.
57. Österbacka, R., A. Pivrikas, G. Juska, K. Genevicius, K. Arlauskas, and H. Stubb, *Mobility and density relaxation of photogenerated charge carriers in organic materials*. Current Applied Physics, 2004. **4**(5): p. 534-538.
58. Street, R.A., S. Cowan, and A.J. Heeger, *Experimental test for geminate recombination applied to organic solar cells*. Physical Review B, 2010. **82**(12): p. 121301.
59. Hecht, K., *Zum Mechanismus des lichtelektrischen Primärstromes in isolierenden Kristallen*. Zeitschrift für Physik A Hadrons and Nuclei, 1932. **77**(3): p. 235-245.
60. Kočka, J., C.E. Nebel, and C.D. Abel, *Solution of the $\mu\tau$ problem in a-Si: H*. Philosophical Magazine Part B, 1991. **63**(1): p. 221 - 246.
61. Ruzin, A. and Y. Nemirovsky, *Methodology for evaluation of mobility-lifetime product by spectroscopy measurements in CdZnTe spectrometers*. Journal of Applied Physics, 1997. **82**(9): p. 4166-4171.
62. Toney, J.E., B.A. Brunett, T.E. Schlesinger, and R.B. James, *Photocurrent mapping as a probe of transport properties and electric field distributions in*

- cadmium zinc telluride detectors*. Nuclear Science, IEEE Transactions on, 1997. **44**(4): p. 1684-1691.
63. Lingren, C.L. and J.F. Butler, *Evaluating the performance of semiconductor radiation detectors through static charge analysis*. Nuclear Science, IEEE Transactions on, 1998. **45**(3): p. 1723-1725.
 64. Cox, G.A. and P.C. Knight, *Drift mobility, trapping and photogeneration of charge carriers in β -metal-free phthalocyanine single crystals*. Journal of Physics C: Solid State Physics, 1974. **7**(1): p. 146.
 65. Zhang, H. and J.-i. Hanna, *High $\mu\tau$ product in a smectic liquid crystalline photoconductor of a 2-phenylnaphthalene derivative*. Applied Physics Letters, 2004. **85**(22): p. 5251-5253.
 66. Cho, S., J. Yuen, J.Y. Kim, K. Lee, and A.J. Heeger, *Photovoltaic effects on the organic ambipolar field-effect transistors*. Applied Physics Letters, 2007. **90**(6): p. 063511-3.
 67. Monestier, F., J.-J. Simon, P. Torchio, L. Escoubas, F. Flory, S. Bailly, R. de Bettignies, S. Guillerez, and C. Defranoux, *Modeling the short-circuit current density of polymer solar cells based on P3HT:PCBM blend*. Solar Energy Materials and Solar Cells, 2007. **91**(5): p. 405-410.
 68. Waldauf, C., P. Schilinsky, J. Hauch, and C.J. Brabec, *Material and device concepts for organic photovoltaics: towards competitive efficiencies*. Thin Solid Films, 2004. **451-452**: p. 503-507.
 69. Shao, Y. and Y. Yang, *Efficient Organic Heterojunction Photovoltaic Cells Based on Triplet Materials*. Advanced Materials, 2005. **17**(23): p. 2841-2844.
 70. Lenes, M., M. Morana, C.J. Brabec, and P.W.M. Blom, *Recombination-Limited Photocurrents in Low Bandgap Polymer/Fullerene Solar Cells*. Advanced Functional Materials, 2009. **19**(7): p. 1106-1111.
 71. Mihailetchi, V.D., H.X. Xie, B. de Boer, L.J.A. Koster, and P.W.M. Blom, *Charge Transport and Photocurrent Generation in Poly(3-hexylthiophene): Methanofullerene Bulk-Heterojunction Solar Cells*. Advanced Functional Materials, 2006. **16**(5): p. 699-708.
 72. Ooi, Z.E., T.L. Tam, A. Sellinger, and J.C. deMello, *Field-dependent carrier generation in bulk heterojunction solar cells*. Energy & Environmental Science, 2008. **1**(2): p. 300-309.
 73. Däubler, T.K., V. Cimrová, S. Pfeiffer, H.H. Hörhold, and D. Neher, *Electric Field and Wavelength Dependence of Charge Carrier Photogeneration in Soluble Poly(p-phenylenevinylene) Derivatives*. Advanced Materials, 1999. **11**(15): p. 1274-1277.

74. Jin, H., Y.-B. Hou, X.-G. Meng, and F. Teng, *Electric field-induced quenching of photoluminescence in the MEH-PPV:C60 composite thin film*. Chemical Physics Letters, 2007. **443**(4-6): p. 374-377.
75. Ramo, S., *Currents Induced by Electron Motion*. Proceedings of the IRE, 1939. **27**(9): p. 584-585.
76. Mozer, A.J., G. Dennler, N.S. Sariciftci, M. Westerling, A. Pivrikas, R. Österbacka, and G. Juska, *Time-dependent mobility and recombination of the photoinduced charge carriers in conjugated polymer/fullerene bulk heterojunction solar cells*. Physical Review B, 2005. **72**(Copyright (C) 2010 The American Physical Society): p. 035217.
77. Cowan, S.R., A. Roy, and A.J. Heeger, *Recombination in polymer-fullerene bulk heterojunction solar cells*. Physical Review B, 2010. **82**(24): p. 245207.
78. Gur, I., N.A. Fromer, C.-P. Chen, A.G. Kanaras, and A.P. Alivisatos, *Hybrid Solar Cells with Prescribed Nanoscale Morphologies Based on Hyperbranched Semiconductor Nanocrystals*. Nano Letters, 2006. **7**(2): p. 409-414.
79. Hillhouse, H.W. and M.C. Beard, *Solar cells from colloidal nanocrystals: Fundamentals, materials, devices, and economics*. Current Opinion in Colloid & Interface Science, 2009. **14**(4): p. 245-259.
80. Colvin, V.L., M.C. Schlamp, and A.P. Alivisatos, *Light emitting diodes made from cadmium selenide nanocrystals and a semiconducting polymer*. Nature, 1994. **370**(6488): p. 354-357.
81. Anikeeva, P.O., J.E. Halpert, M.G. Bawendi, and V. Bulović, *Quantum Dot Light-Emitting Devices with Electroluminescence Tunable over the Entire Visible Spectrum*. Nano Letters, 2009. **9**(7): p. 2532-2536.
82. Holzapfel, M., H. Buqa, W. Scheifele, P. Novak, and F.-M. Petrat, *A new type of nano-sized silicon/carbon composite electrode for reversible lithium insertion*. Chemical Communications, 2005(12): p. 1566-1568.
83. Harris, J.T., J.L. Hueso, and B.A. Korgel, *Hydrogenated Amorphous Silicon (a-Si:H) Colloids*. Chemistry of Materials, 2010. **22**(23): p. 6378-6383.
84. Talapin, D.V. and C.B. Murray, *PbSe Nanocrystal Solids for n- and p-Channel Thin Film Field-Effect Transistors*. Science, 2005. **310**(5745): p. 86-89.
85. Patel, R.N., A.T. Heitsch, C. Hyun, D.-M. Smilgies, A. de Lozanne, Y.-L. Loo, and B.A. Korgel, *Printed Magnetic FePt Nanocrystal Films*. ACS Applied Materials & Interfaces, 2009. **1**(6): p. 1339-1346.
86. Dresselhaus, M.S., G. Chen, M.Y. Tang, R.G. Yang, H. Lee, D.Z. Wang, Z.F. Ren, J.P. Fleurial, and P. Gogna, *New Directions for Low-Dimensional Thermoelectric Materials*. Advanced Materials, 2007. **19**(8): p. 1043-1053.

87. Beard, M.C., A.G. Midgett, M. Law, O.E. Semonin, R.J. Ellingson, and A.J. Nozik, *Variations in the Quantum Efficiency of Multiple Exciton Generation for a Series of Chemically Treated PbSe Nanocrystal Films*. Nano Letters, 2009. **9**(2): p. 836-845.
88. Bao, H., B.F. Habenicht, O.V. Prezhdo, and X. Ruan, *Temperature dependence of hot-carrier relaxation in PbSe nanocrystals: An ab initio study*. Physical Review B, 2009. **79**(23): p. 235306.
89. Akhavan, V.A., B.W. Goodfellow, M.G. Panthani, and B.A. Korgel, *Towards the next generation of Ultra-low-cost photovoltaics using low cost inks*. Modern Energy Review, 2010. **2**(2): p. 25.
90. Beek, W.J.E., M.M. Wienk, M. Kemerink, X. Yang, and R.A.J. Janssen, *Hybrid Zinc Oxide Conjugated Polymer Bulk Heterojunction Solar Cells*. The Journal of Physical Chemistry B, 2005. **109**(19): p. 9505-9516.
91. Romero, H.E. and M. Drndic, *Coulomb Blockade and Hopping Conduction in PbSe Quantum Dots*. Physical Review Letters, 2005. **95**(15): p. 156801.
92. Geyer, S., V.J. Porter, J.E. Halpert, T.S. Mentzel, M.A. Kastner, and M.G. Bawendi, *Charge transport in mixed CdSe and CdTe colloidal nanocrystal films*. Physical Review B, 2010. **82**(15): p. 155201.
93. Guyot-Sionnest, P. and C. Wang, *Fast Voltammetric and Electrochromic Response of Semiconductor Nanocrystal Thin Films*. The Journal of Physical Chemistry B, 2003. **107**(30): p. 7355-7359.
94. Kang, M.S., A. Sahu, D.J. Norris, and C.D. Frisbie, *Size-Dependent Electrical Transport in CdSe Nanocrystal Thin Films*. Nano Letters, 2010. **10**(9): p. 3727-3732.
95. Law, M., J.M. Luther, Q. Song, B.K. Hughes, C.L. Perkins, and A.J. Nozik, *Structural, Optical, and Electrical Properties of PbSe Nanocrystal Solids Treated Thermally or with Simple Amines*. Journal of the American Chemical Society, 2008. **130**(18): p. 5974-5985.
96. McCandless, B.E. and W.N. Shafarman. *Chemical surface deposition of ultra-thin cadmium sulfide films for high performance and high cadmium utilization*. in *Photovoltaic Energy Conversion, 2003. Proceedings of 3rd World Conference on*. 2003.
97. Mentzel, T.S., V.J. Porter, S. Geyer, K. MacLean, M.G. Bawendi, and M.A. Kastner, *Charge transport in PbSe nanocrystal arrays*. Physical Review B, 2008. **77**(7): p. 075316.
98. Porter, V.J., S. Geyer, J.E. Halpert, M.A. Kastner, and M.G. Bawendi, *Photoconduction in Annealed and Chemically Treated CdSe/ZnS Inorganic*

- Nanocrystal Films*. The Journal of Physical Chemistry C, 2008. **112**(7): p. 2308-2316.
99. Yu, D., C. Wang, B.L. Wehrenberg, and P. Guyot-Sionnest, *Variable Range Hopping Conduction in Semiconductor Nanocrystal Solids*. Physical Review Letters, 2004. **92**(21): p. 216802.
 100. Powalla, M. and B. Dimmler, *Scaling up issues of CIGS solar cells*. Thin Solid Films, 2000. **361-362**: p. 540-546.
 101. Chopra, K.L., P.D. Paulson, and V. Dutta, *Thin-film solar cells: an overview*. Progress in Photovoltaics: Research and Applications, 2004. **12**(2-3): p. 69-92.
 102. Green, M.A., K. Emery, Y. Hishikawa, and W. Warta, *Solar cell efficiency tables (version 37)*. Progress in Photovoltaics: Research and Applications, 2011. **19**(1): p. 84-92.
 103. Akhavan, V.A., M.G. Panthani, B.W. Goodfellow, D.K. Reid, and B.A. Korgel, *Thickness-limited performance of CuInSe₂ nanocrystal photovoltaic devices*. Opt. Express, 2010. **18**(S3): p. A411-A420.
 104. Guo, Q., H.W. Hillhouse, and R. Agrawal, in *2009 AIChE Annual Meeting*. 2009: Nashville. p. 447C.
 105. Mesa, F., C. Calderon, and G. Gordillo, *Study of electrical properties of CIGS thin films prepared by multistage processes*. Thin Solid Films, 2010. **518**(7): p. 1764-1766.
 106. Repins, I., M. Contreras, M. Romero, Y. Yan, W. Metzger, J. Li, S. Johnston, B. Egaas, C. DeHart, J. Scharf, B.E. McCandless, and R. Noufi. *Characterization of 19.9%-efficient CIGS absorbers*. in *Photovoltaic Specialists Conference, 2008. PVSC '08. 33rd IEEE*. 2008.
 107. Guha, P., S.N. Kundu, S. Chaudhuri, and A.K. Pal, *Electron transport processes in CuIn_{1-x}Ga_xSe₂ films prepared by four source co-evaporation technique*. Materials Chemistry and Physics, 2002. **74**(2): p. 192-200.
 108. Efros, A.L. and B.I. Shklovskii, *Coulomb gap and low temperature conductivity of disordered systems*. Journal of Physics C: Solid State Physics, 1975. **8**(4): p. L49.
 109. Mott, N.F. and E.A. Davis, *Electronic Processes in Non-Crystalline Materials*. 1971, London: Oxford University Press.
 110. Mott, N., *Conduction in Non-Crystalline Materials*. Second ed. 1993, New York: Oxford University Press.
 111. Shafarman, W.N., D.W. Koon, and T.G. Castner, *dc conductivity of arsenic-doped silicon near the metal-insulator transition*. Physical Review B, 1989. **40**(2): p. 1216.

112. Adkins, C.J., *Conduction in granular metals-variable-range hopping in a Coulomb gap?* Journal of Physics: Condensed Matter, 1989. **1**(7): p. 1253.
113. Bera, S.K., S. Chaudhuri, and A.K. Pal, *Electron transport properties of CdTe nanocrystals in SiO₂/CdTe/SiO₂ thin film structures.* Thin Solid Films, 2002. **415**(1-2): p. 68-77.
114. Roest, A.L., J.J. Kelly, and D. Vanmaekelbergh, *Coulomb blockade of electron transport in a ZnO quantum-dot solid.* Applied Physics Letters, 2003. **83**(26): p. 5530-5532.
115. Tran, T.B., I.S. Beloborodov, X.M. Lin, T.P. Bigioni, V.M. Vinokur, and H.M. Jaeger, *Multiple Cotunneling in Large Quantum Dot Arrays.* Physical Review Letters, 2005. **95**(7): p. 076806.

Vita

Christopher Joseph Lombardo was born on June 29, 1982 in Annapolis, MD to Maureen and Joe Lombardo. He graduated from Broadneck High School in Annapolis, MD in 2000. He attended the University of Maryland at College Park and graduated from the A. James Clark School of Engineering with a Bachelor of Science in Electrical Engineering and the College of Computer, Mathematical, and Physical Sciences with a Bachelor of Science in Physics in 2005. While at the University of Maryland, Christopher was inducted into Eta Kappa Nu, the electrical and computer engineering honor society, in 2002 and in 2004 he began working with Engineers Without Borders-USA and is still highly involved with that organization. He attended graduate school at The University of Texas at Austin and received his Master of Science in Electrical and Computer Engineering in 2007. Christopher's doctoral research in organic bulk heterojunction solar cells and other topics has been supervised by Professor Ananth Dodabalpur for the duration of his studies at UT.

Permanent email address: clombardo@gmail.com

This dissertation was typed by the author.